Environment Canada
Conservation and Protection

Environnement Canada
Conservation et Protection

Yukon River Headwater Lakes Study, 1983 and 1985: Observations and Analysis

P.F. Hamblin

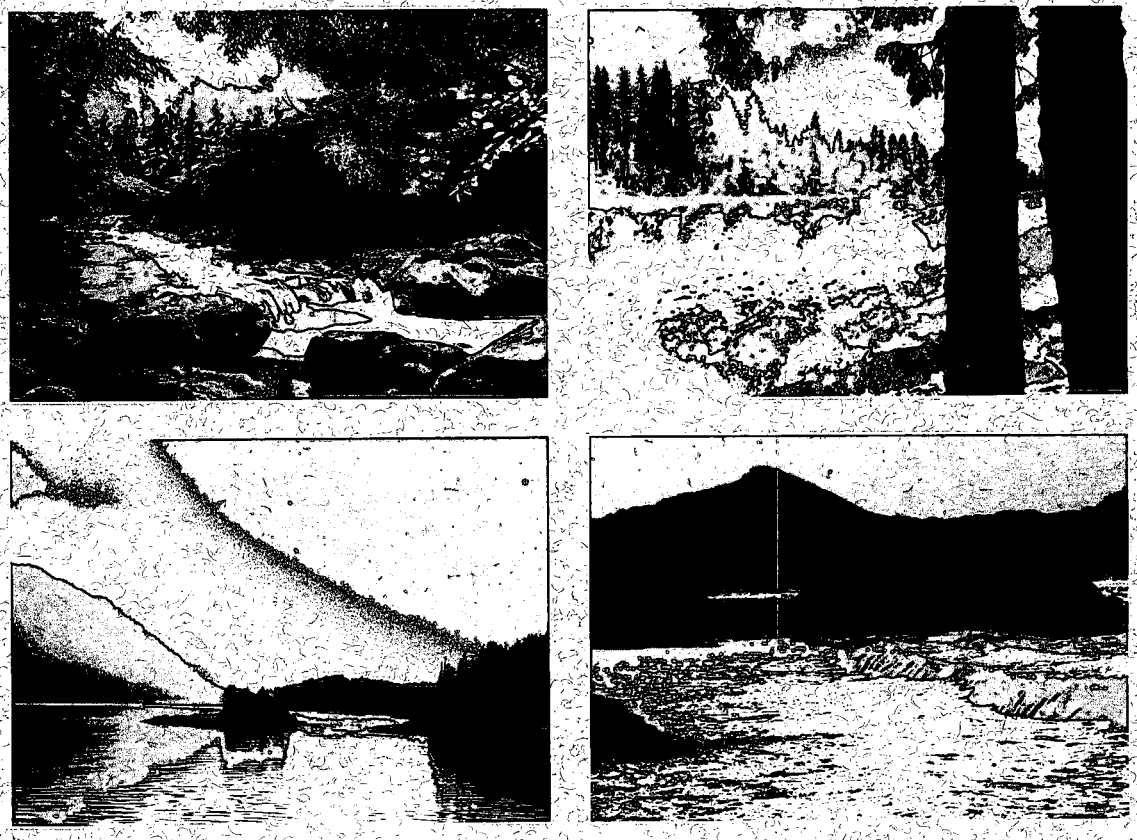

SCIENTIFIC SERIES NO. 175

GB
707
C335
no. 175E

LAKES RESEARCH BRANCH
NATIONAL WATER RESEARCH INSTITUTE
CANADA CENTRE FOR INLAND WATERS
BURLINGTON, ONTARIO, 1990

(Disponible en français sur demande)

Canada

Environment Canada | Environnement Canada
Conservation and Protection | Conservation et Protection

Yukon River Headwater Lakes Study, 1983 and 1985: Observations and Analysis

P.F. Hamblin

SCIENTIFIC SERIES NO. 175

LAKES RESEARCH BRANCH
NATIONAL WATER RESEARCH INSTITUTE
CANADA CENTRE FOR INLAND WATERS
BURLINGTON, ONTARIO, 1990

(Disponible en français sur demande)

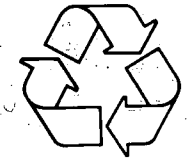

Printed on paper that contains recovered waste

Published by authority of
the Minister of the Environment

Cat. No. En 36-502/175E
ISBN 0-662-18449-1

Contents

Contents (Cont.)

Tables

Illustrations

Illustrations (Cont.)

Illustrations (Cont.)

Abstract

Field programs were initiated in the late winters of 1983 and 1985 to obtain an understanding of the physical processes responsible for winter ice cover in lakes and reservoirs. This report documents many of the observations made on three headwater lakes of the Yukon River basin (Marsh, Tagish, and Laberge), presents analyses of through-flow phenomena, establishes the validity of field observations and parameterizations required for thermodynamic models of lakes, and develops some specialized mathematical models of the inflow, through-flow, and outflow of deep riverine lakes.

Unlike the summer flow conditions in these and some other ice-covered lakes, the winter through-flow current was not concentrated as a boundary current. In the 1983 study, it was found that, apart from the immediate inflow area, the current flow was below the threshold of a specially designed acoustic time-of-flight current profiler. In the subsequent experiment in 1985, a novel under-ice drogue was deployed successfully, which made it possible to delineate the weak under-ice flow. When the flow measurements were combined with temperature profile observations, they offered a picture of the circulation in a large ice-covered riverine lake. The outflow and the associated heat flux tend to be concentrated more at the surface on the left-hand side of the lake looking in the direction of outflow. Possible outflow instabilities offer an interpretation of the observed irregularities in the drogue trajectories.

The sensible heat transfer between water and ice was inferred by a number of methods in Tagish and Marsh lakes to be represented by a bulk transfer coefficient of 0.8×10^{-3}. A thermal model of the Yukon River, including such effects as the shading of solar radiation by the river banks, simulated the observed temperatures to an RMS error of 1°C and, therefore, was used to supply missing water temperatures. Two expressions for incoming longwave radiation were tested. The Swinbank formula was found to be superior for daily air temperatures above 0°C and the Anderson relation better at lower temperatures. A standard method of

estimating the fraction of daily cloud cover was evaluated for a northern site.

Four mathematical models were formulated to examine various aspects of winter circulation in large lakes. A diagnostic three-dimensional model of flow-through under ice with Ekman friction was found to be qualitatively similar to the drogue observations, but problems remained in the specification of the open boundary conditions. A steady two-dimensional analytical model demonstrated the observed flow concentrations on the left-hand side of the outflow and suggested that the upward heat flux from the water to the ice and air decays with the square root of the distance from the outflow. A one-dimensional similarity model of the outflow dynamics offered a means of determining the distance from the outflow at which the upward transport of heat equals or exceeds the atmospheric heat loss and thus allows an estimate of the size and area of the outflow polynya. This model suggested decay of the heat flux varying inversely with distance from the outflow. An unsteady two-dimensional and nonhydrostatic numerical model gave only qualitative agreement with the above two outflow models. It would appear that these two methods are too simple to parameterize the outflowing heat flux accurately. Unfortunately, the numerical model, when extended from a simple rectangularly shaped lake to a more realistic variable-depth lake, was too computationally elaborate to reach a final steady state for both the flow and temperature fields.

Résumé

Dans le but de comprendre les phénomènes physiques responsables de la formation de la couverture de glace sur les lacs et les réservoirs durant l'hiver, il a été décidé à la fin des hivers 1983 et 1985, d'entreprendre des programmes de recherche sur le terrain. Ce rapport présente plusieurs observations relatives à trois lacs du cours supérieur du bassin du fleuve Yukon (les lacs Marsh, Tagish et Laberge), présente les analyses des phénomènes d'ecoulement de l'eau à travers le lac, établit la validité des observations sur le terrain et du paramétrage nécessaires à l'élaboration de modèles thermodynamiques des lacs, et présente un certain nombre de modèles mathématiques du débit entrant, de l'écoulement de l'eau à travers le lac et du débit sortant des lacs profonds qui ont des débits entrant et sortant suffisamment importants pour déterminer en partie la circulation de l'eau dans ces lacs.

Contrairement à ce qui est observé dans ces lacs et d'autres lacs couverts de glace ou durant l'été, le courant traversant les lacs étudiés n'était pas concentré le long des rives. Dans l'étude de 1983, l'intensité du courant était en dessous du seuil de détection d'un courantomètre acoustique à temps de passage spécialement conçu pour ces recherches, sauf dans la région où arrive le débit entrant. Dans l'expérience subséquente, en 1985, l'emploi avec succès d'une drogue originale, conçue pour aller sous la glace, a permis de caractériser le faible écoulement de l'eau sous la glace. Les mesures de courant ainsi obtenues, conjuguées aux données relatives au profil de température, ont permis d'établir la manière dont l'eau circule dans un grand lac couvert de glace dont les débits entrant et sortant sont suffisamment importants pour déterminer en partie l'écoulement de l'eau. Le débit sortant et le flux de chaleur concomitant ont tendance à se concentrer davantage à la surface du côté gauche du lac, c'est-à-dire à gauche quand on regarde dans la direction de l'écoulement du débit sortant. L'instabilité possible du débit sortant permettrait d'interpréter les trajectoires irrégulières de la drogue.

Un certain nombre de méthodes utilisées dans les lacs Tagish et Marsh ont permis de déduire que le transfert de chaleur sensible entre

l'eau et la glace pouvait être exprimé, dans l'ensemble, par un coefficient de transfert de 0,8 x 10^{-3}. Un modèle thermique du fleuve Yukon qui prenait en considération des facteurs tels que le blocage des radiations solaires par les rives, a permis de simuler les températures observées avec une erreur quadratique moyenne de 1 °C. Ce modèle a donc été utilisé pour obtenir les valeurs manquantes de température de l'eau. Deux formules mathématiques portant sur l'apport calorifique des radiations infrarouges ont été mises à l'épreuve. La formule de Swinbank s'est avérée supérieure quand la température de l'air durant le jour est supérieur à 0 °C tandis que la relation d'Anderson était supérieure à des températures plus basses. Une méthode normalisée permettant d'estimer la nébulosité quotidienne a été évaluée dans des conditions nordiques.

Un certain nombre de modèles mathématiques ont été mis au point dans le but d'étudier différents aspects de la circulation de l'eau dans les lacs de grandes dimensions pendant l'hiver. Un modèle diagnostique tridimensionnel de l'écoulement de l'eau sous la glace tenant compte de la friction d'Ekman a donné des résultats qualitativement similaires à ceux obtenus avec la drogue mais certains problèmes relatifs à la caractérisation des conditions aux limites dans le cas d'une masse d'eau qui n'est délimitée par aucune frontière physique n'ont pas été résolus. Un modèle analytique invariable bidimensionnel décrivant la concentration du courant du côté gauche du débit sortant donne à penser que le flux de chaleur allant de l'eau à la glace et à l'air décroît en proportion de la racine carré de l'éloignement par rapport au débit sortant. Un modèle de similitude unidimensionnel de la dynamique du débit sortant rend possible l'évaluation de la distance, par rapport au débit sortant, à laquelle le transfert de chaleur vers le haut est égal ou supérieur à la perte de chaleur atmosphérique et permet donc d'estimer la taille et la localisation de la polynie du débit sortant. Ce modèle donne à penser que le flux de chaleur varie en fonction inverse de l'éloignement par rapport au débit sortant. Un modèle numérique unidimensionel non hydrostatique et instable n'a concordé que qualitativement avec les deux modèles de débit sortant ci-dessus. Il semblerait que ces deux méthodes

sont trop simples pour paramétrer avec précision le flux de chaleur du débit sortant. Malheureusement, le modèle numérique, bien qu'il soit valable pour un lac rectangulaire simplifié, demandait des calculs trop complexes et ne pouvait atteindre un état d'équilibre final en ce qui a trait aux champs d'écoulement et de température dans le cas d'un lac profond réel et donc irrégulier.

Management Perspective

Field investigations of the physical limnology of the headwater lakes of the Yukon River basin were undertaken during the late winters of 1983 and 1985. The emphasis on the behaviour of the temperature and flow fields near the outflow, the through-flow process, and their relation to ice cover thickness and extent stemmed from the need for fundamental knowledge of the impact of possible future hydroelectric power developments in the Yukon River basin on the river, lake, and reservoir ice regimes. Specific topics studied in this report, which provide input to a model of the winter thermal regime of lakes and reservoirs, are the determination of the coefficient of sensible heat transfer between lake ice and water, the specification of river inflow temperatures from standard meteorological data, the computation of certain radiation terms, and the parameterization of the outflow of heat from an ice-covered lake or reservoir.

Acknowledgments

Scientific discussions with E. Carmack and R. Spigel have been most fruitful. C.H. Mortimer is thanked for his interest in this study and making available some reprints from the early literature from his collection. Y.M.R. Marmoush's assistance in the running of the cavity flow model is gratefully acknowledged.

Yukon River Headwater Lakes Study, 1983 and 1985: Observations and Analysis

P.F. Hamblin

INTRODUCTION

Study Description

In 1981, the Pacific and Yukon Branch of the National Water Research Institute initiated a study of the circulation and thermal regimes of the Yukon River headwater lakes and of the sensitivity of these lakes to possible future hydroelectric power development in the Yukon River basin. The first phase of this study was necessarily descriptive and involved the determination of the bathymetry of the major lakes and their annual thermal and salinity cycles (Kirkland and Gray, 1986). The second phase, which was more narrowly focused, attempted to address the practical problem of understanding the physical behaviour of a large northern impoundment should such structures be built in the Yukon River basin. For this reason, Lake Laberge (Fig. 1) was selected as a typical example of a large northern reservoir suitable for detailed study involving long-term meteorological, ice thickness, and water temperature observations for the verification of a northern impoundment water quality model. It was recognized at the onset of the Lake Laberge study that more detailed observations in the vicinity of the inflow and outflow regions were warranted. The regional thermal studies revealed an interesting feature common to these headwater lakes: during the winter, they exhibit ice-free zones known technically as polynyas. Polynyas are situated in all the outflowing regions and at some of the lake inflows as well.

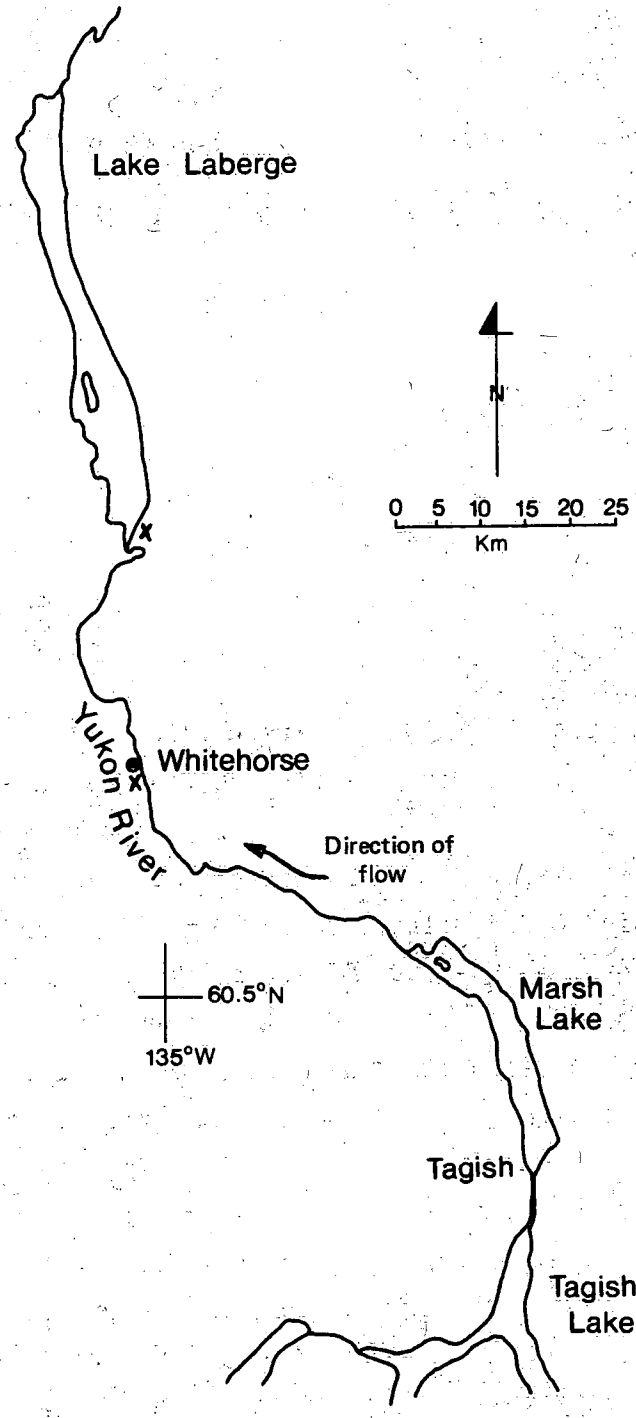

Figure 1. Location of Yukon River headwater lakes studied. X marks locations of meteorological observations.

In 1983, flow and thermal structure were measured in Lake Laberge by means of a current meter and a temperature/conductivity profiler in order to study the inflow region in greater detail during the

ice-covered period. The results of this study are presented in Part I of this report. A study of the outflow dynamics was commissioned in 1985. For logistical reasons, it was not carried out in the remote northern end of Lake Laberge, but in the more readily accessible outflow regions of Marsh and Tagish lakes (Fig. 1). In addition to the detailed circulation and thermal structure observations, which are outlined in Part II of this report, this study attempted to determine the sensible heat transfer coefficient between the water and ice cover, which was indicated as a key unknown parameter from the early modelling results of Lake Laberge.

Besides knowledge of the sensible heat transfer coefficient between water and ice, the Lake Laberge thermal simulation model required the daily average temperature of the major inflowing river, the Yukon River. Since these data were interrupted from time to time by equipment failure, it was necessary to develop a mathematical model of the thermal regime of a river. This is described in detail in Part III. It is the intention of the lake thermal simulation model to include the formation and maintenance of the observed polynya within the framework of the one-dimensional model. This requires sufficient understanding of the outflow dynamics in order to formulate a suitable parameterization of the outflowing heat flux. This problem is also discussed in Part III.

Related Studies

Scandinavian workers collected and reported observations of winter ice conditions and temperatures in lakes as early as 1941 with Liljequist's report on Lake Vetter in Sweden. Mellin (1947 and 1948) first drew attention to regulated waterflow and its effect on black ice thickness, particularly late in the season, and showed convincingly the upwelling of warmer water near the outflow of Swedish lakes. More recently, Stigebrandt (1978) has discussed the dynamics of flow under ice in lakes. The open literature on polynyas is scant, with the three-part series by Topham et al. (1983) being the most current contribution. Carmack et al. (1987) have presented additional observations to those discussed here for Lake Laberge.

PART I: WINTER THROUGH-FLOW STUDY OF LAKE LABERGE, MARCH 1983

Purpose

The purpose of the study at Lake Laberge in March 1983 was to gain knowledge of the nature of the winter through-flow of a northern lake that has a significant winter inflow. Lake Laberge, as may be evident from Figure 2, is a deep (145 m), moderately long (45 km), and narrow (2 to 6 km) lake. The lake's residence time varies between two years in the winter to 220 days in early July. From a hydrodynamical perspective, during the ice-covered period, the through-flow is likely to be influenced mainly by viscous and diffusive effects rather than by the inertia of the inflow because the nondimensional parameter, R, based on the two-dimensional theory of Fischer et al. (1979), which characterizes these effects, has a value less than unity (0.1 to 0.5 depending on the value of the eddy diffusitivity assumed). The winter study of Stigebrandt (1978) and the summer turbidity and temperature data of Lake Laberge (Ball, 1983) suggest that the inflow might be concentrated as a thin layer of near zero-degree water, which in turn would be deflected by the earth's rotation to the right-hand shoreline of the lake. As well as investigating whether or not the inflow velocity remained concentrated, it was hoped that sufficient quantitative information could be obtained to determine such unknown quantities as the sensible heat transfer coefficient between water and ice.

To this end, the engineering literature was reviewed for suitable instrumentation. Profiles of current are routinely measured through sea ice with direct reading current meters (Baird, 1981). Because of the extremely low velocities anticipated, Baird's mechanical current meter was considered to be unsuitable. A solid state electromagnetic current meter could be ruled out on account of the low conductivity of the lake water. By a process of elimination, it was decided to purchase a lightweight direct reading acoustic current meter of Neil Brown manufacture suitable for deployment through a single 20-cm ice hole. According to the manufacturer, the threshold speed of this device is 1 cm/s, which should be able to detect flows estimated to be

about 2 cm/s based on a typical winter discharge of 160 m^3/s and river plume depths and widths observed in summer in Lake Laberge (Ball, 1983).

During March 1983, 15 combined profiles of current and temperature were taken through 60 to 100 cm of ice on the southern end of Lake Laberge at the locations shown in Figure 2.

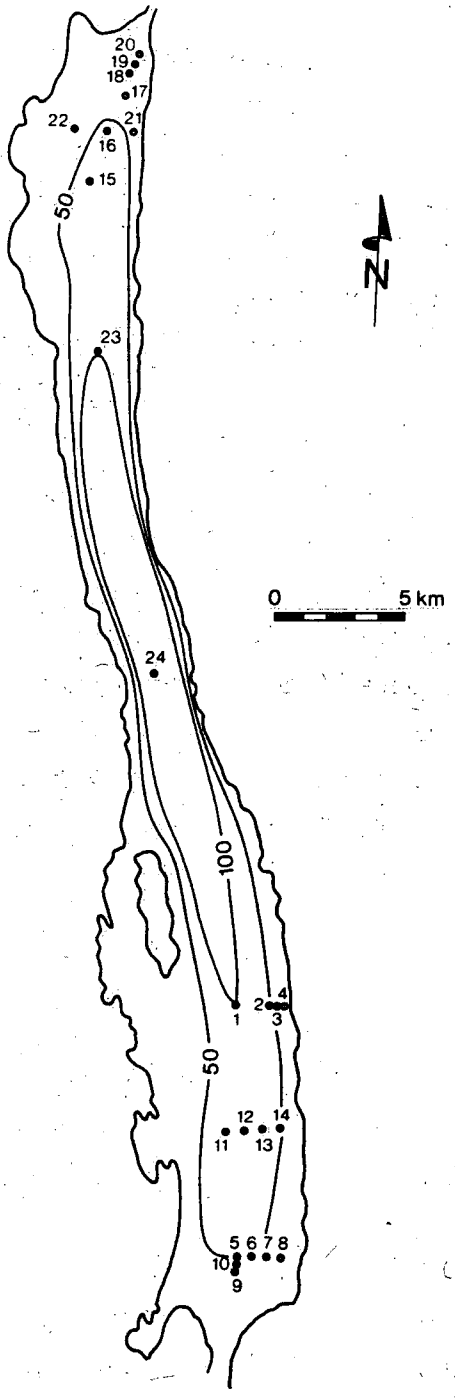

Figure 2. Lake Laberge station locations and simplified bathymetry (m).

Following a discussion of the calibration tests and field procedures, the results of the field study are given.

Current Meter

Calibrations

All calibrations were performed with the towing carriage of the National Calibration Facility to an accuracy of several percent of the true towing speed. In a preliminary test with a borrowed Neil Brown instrument from McMaster University, considerable distortion of the flow by the supports for the acoustic mirror was observed at speeds less than 5 cm/s. In the model purchased, the cross-sectional areas of the supports were reduced by a factor of approximately two. The tests were conducted to examine the low-speed response, flow distortion by the supporting struts, and the stability of the zero-speed offset on each of the two axes.

Individual calibration runs consisted of 80 to 150 readings at intervals of 0.5 s and recorded on magnetic tape. Spurious readings were eliminated from the data and then means and standard deviations were taken of the edited data. The calibrations consist of prefield and postfield tests. In all cases, the calibration facility was allowed to come to rest over a weekend period, and calibration began at low speeds progressing to higher speeds.

Prefield Calibrations

The prefield calibration results are summarized in Figure 3 for towing speeds of 0.5, 1.0, 1.5, 2.0, and 5.0 cm/s. The following features should be noted:

1. There is no evidence of shading by supports at flow angles of 0°, 90°, 180°, and 270°.
2. There is a persistent offset on the Y-channel only of 1.25 cm/s.
3. Measured speeds are consistently 93% of the true values.

4. Repeated calibration readings are within ±1 mm/s of one another with the exception of speeds of 0.5 cm/s.
5. Standard deviations (not shown) are less than 1 mm/s for speeds up to 2 cm/s and are less than 1.5 mm/s for speeds at 5 cm/s.

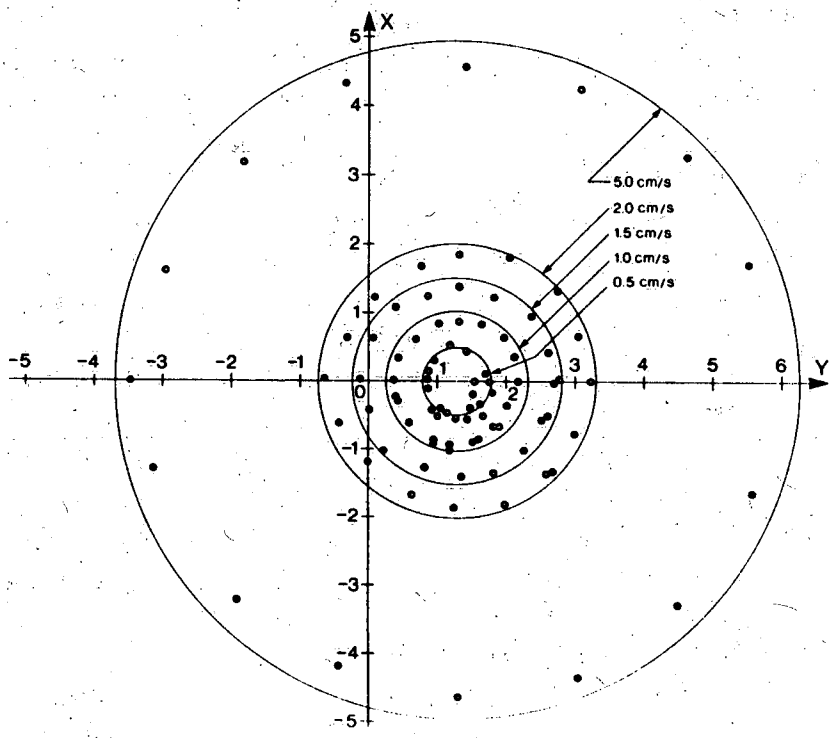

Figure 3. Tow tank calibrations of direct reading acoustic current meter prior to field deployment, January 25, 1983. Solid lines represent nominal values about the experimental offset (cm/s).

Postfield Calibrations

The postfield calibration results are shown in Figure 4 for the towing speeds of 1.0, 2.0, 2.5, and 5 cm/s. The following points should be noted:

1. The zero-speed offsets on both channels have changed from the prefield calibrations despite the installation of a new set of velocity sensors in the X-channel and the subsequent zeroing of the signal in a 1-m^3 test tank prior to the field deployment. The Y-channel has shifted to 1.6 cm/s and the X-axis has shifted to 0.25 cm/s.

2. Measured speeds are 93% of true values for the speed range of 5.0 and 2.5 cm/s, as was the case in the prefield calibration, but is 100% of true at 2.0 cm/s and only 60% of true at 1 cm/s. The reason for this observed nonlinearity in the low-speed response is not known.

3. In general, standard deviations of the flow response are somewhat larger than in the prefield calibration runs, being typically in the range of 0.1 to 0.2 cm/s.

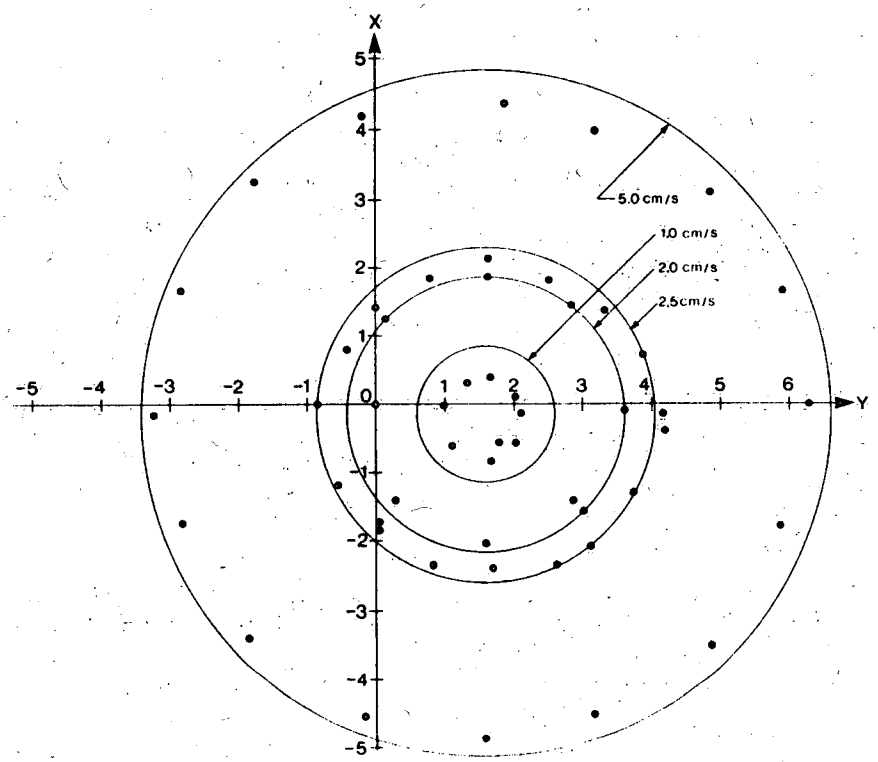

Figure 4. **Tow tank calibrations of direct reading acoustic current meter after field deployment, March 31, 1983. Solid lines represent nominal values about the experimental offset (cm/s).**

Field Deployment

The direct reading acoustic current meter was manually lowered through a machine-cut auger hole in the ice as data were simultaneously recorded at the surface on magnetic tape and viewed on a digital display. Before profiling, the acoustic transducers of the current meter were

bathed in a surface-active fluid to remove bubbles and dwelled at some depth to ensure that they were ice free. Throughout the lowering process, the current meter was periodically dwelled and slowly rotated to obtain in situ data on the offset value of each axis. In most cases, logistical support was provided by motorized toboggans, although a light aircraft was necessary for the northern half of the lake. At some stations, profiles of temperature and conductivity were taken with a lightweight profiling system. Fifteen profiles of current were taken between March 3 and March 10, when the current meter failed because of breaks in both the original and spare instrument cables. At this point, nine additional profiles were taken by the temperature-conductivity instrument.

Data Analysis

The profiles measured by the conductivity-temperature probe were corrected and reduced to standard depths by E.C. Carmack as described by Carmack et al. (1987). The data collected by the direct reading acoustic current meter were first transferred from the field audio cassette tapes to standard one-half-inch magnetic tapes and then converted to currents, temperatures, and depths according to the postfield towing tank calibration curves (Fig. 4). A typical profile consists of approximately 500 one-half-second readings evenly spaced over 42 m, the maximum length of the cable. These individual readings were scanned first automatically and then manually to flag and delete obvious errors. Profiles taken at times close to cable failure contained a high frequency of errors. Next, any offsets on the axes remaining after calibration and editing were determined from the dwells and removed from the axes. Finally, the current components were aligned in geographical coordinates. The offset data as determined from the dwells showed variation from profile to profile of about ±1 cm/s. Machine plots of current components as well as speed and directions showed irregular distributions of flow. In order to reduce the apparent noisiness of the velocity profiles, it was decided to further smooth the profile data by including only 10-point averages and the mean values of the flow at the dwells. In nearly all cases, the smoothed profiles still exhibited inconsistent results. It was concluded

that the flow field in the winter is generally less than 2 cm/s, a figure that is taken to be the effective threshold of the acoustic current meter in the field, despite the laboratory repeatability of about 0.5 cm/s once the offsets are taken into account.

Profiles of the east and north current components at station 9 about 100 m to the north of the inflow plotted in Figure 5 are probably the only reliable cast taken. As expected, there is a northerly component near the surface overlying a surprisingly strong counterflow, presumed to be an entrainment-induced return flow.

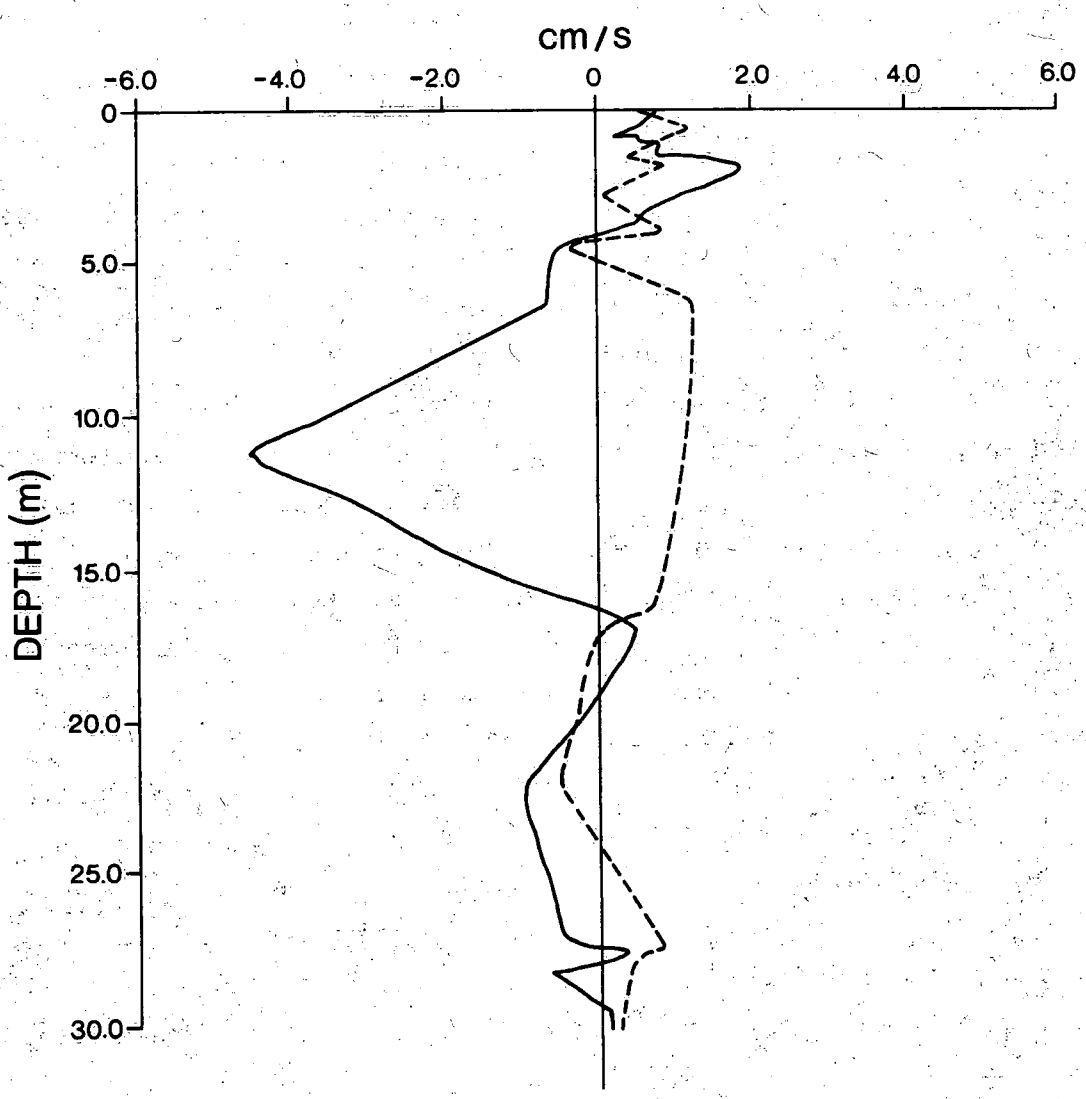

Figure 5. East component of flow (dashed line) and north component of flow (solid line) at station 9, March 8, 1983.

The transverse temperature section at the northern end of Lake Laberge (Fig. 6) generally shows warmer water on the western shoreline in the upper 10 m consistent with the expected slope of the isotherms required to balance the northward through-flow. On the other hand, a section in the southern portion, which is based upon the current profiles, but which, unfortunately, is incomplete, suggests a southerly flow at depths around 20 m along the eastern shoreline from the tilt of the 1°C isotherm (Fig. 7). A temperature section along the north-south axis of the lake (Fig. 8), based on a combination of temperature data from the conductivity and current profilers, suggests that there is a mixing zone within the nearest 5 km from the inflow, where a thin, cold layer of water is formed that overlies a shallow thermocline at a depth of approximately 10 m. The draw-up of warm water into the outflow may also be noted due to the process of selective withdrawal. Below the withdrawal level, the 1.2°C isotherm is deflected downwards at the outlet consistent with a downwelling of water probably due to a weak return flow

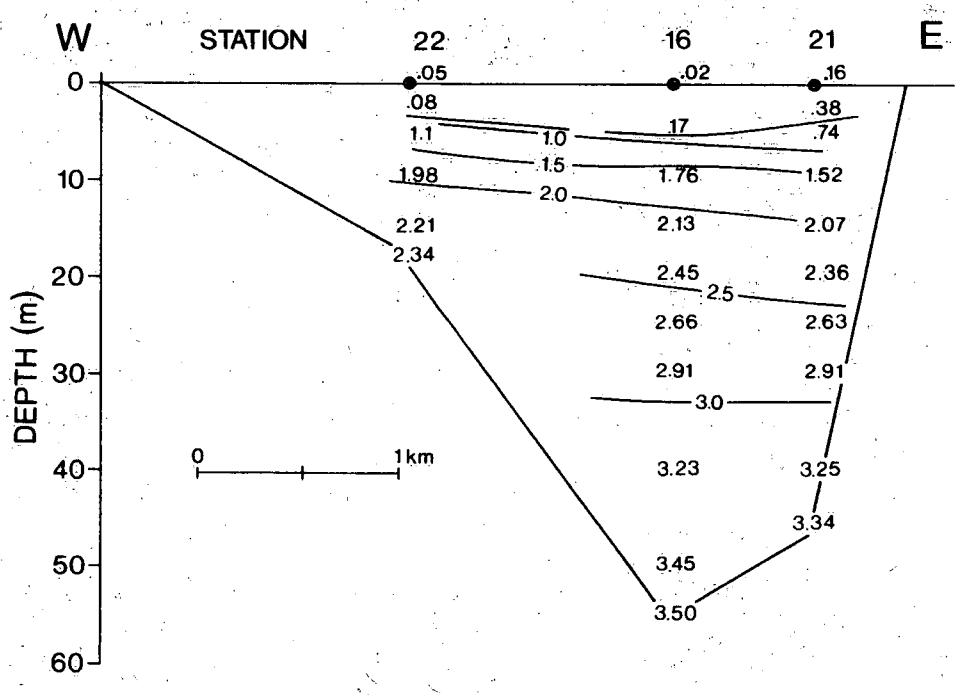

Figure 6. Transverse temperature distribution at north end of Lake Laberge, March 11, 1983 (°C).

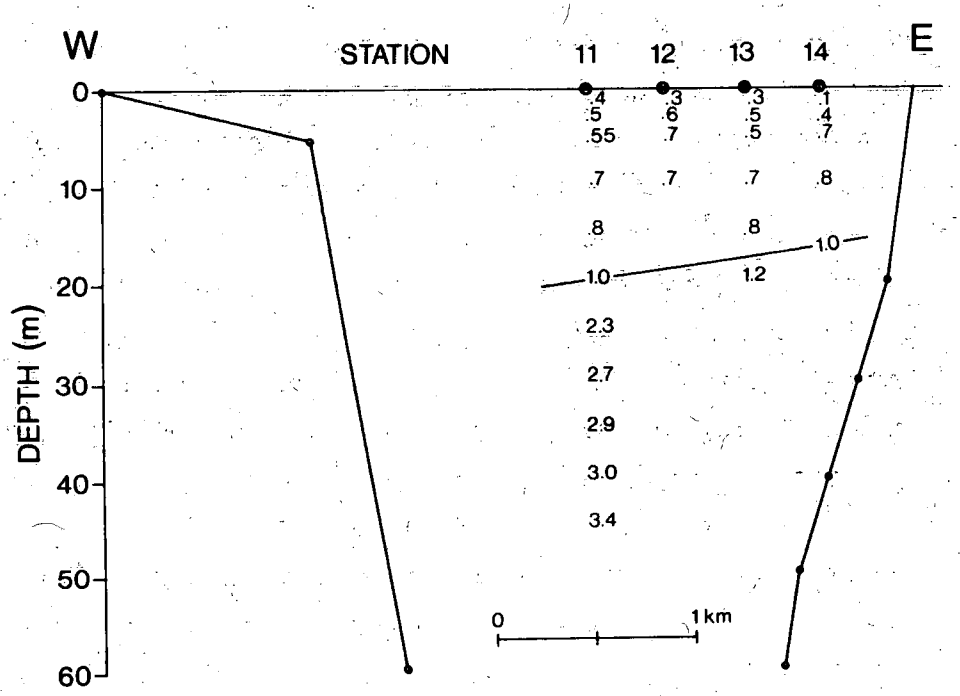

Figure 7. Transverse temperature section at south end of Lake Laberge, March 9, 1983 (°C).

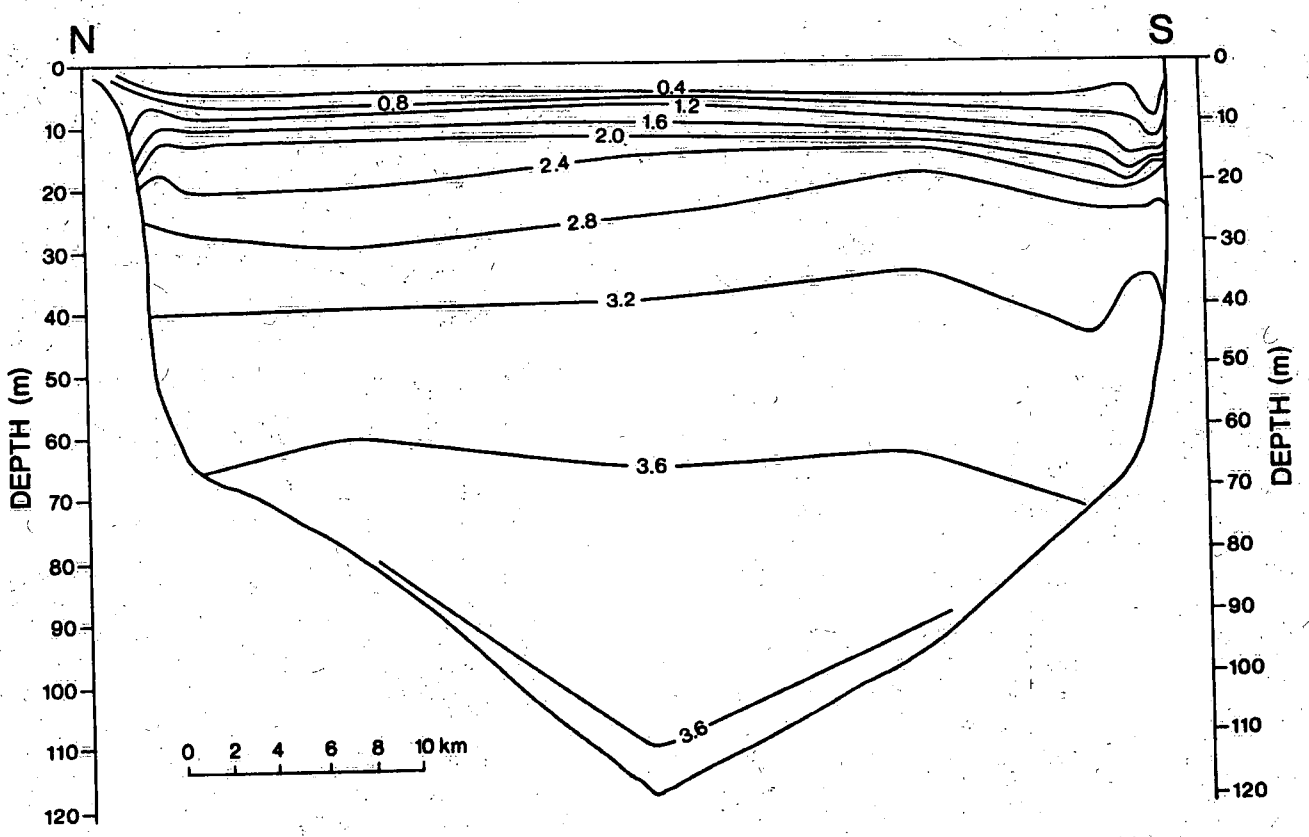

Figure 8. Longitudinal temperature section, Lake Laberge, March 8-11, 1983 (°C).

below the surface overflow. This weak return flow may extend as far south as the inflow, where it could be responsible for upwelling of the isotherms there, as well as accounting for the apparently weak southward flow seen in the current readings of Figure 5. The main features of the temperature section of Figure 8 are also found on three additional sections presented by Carmack et al. (1987).

Finally, the ice thickness measurements made during the survey are summarized in Figure 9. The thickest ice occurs in the shallow embayments on the western half, while the thinnest ice is found at the inflow and near the outflow. There does not appear to be a region of thin ice along the eastern shoreline, as found in some northern lakes (Stigebrandt, 1978), where the inflow is concentrated. Instead, on the basis of ice thicknesses, the through-flow seems to be well distributed across the lake.

On March 6 at station 4, a submersible shortwave radiometer was lowered through the ice to 1.8 m below the water-ice boundary. At noon, the snow albedo was 0.77; the extinction coefficient for the 21-cm-thick layer of snow was 10 m^{-1}; for the 55-cm layer of ice, 1.8 m^{-1}; and for the water, 0.4 m^{-1}. On March 8, these measurements were repeated at station 10 at 1115 local time. On that occasion, the albedo was 0.87 and the extinction coefficients of snow, ice, and water were 5.2 m^{-1}, 2.2 m^{-1}, and 0.3 m^{-1}, respectively. These measurements are similar to published values of albedo for new snow of 0.85 and extinction coefficients of snow and ice of 6 m^{-1} and 1.5 m^{-1}, respectively (Patterson and Hamblin, 1988). The average winter albedo is 0.75 (Carmack et al., 1987). The extinction coefficient for water under ice may be compared to the summer values, 0.2 to 3.6 m^{-1}, inferred from the turbidity and Secchi disc measurements of Ball (1983). These data are required for the thermodynamic modelling of ice-covered lakes.

Conclusions

The expected flow concentration of the through-flow was not observed and hence the under-ice currents were too low to be discerned by

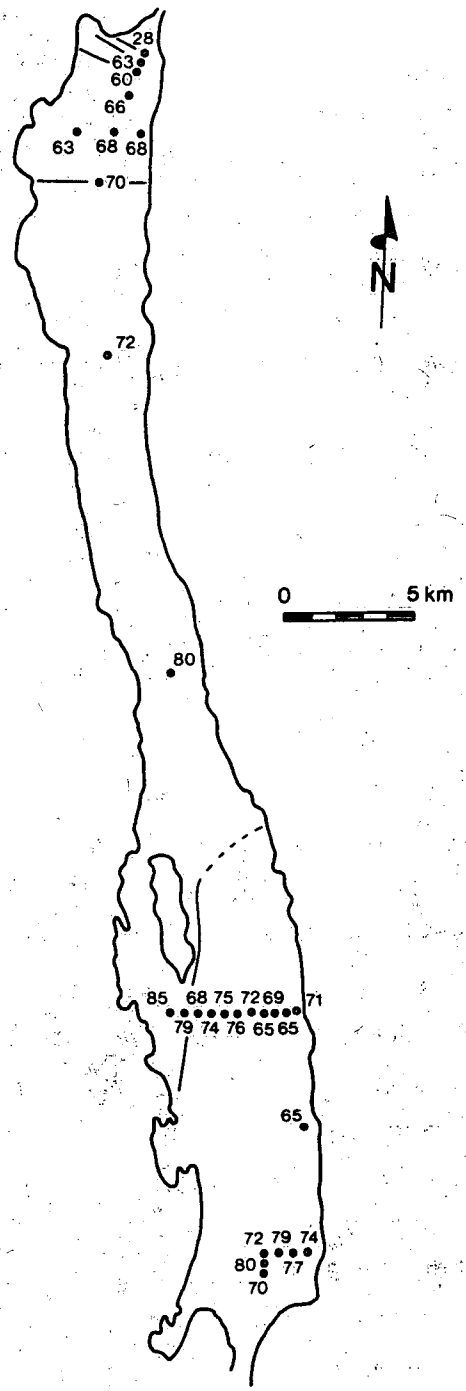

Figure 9. Ice thickness (cm), Lake Laberge, March 3-11, 1983.

an acoustic profiling current meter whose effective threshold current proved to be as large as several centimetres per second in the field. Instead, a qualitative picture of the winter through-flow was inferred

from temperature readings by assuming in the longitudinal plane that isotherms correspond to streamlines and that in the transverse plane, the thermal wind relation applies. It was concluded that the through-flow is uniformly distributed across the lake in the upper 10 m of the water column, which would result in an average flow of 0.4 cm/s. Below this northward-flowing layer, there is evidence of a weak southward return flow from one end of the lake to the other. The current measurements were not sufficiently reliable to permit the sensible heat transfer coefficient to be determined. It is recommended that additional field measurements employing a different system of current measurements be taken and that numerical modelling studies of the through-flow dynamics be initiated.

PART II: OUTFLOW CIRCULATION STUDY IN MARSH AND TAGISH LAKES, MARCH 1985

Field Equipment

The study at Lake Laberge in 1983 revealed the limitations of a conventional current meter in such low flow conditions and in such harsh environments as ice-covered lakes. Therefore, for the 1985 study at Marsh and Tagish lakes, it was decided to design a drogue suitable for under-ice deployment, tracking, and recovery in remote locations. This system consisted of a square sail, 10 m^2 in area, made out of Dacron spinnaker cloth, and weighted by an 18-kg anchor rod. The roller blind drogue was attached to a cylindrical subsurface float ballasted to a positive buoyancy of 10 to 30 g. Thus the horizontal drag of the polystyrene sphere, which formed the uppermost portion of the subsurface float next to the ice, would be expected to be only several grams force. The drogues were tracked under the ice by means of a radio location system employing transmitters attached to the subsurface float. The entire drogue system was capable of being deployed and retrieved through a machine-made auger hole in the ice 20 cm in diameter. An illuminating periscope fitted with a plumber's snake and hook greatly aided the retrieval, as did a line attached to the anchor, which allowed the sail to be collapsed in place. Because of air trapped in the seams of the sail, it was necessary to presoak the drogues in situ for 24 hours prior to release. Additional details, design calculations, and laboratory tests of the drogue behaviour are provided in Appendix A.

Another novel feature of this study was the use in lakes of a conventional mechanical current meter designed for river surveys. Deployment of the Price meter was possible in extremely shallow outflow regions since the flow velocity close to the river mouth often exceeded the threshold speed of the meter of 2.5 to 3 cm/s, and because the clarity of the water permitted the flow direction to be observed visually from a neutrally buoyant streamer attached to the current meter. An Applied Microsystem conductivity and temperature profiler completed the instrumentation system.

Marsh Lake Observations

Marsh Lake was chosen for the first field trial because of its proximity to the National Water Research Institute field station and the Water Survey of Canada office in Whitehorse, Y.T. On account of the extremely cold weather preceding and during the experimental period, the outflow polynya was frozen over. The complex outflow geometry and bathymetry of Marsh Lake relative to Lake Laberge and Tagish Lake are evident in Figure 10. Depths, which were determined from the profiler, suggest the presence of a deep channel along the eastern shoreline that crosses to the opposite shoreline along the northern portion of the island. At the northwestern tip of the island, the outflow passage, which is located closer to the island than the mainland, has a maximum depth of only 4 m.

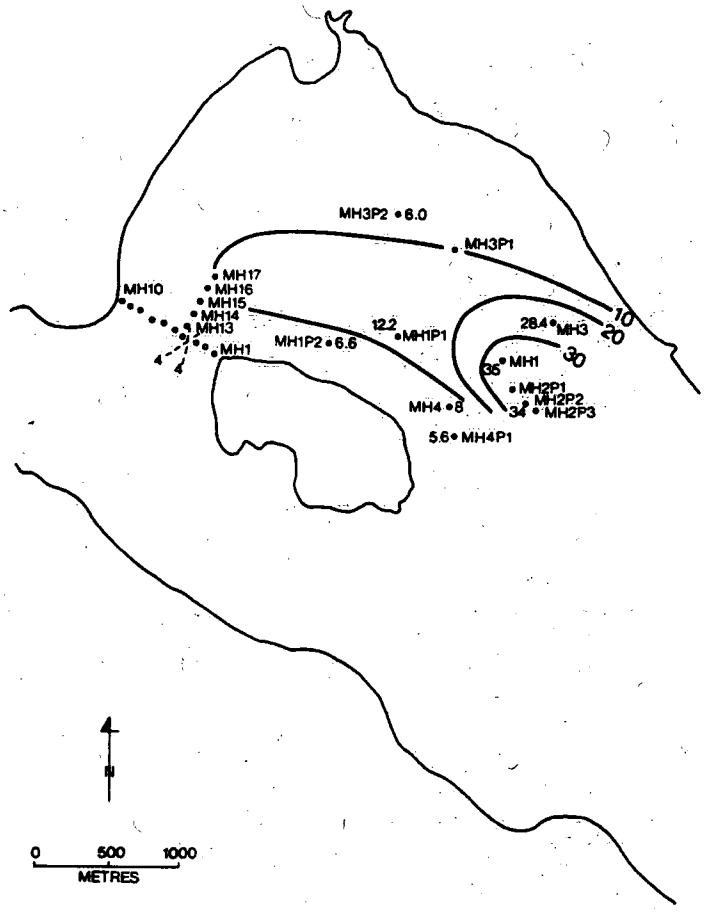

Figure 10. Marsh Lake station locations and bathymetry (m) in outflow region.

Drogue trajectories in Marsh Lake are shown in Figure 11 for drogues set in all but one case at a depth of 6 m, which, unfortunately, was as close to the surface as possible because of the size of the drogue, floats, and bridle. It may be noted that the drogue averages the flow over the range of depth of 4.3-7.6 m. The drogues indicated a flow more or less parallel to the bathymetric contours in the direction of the outflow on the eastern half of the lake and in the reverse direction on the western half. Counterflow is also found in the centre of the lake at a depth of 10 m. In all cases, except for the 10-m depth trajectory, the drogues grounded after a day or two. Thus, it is impossible to calculate speeds accurately except at the release points MH17, MH3, and MH1. The speed and directions from the drogues at 6-m and 10-m depths are combined with the Price current meter measurements in Figure 12. It is apparent that the speed of flow is well below the threshold of mechanical current

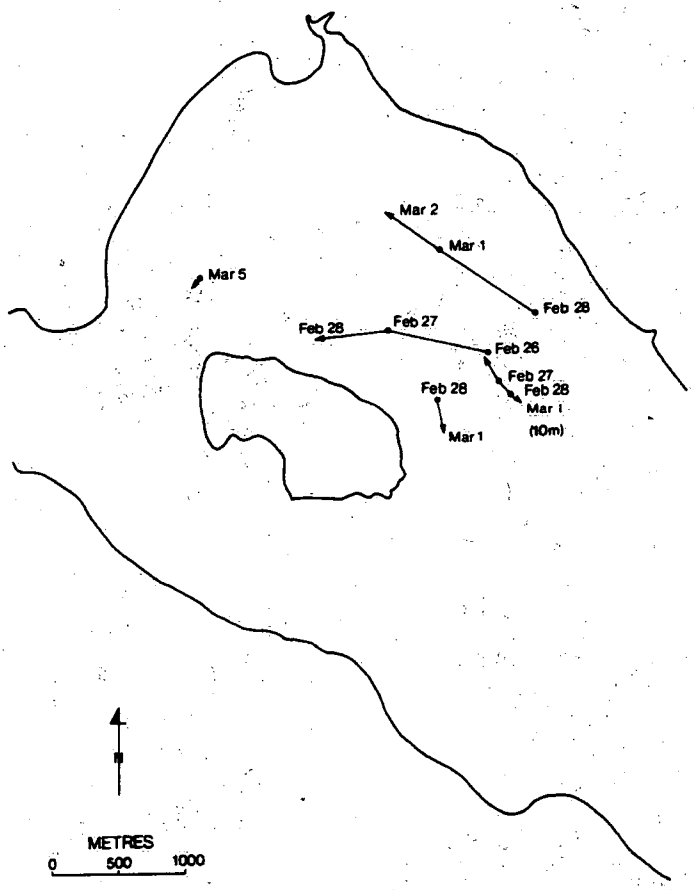

Figure 11. Marsh Lake drogue trajectories, February 26 to March 5, 1985. All drogues are set at 6-m depth unless otherwise noted.

meters, except in the confined outflow passage. The outflow regime, then, appears to be a flow along the northeastern shoreline that supplies the outflow, which, in turn, is concentrated on the left-hand side (in the direction of flow) of the narrow outflow passage. Lake water entrained into the Yukon River through-flow is returned to the open lake by both flow along the western shoreline and counterflow at deeper levels.

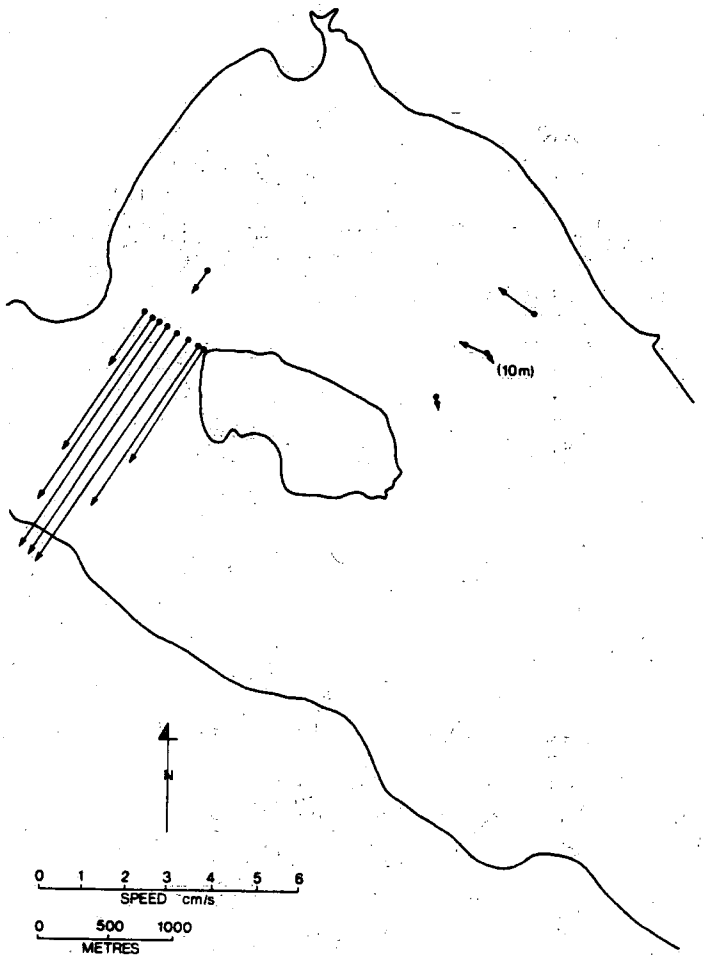

Figure 12. Marsh Lake currents, February 26 to March 5, 1985. Current in the narrows to north of island is measured by a current meter. At other locations, flow is from drogues at 6-m average depth unless otherwise indicated.

The concentration of the outflow along the eastern shoreline at the line MH4 to MH3 is substantiated by the northward flow inferred from the combination of drogue and temperature data, shown in Figure 13. The velocity section of Figure 13b is computed from the transverse density

gradients associated with the sloped isotherms shown in Figure 13a through the well-known thermal wind relation and employing the drogue current at one or more levels to supply the required constant of integration. The thermal wind relation quantifies the tendency of the heavier water on the western side to flow under the lighter water of the eastern side and in the process to be deflected to the south by the earth's rotation while the lighter water is turned to the north.

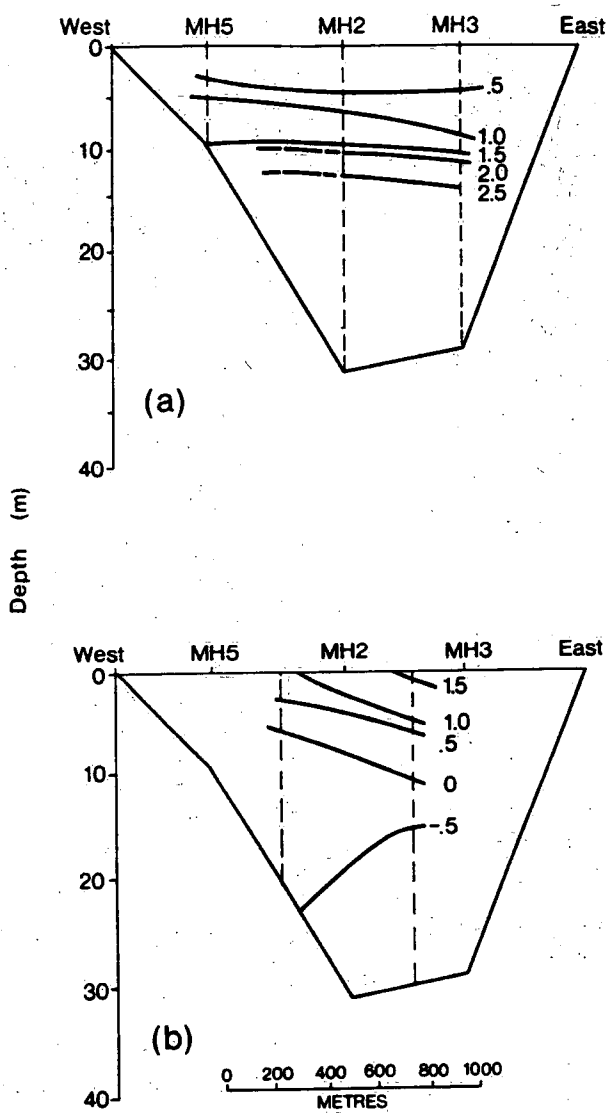

Figure 13. Marsh Lake, February 27, 1985, station MH5-MH3. (a) Temperature section (°C). (b) Northward flow (cm/s, positive to north).

Tagish Lake Observations

It was desirable to determine the outflowing circulation in a simpler setting than that offered by Marsh Lake. Tagish Lake was chosen because of its simple geometry, fairly safe ice, well-defined polynya, and the proximity of suitable lodging for a field party. The sampling network is shown in Figure 14. The bathymetry of the outflow region of Tagish Lake (Fig. 15) is somewhat better defined than in Marsh Lake by a denser coverage of stations. Tagish Lake similarly has a deep outflow channel that crosses from the centre of the lake to the westward shoreline.

Drogues positioned along the line 1–8 could not be released simultaneously for logistical reasons. The trajectories of the first batch of three are shown in Figure 16 and the second release, two days later, in Figure 17. All drogues were released at an average depth of 6 m, except for an intermediate depth drogue, which was released at 9.6 m at station 6. The subsurface float of the deep drogue at station 6 reentered the ice hole and could not be used.

The fact that the drogue paths appear to cross over one another when released concurrently is sufficiently remarkable to demand further comment. Either the drogues do not faithfully follow the streamlines or the outflow circulation is highly unsteady. The first explanation is supported to a certain extent by the tendency of the drogues to ground in Marsh Lake. Therefore, a postfield laboratory test of the drogues was undertaken and is described in Appendix A. The stability of the outflow current will be investigated in the section on outflow stability.

Despite these uncertainties in drogue behaviour, the drogue speed normal to the line 1–8 served as the reference value of flow in the application of the thermal wind equation to the cross section. Since there were many more temperature and drogue readings across Tagish Lake than Marsh Lake, it is reasonable to compute the total transport and compare it to the river discharge. The reference currents at 6 m depth

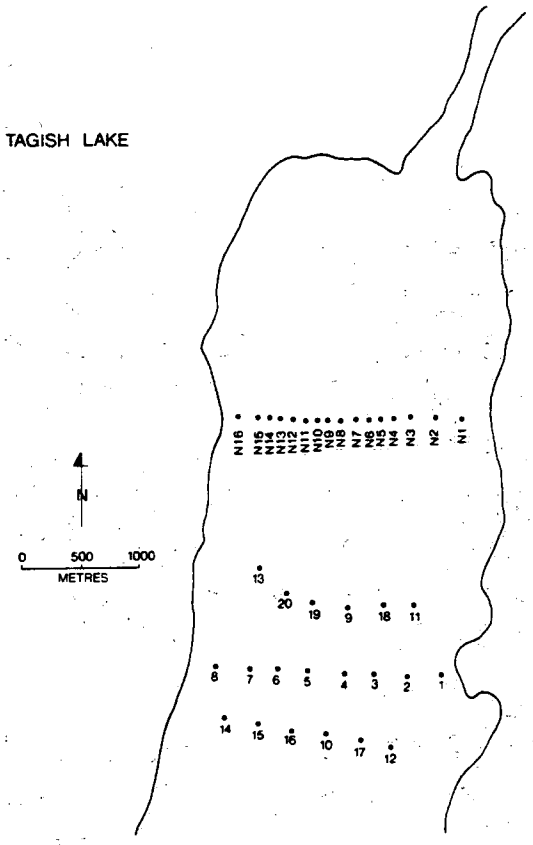

Figure 14. Station locations in outflow region of Tagish Lake.

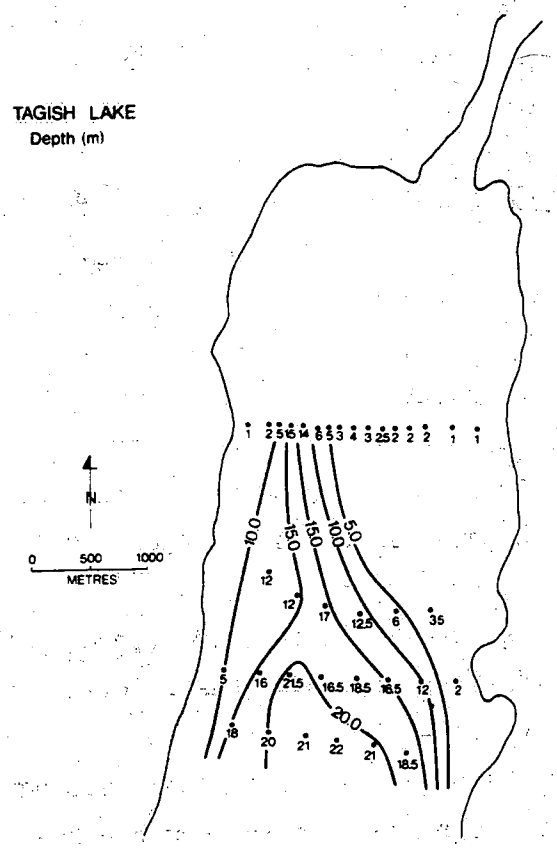

Figure 15. Bathymetry (m) in outflow region of Tagish Lake.

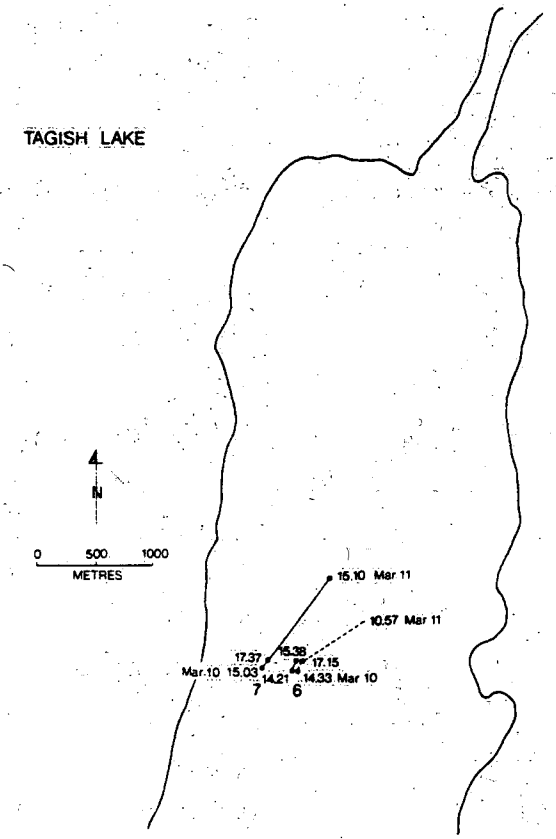

Figure 16. Drogue trajectories, March 10-11, 1985. Depth 6 m (solid line); depth 9.6 m (dashed line).

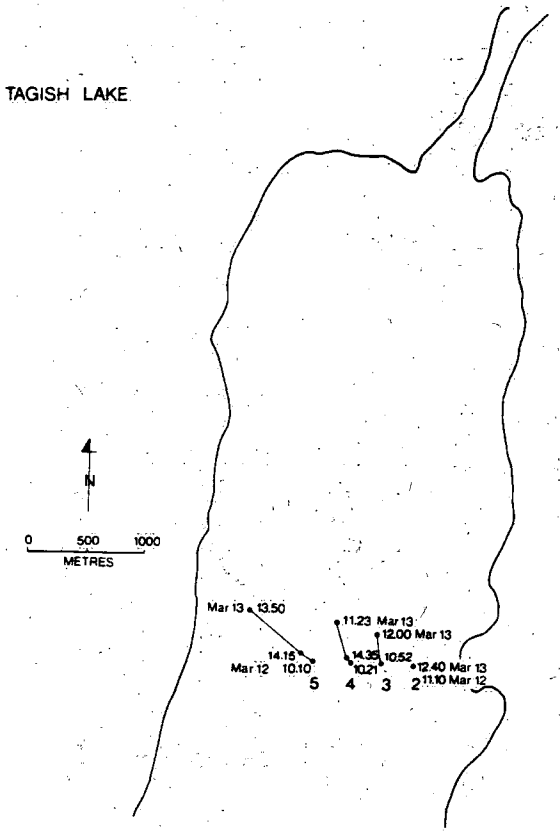

Figure 17. Drogue trajectories, March 12-13, 1985. All drogues at 6-m depth.

were adjusted slightly about the observed values to bring the cross-sectional transport into exact agreement with the winter discharge of the Yukon River of 140 m^3/s even though the observed reference currents yielded reasonable agreement. The pronounced tilting of the isotherms seen in Figure 18a is consistent with a highly concentrated northward flow off centre to the western side of the lake between stations 5 and 6 and at a depth of 3 m seen in Figure 18b. Weak northward currents are found on the eastern side of the lake, while slow return flow obtains in the lowest 5 m on the western side of Tagish Lake.

Although there were no drogue measurements on the transverse lines to either side of line 1–8 and the density structure is more poorly defined, the thermal wind method was applied assuming the same nominal values for the reference velocities and that the total transport is equal to the river discharge. Perhaps then it is not surprising that much the same pattern of northward flow emerges in Figures 19 and 20. The major

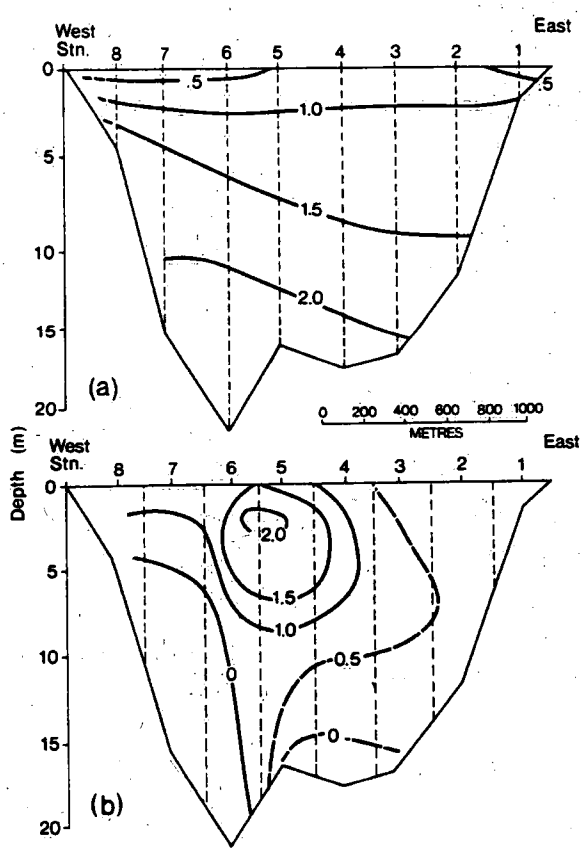

Figure 18. Tagish Lake, March 6, 1985, stations 1–8. (a) Temperature section (°C). (b) Northward flow (cm/s).

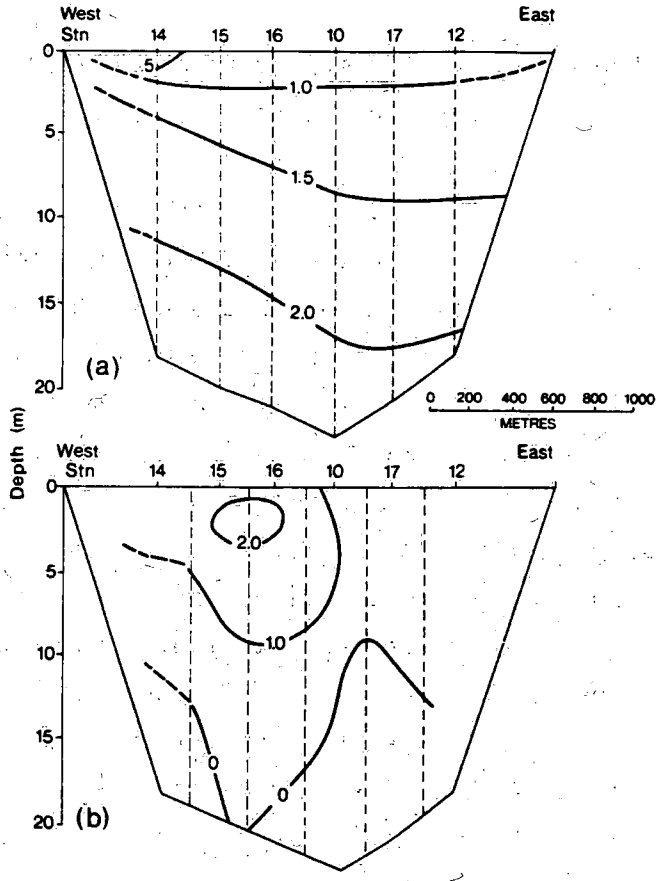

Figure 19. Tagish Lake, March 7, 1985, stations 14–12. (a) Temperature section (°C). (b) northward flow (cm/s).

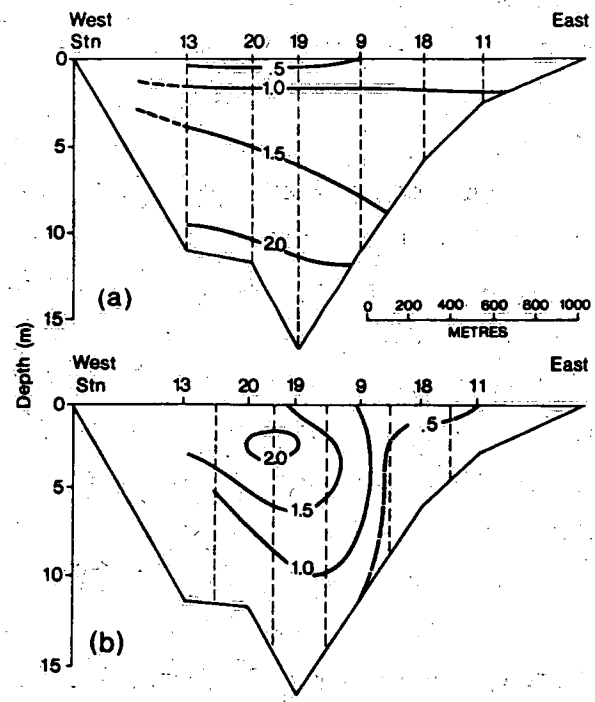

Figure 20. Tagish Lake, March 7, 1985, stations 13–11. (a) Temperature section (°C). (b) Northward flow (cm/s).

difference is that the return flow decreases closer to the outflow until at line 13–11 there is no apparent southward flow.

An additional striking feature of the temperature sections of Figures 18 to 20 is the enhanced near-surface temperature of Tagish Lake compared to that of Marsh Lake. While the temperature is nearly the same at 10 m and even less at depths of 20 m, the average temperature at 1 m depth is 0.8°C compared to 0.16°C in Marsh Lake. The reason for the low surface temperatures in Marsh Lake is unknown, but is conjectured to be associated with the relatively short transit time (about 20 days) between the inflow and outflow in Marsh Lake compared to a much longer time in Tagish Lake. For example, if a vertical eddy diffusivity of 0.4 cm^2/s is assumed to hold in the upper 10 m of Marsh Lake on average, then it would take about 30 days for heat to diffuse from 10 m to the surface, which is greater than the travel time of inflow water through Marsh Lake. Unfortunately, because of an instrumentation failure, the temperature of the inflow required to make the calculation more precise could not be determined. In any case, the much colder near-surface water in Marsh Lake is likely to be responsible for the disappearance of the outflow polynya during the coldest part of the winter. This assertion will be quantitatively tested in the section on the sensible heat transfer between water and lake ice.

The observed drogue current at 6 m is extrapolated to a depth of 1 m by the thermal wind method and is plotted along with the Price current measurements made on March 12, 1985, in shallow water in the vicinity of the ice edge in Figure 21. Accompanying these flow vectors, the temperature at 1 m is plotted in Figure 21. In the deeper area, flow is concentrated in the western half of the lake, but closer to the polynya there is appreciable flow at 1 m at several locations along the shallow flanks of the channel at the eastern side of the lake. Unlike in Marsh Lake, where the outflow polynya had recently frozen over and cut off the effects of the wind, in Tagish Lake, the open water was fully exposed to a wind strength estimated to be 60 km/h when the observations were taken. It is possible that the large flows outside of the channel

are due to transient wind effects and are not directly related to the outflow current. Temperature at 1 m is generally lower where the current is strongest on the western side of the lake.

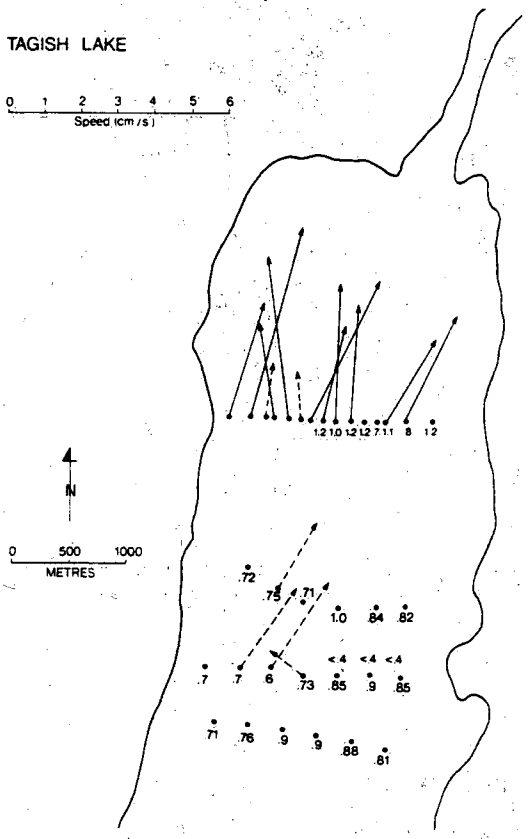

Figure 21. Current and temperature (°C) at 1-m depth (solid line), measured; dashed line, inferred).

Finally, the ice thickness distribution is presented in Figure 22 for the period March 6–12, 1985. Clearly, there is a significant cross-lake gradient in ice thickness as well as a less pronounced longitudinal thickening away from the outflow. Since the ice thickness distribution may be viewed as a long-term integrator of both the distribution of heat and flow in the lake, two factors are suggested: the tilting of the isotherms brings warmer water to the upper levels along the western shoreline and the stronger flow there also is responsible for increased turbulent transport of heat to the ice from the water. The data collected during the field experiments will serve to quantify these ideas and in particular to deduce the coefficient of sensible heat transfer from water to ice.

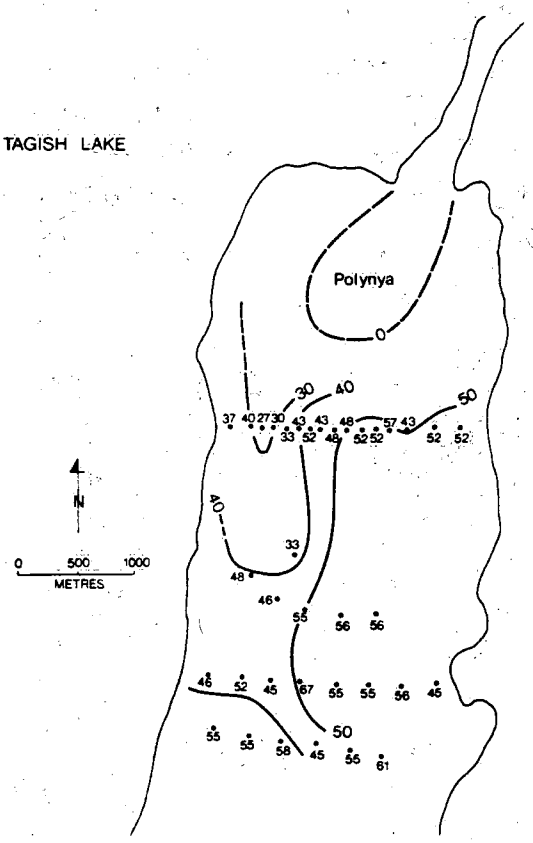

Figure 22. Measured ice thickness (cm) at Tagish Lake, March 6-12, 1985. The approximate margin of the ice edge is estimated and given by the dashed line.

Thorpe Length Scale

During the temperature survey of Marsh Lake, pronounced temperature inversions were noted in the upper layers of stations MH3, MH1, and MH1P1. These inversions were also reflected in the associated conductivity profiles. Since it seemed unlikely that the temperature inversions were instrumental in origin, it was supposed that they represented shear-induced overturning events and were thus amenable to the analysis described by Dillon (1982). As an example of one of these profiles, the one at station MH3, shown in Figure 23, was chosen since estimates of vertical shear were available from the previous analysis.

The first step of the analysis is to reconstruct the original temperature profile here by the objective method described by Papadakis (1981), which is shown as a dashed line in Figure 23. The vertical displacement of each point from its original position is determined. The root mean square vertical displacement for the overturning event, known as the Thorpe length, L_T scale, is 0.9 m for the profile at MH3. The

Ozimidov length scale has been shown by Dillon (1982) to be 80% of the Thorpe scale under most conditions. In turn, the vertical eddy diffusivity, kv, may be shown to be given by

$$k_v = \text{eff } (0.8\ L_T)^2\ N$$

where N is the stability frequency at temperature T given by $N^2 = 1.33 \times 10^{-4}\ (T-4)\ \partial T/\partial Z$ and the vertical temperature gradient is given in degrees Celsius per metre. If the efficiency of conversion of turbulent kinetic energy to potential energy, eff, is assumed to be 5% (Fischer et al., 1979), then for the observed N of $7.1 \times 10^{-3}\ s^{-1}$, the vertical eddy diffusivity is 1.8 cm^2/s. In the light of the previous calculation, this estimate is apt to be an upper limit for the vertical eddy diffusivity in Marsh Lake.

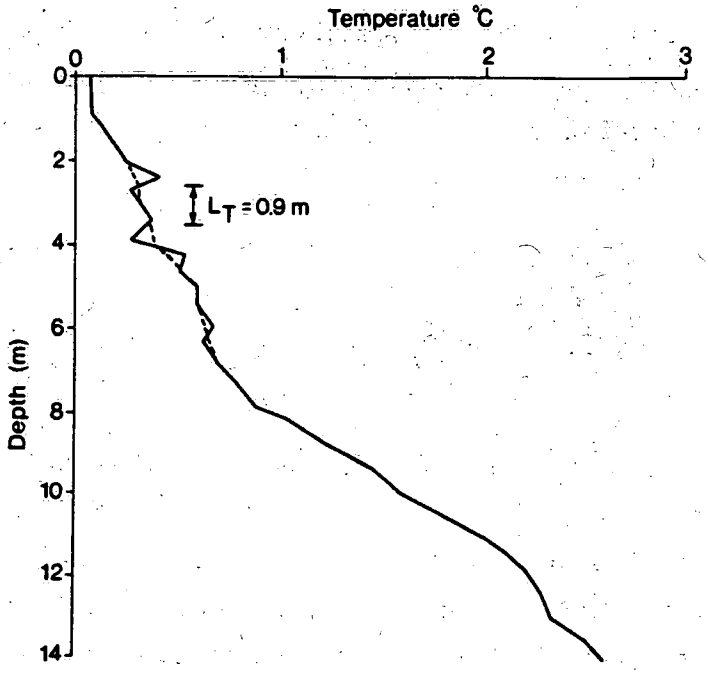

Figure 23. Marsh Lake, February 27, 1985, station MH3. Upper portion of observed temperature profile (solid line), monotonic profile (dashed line).

The gradient Richardson number for this event may be roughly estimated from the thermal wind relation and the stability frequency to be 3. Although this value is too high to account for the overturn, it

must be borne in mind that the geostrophically determined shear over a baseline of 500 m probably greatly underestimates the true local shear. It is notable that the three overturning events were observed to occur on the eastern half of the lake where the vertical shear is likely to be highest. Similar overturning events in the inflow region of Lake Laberge were observed by Carmack et al. (1987).

Outflow Stability

One possible explanation for the observed deviation of outflow direction in Tagish Lake (Figs. 16 and 17) is that the concentrated outflow current is unstable and hence meanders from one side of the lake to the other. Physically this would appear to be unreasonable due to the confining influence of the longitudinal shoreline of the lake. In order to investigate this hypothesis further, a formula for the instability of sheared flow in a stratified rotating channel of constant depth was evaluated using the approximate geometry and stratification of Tagish Lake. According to the Eady model reported by LeBlond and Mysak (1978), disturbances of wavelength, λ, or greater, are possible in channels of breadth, l, if

$$\left(\frac{\lambda}{2\pi}\right)^2 > \frac{1}{\frac{5.8}{r^2} - \left(\frac{n\pi}{l}\right)^2}$$

where r is the Rossby radius of deformation, in the case of the Tagish outflow, 0.8 km. If we take as the channel width the width at the mid-depth of line 1–8 of 1.6 km, then disturbances with wavelengths at least as long as 2.7 km would be unstable, which is possible in Tagish Lake. Note that the cross-channel mode, n, must be unity, meaning that higher cross-channel modes are always stable. Furthermore, it is of interest to evaluate the periodicity of this disturbance. From the Eady model, the disturbance propagates with half the mean speed. With an assumed mean speed of 1 cm/s at station 8, the period of the wave would be 6.25 days. Thus the two-day period between the drogue experiments of Figures 16 and 17 would be nearly sufficient for the flow to shift from,

say, a peak to a trough of the wave. Because of the extremely approximate nature of the theory of baroclinic stability, all that can be concluded from this analysis is that the observations are consistent with the theory, but it may not be proven with absolute certainty that the apparent deviation of the drogue tracks is due to the instability of the outflow.

It is of some interest to investigate the Marsh Lake outflow for baroclinic instability. Since the inflow has not mixed with the deeper layers to the same extent as in Tagish Lake, a more appropriate idealization of the thermal structure is a two-layer model. In this case we may take from Figure 13 the upper layer as 10 m depth, the lower layer as 20 m, and mean layer temperature of 0.75°C and 2.5°C, respectively. Assuming a width of the lake, l, at the depth of the thermocline of 1300 m, we have from LeBlond and Mysak (1978) for instability $(2\pi/\lambda)^2 > (1/r)^2 - (n\pi/l)^2$ where r is the two-layer Rossby radius of deformation. Since λ^2 is negative even for the first mode, it would appear that the outflow Marsh Lake is stable.

The interpretation of the somewhat irregular behaviour demonstrated by the drogue paths put forth here is baroclinic instability. The recent laboratory experiments of Monismith and Maxworthy (1988) have shown that large eddies form near the outflow at a later stage of transient withdrawal from a rotating stratified box. Their experiment differs from the lake outflow as in their experiment the free surface is drawn down.

Sensible Heat Transfer Between Water and Lake Ice

Analysis

Transports in turbulent boundary layers are often represented for the purposes of engineering calculations by bulk transport formulas. By analogy with the atmospheric boundary layer, where fluxes are parameterized normally in terms of mean quantities measured at a height of 10 m above the boundary, in the case of ice, the quantities will be

taken at a height of 1 m below the boundary. From the requirement for continuity of stress across the air-water boundary and from the proportionality of boundary layer thickness to the friction velocity, the height in water is of the order of $\sqrt{\rho_{air}/\rho_{water}}$ of the height of atmospheric boundary layer. Although the height would be only about 30 cm employing this reasoning, 1 m is chosen for the sake of convenience.

The sensible heat flux, H, in a turbulent atmospheric boundary layer is given by

$$H = \rho\ C_s\ C_p\ \Delta T\ U \qquad (1)$$

where ρ is the density, C_p the thermal heat capacity, ΔT and U are the air-water temperature difference and flow evaluated at a height of 10 m, and C_s is the sensible heat transfer coefficient of value 1.5×10^{-3} (Fischer et al., 1979). However, they note that this coefficient could vary from 0.8×10^{-3} for very stable conditions to 1.6×10^{-3} for very unstable conditions. While this sensible heat transfer coefficient has been found by Gilpin et al. (1980) to vary between 0.6 and 1.0×10^{-3} in the laboratory, depending on ice conditions, it had not to the writer's knowledge been observed in the field prior to the initiation of the study. It is proposed to infer C_s appropriate to the turbulent boundary layer on the underside of the ice by four independent approaches and the data base collected during the study. It is assumed that flow next to the ice is sufficiently vigorous to create a turbulent boundary layer.

It may be noted from Figure 24 that the temperature at 1 m is constant normal to the outflow. Thus the heat advected horizontally into a control volume encompassing the 0.5°C isotherm must equal the heat flowing out. Therefore, only heat transfers in the vertical need be considered. The vertical diffusive flux of heat may be written as $\rho C_p k_v\ \partial T/\partial Z$ and the advective flux as $\rho C_p k_v$ WT where W is the vertical velocity. Then it follows that

$$C_s = \frac{WT + k_v \frac{\partial T}{\partial Z}}{UT}$$

Here W is estimated to be 2.4 x 10^{-3} cm/s from the slope of the 0.75°C isotherm and the drogue speed at station 17 along with the assumption of $U \cdot \nabla T = 0$. If U is taken to be 6 cm/s from the measurement at station 4/11 and k_v is 1.0 cm^2/s, which is within the limiting values established earlier, then C_s = 1.2 x 10^{-3}. In the estimation of the vertical flux of heat, the diffusive flux is twice the advective flux. The principal shortcoming of this method is the assumption of a value for k_v and the poor knowledge of W.

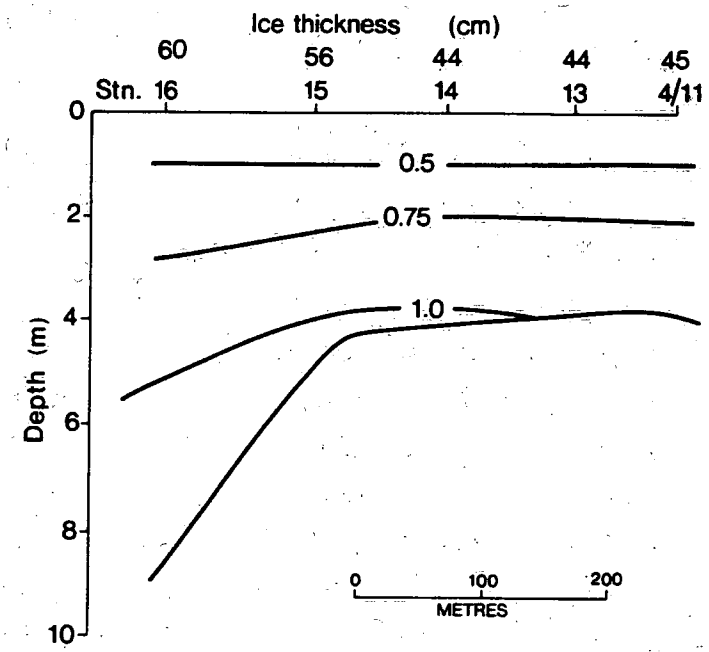

Figure 24. Temperature section (°C) of the outflow region of Marsh Lake, March 3, 1985.

As a second approach, the control volume may be taken between the surface and bottom at stations 16 and 4/11 in Figure 24. The horizontal flow at station 16 was not measured directly, but may be inferred from the conservation of mass. If no heat flux is derived from the bottom sediments, the conservation of heat equation again gives C_s

$$C_s = \frac{\int_0^{h_{16}} T_{16}\, U_{16}\, dz - \int_0^{h_{4/11}} T_{4/11}\, U_{4/11}\, dz}{\bar{U}_1\, \bar{T}_1\, l}$$

For the purposes of this calculation, the velocity profile is assumed to vary parabolically such that the transports through each station are equal, the horizontal separation between the stations, l, is 400 m, and U_1 is the average 1-m flow over 1 assumed to be 4.9 cm/s. From the observed temperature readings at each station, C_s is determined to be 5.7×10^{-3}. This method is probably less accurate than the previous one as it could be in error due to uncertainty in the assumption of a parabolic velocity profile particularly at station 16. It is possible that the flow is asymmetric with larger transport in the upper half so that heat flux through station 16 is too large resulting in a corresponding overestimate of C_s.

To further investigate the possibility of an overestimation of the horizontal heat flux from the parabolic profile, an asymmetric current profile was assumed based on the roughness differences between ice and the bottom according to the river measurements of Alford and Carmack (1987). This assumption reduced the value of C_s somewhat to 5×10^{-3}. A further source of asymmetry in the velocity profile is due to the influence of stratification of the outflow or selective withdrawal, which acts to supress the vertical component of the flow and enhance the outflow beneath the ice. A two-dimensional numerical model of the outflow was developed, which is described in Part III. The model calculation yielded a value of C_s of 3.7×10^{-3}, which may still be too large. It is concluded that the flow field near the outflow is sufficiently three-dimensional in nature to invalidate a two-dimensional assumption.

A third method is motivated by the ice thickness in the outflow region, which was seen to vary inversely with the velocity at 1 m. For example, the ice thickness is 45 cm at station 4/11 where the speed is 6.2 cm/s, while at station 16 the ice thickness is 60 cm and the estimated speed is 1.4 cm/s. The ice thickness measured across the outflow passage on Marsh Lake on two occasions eight days apart is shown in Figure 25. If the ice thickness is H and the thermal conductivity of ice K_i is 2.3 J/°C/m, the steady heat conservation equation stating that the sensible heat flux supplied to the underside of the ice is conducted

through the ice to the snow cover may be written

$$L\rho_i \frac{dH}{dt} = - \frac{K_i T_{si}}{H} - C_s \rho C_p T_{w_1} U_{w_1} = 0$$

where L is the latent heat of fusion and T_{si} is the surface temperature of the ice assumed to be the observed Whitehorse air temperature average of -9.33°C over two weeks prior to March 1, 1985 (February 16–28).

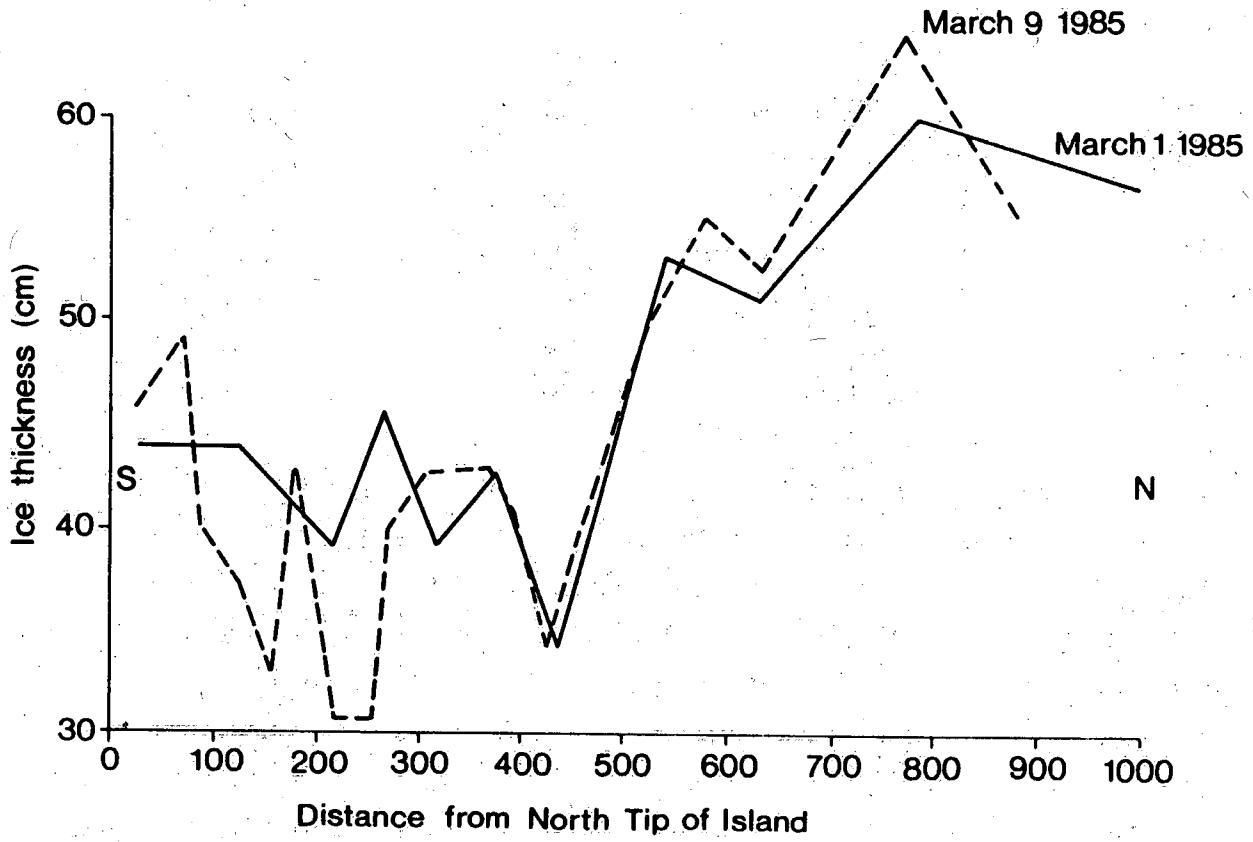

Figure 25. Ice thickness (cm) in the outflow region of Marsh Lake. Solid line, March 1, 1985; dashed line, March 9, 1985.

In this study, it is assumed that the snow cover was too thin (≈5 cm) and wind-compacted to substantially increase the temperature of the ice. The average ice thickness, the difference in ice thickness, the average air temperature on March 1, and the flow at 1 m on March 9, 1985, yielded a value of C_s of $0.63 \times 10^{-3} \pm 0.25 \times 10^{-3}$ based on 19 observation points across the outflow.

While this method is probably the most accurate of the four methods applied to this problem, it is subject nonetheless to large errors. As far as the field data are concerned, the error in ice thickness is probably at least 5 cm, the field temperatures were not measured on the same day as the current and ice thickness, and the currents themselves would have a large relative error in the threshold response region. Finally, another source of error is the model formulation. For example, the effect of radiation on the ice temperature has been ignored.

The final method of estimating C_s is similar to the second method, where the heat flux from the surface to the bottom is computed and equated to the surface heat flux. The difference is that, in addition, the lateral contribution to the heat balance is included. The horizontal heat flux along the axis of the lake is computed by summing the product of temperature and normal flow over the cross section. Returning to Figures 18 to 20, we find that the heat flux across line 2–7 is 7.36×10^5 kJ/s, that across line 14–12 it is 7.85×10^5 kJ/s, and across line 13–11 it is 7.63×10^5 kJ/s. The least squares best fit the line passing through line 14–12, and averaging the heat fluxes of the two down-lake lines yields an average rate of heat loss of 3.72×10^4 kJ/km. The heat flux through the ice surface over the lake surface area (assuming an average width of 1.9 km and based on the assumption of an average speed at 1 m of 1 cm/s and average temperature of 0.8°C) is equated to this average heat loss. The sensible heat transport coefficient is then $(0.58 \pm 0.3) \times 10^{-3}$. It is noted that the heat flux through line 1–8 is calculated ignoring stations 1 and 8 in order to correspond more closely with the sampling distribution on lines 14–12 and 13–11. It is evident in Table 1 that the computed heat flux across the shallow line 13–11 is larger than that of the centreline. The large error in this calculation arises from the fact that the lines are so close together and hence it is necessary to subtract two large numbers from one another. Unfortunately, due to unsafe ice conditions farther from the outflow, it was not possible to measure the cross-sectional heat transport farther from the outflow, which would provide a larger difference between heat transports.

Table 1. Cross-sectionally Averaged Quantities, Tagish Lake

Line station	Cross-sectional area (m^2)	Discharge (m^3/s)	Heat flux (kJ/s)	$\bar{U}_{1.0}$* (cm/s)
14-12	2.81×10^4	137	7.85×10^5	1.05
7-2	2.24×10^4	140	7.36×10^5	1.08
13-11	1.43×10^4	136	7.63×10^5	1.2

* Breadth-averaged current at depth of 1 m.

Discussion

In summary, three of the four independent methods used to calculate the sensible heat transfer coefficient are consistent with one another and result in an overall average value of $(0.8 \pm 0.3) \times 10^{-3}$. A fourth method dependent on an assumed parabolic distribution of flow for the heat flux computation yields a much larger value of C_s and therefore is not included in the average. It is noteworthy that the average sensible heat transfer coefficient determined in this study is less than the neutrally stable atmospheric boundary layer value of 1.45×10^{-3} and that it is within the uncertainty of the laboratory measurements of Gilpin et al. (1980).

Since the completion of the field study, two recent field investigations have come to light on the transfer of heat between seawater and ice. In their field investigation, Bogorodskiy and Sukhorukov (1983) determined a value of C_s of 1.3×10^{-3} from sea ice melting rates, as did Josberger and Meldrum (1985), who stated a value of 0.8×10^{-3} measured at a depth of 2.55 m below the ice. Their value could be too low because they ignored the heat flux through the 1-m-thick ice sheet, which could lead to a 16% error in half of their experiment. It is interesting that they obtained larger values of C_s during the second half of their experiment when the neglect of heat flux in the ice would be only an error of several percent. For this reason the value in the second part of the experiment is taken as 1×10^{-3} in place of the

0.8×10^{-3}. Unfortunately Josberger and Meldrum do not provide estimates of the roughness height so that the two estimates cannot be compared at a common height. However, if a typical value of a sea ice roughness of 0.001 m (Langleben, 1982) is assumed, then their value of C_s of 1×10^{-3} becomes 1.3×10^{-3} at a depth of 1 m according to the logarithmic boundary layer theory. Unfortunately, Bogorodskiy and Sukhorukov did not publish the depth at which their measurements were taken so that it is impossible to compare results. It does appear, however, that the lake ice transfer rates of sensible heat between water and ice are somewhat lower than in sea ice.

It is difficult to estimate the error of the determination in the present study. It would be safe to assume that the error bounds associated with the ice thickness measurements would apply. It is concluded as well that the three methods are not sufficiently accurate to allow the effect of boundary layer stability to be determined.

Application

It is assumed in the application of the sensible heat transfer formula that the flow at 1 m is fully turbulent. This would likely be valid for flows as low as 1 mm/s in the absence of stratification.

Due to the failure of the temperature profiler near the outflow, it is impossible to estimate the distribution of heat flux from the water to the ice in detail. In general, in Figure 26 there is a trend towards larger heat fluxes near the outflow and on the western side of the lake. This pattern corresponds closely to the ice thickness distribution shown for the Tagish outflow region in Figure 22. Similarly, in the Marsh Lake outflow section in Figure 24, an estimated heat flux at the outflow line of 157 W/m^2 corresponds to an ice thickness of 45 cm, whereas farther from the outflow at station 16, an estimated heat flux of 65 W/m^2 is associated with ice thickness of 60 cm.

The relatively high heat fluxes in the region of station N4 in Tagish Lake do not agree with the general pattern of ice thickness and

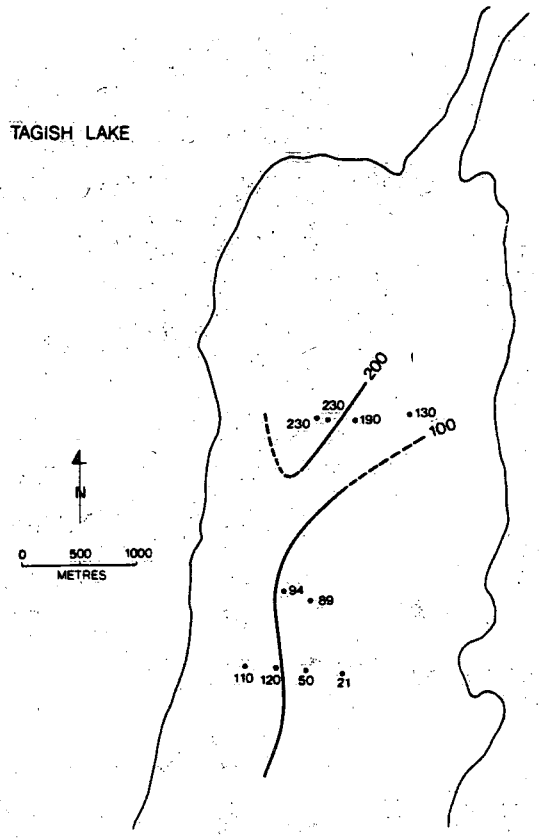

Figure 26. Heat flux distribution, Tagish Lake (W/m^2).

heat flux elsewhere. It is conjectured that the measured current is transient in nature caused by the wind stress divergence in the open water nearby associated with the observed storm conditions. Continued high heat fluxes in this shelf region of the outflow would lead to rapid thinning of the ice. The results of this section have been summarized by Hamblin and Carmack (1990).

Outflow Description

The previous section on transfer of heat between water and lake ice has dealt with one aspect of polynya formation and maintenance, the upward flux of heat from the water to the ice in a turbulent boundary layer responsible for thinning the ice. The other determining process is the upwelling of heat by advection of the outflow. Figures 12, 13, 17, 18, 19, and 21 show that the outflow is highly concentrated and three-dimensional in nature. If a one-dimensional simulation model is to be developed capable of treating outflow polynyas, then the upwelling will have to be parameterized in some way in the model.

The concentration of flow at the outlet itself, seen in Figures 12 and 21, at the deepest portion of the outflow cross sections suggests that friction may be the cause. To test this hypothesis, we may assume that the outflow acts as a broad river of irregular cross section of line N1 to N16 in Tagish Lake (Fig. 27), which may be divided into a left-hand main channel and a shallow right-hand berm. The customary assumption is that the same overall surface pressure gradient applies to each subsection (Henderson, 1966). According to Henderson, the ratio of average velocities in each section is proportional to the two-thirds power of the ratio of the half depths (area divided by the wetted perimeter). Allowing for 60% of the total flow of 140 m^3/s through the section of Figure 27 yields an average conveyance channel velocity of 4.8 cm/s and a right-side channel velocity of 2.9 cm/s. Since the right berm value on the average is about the level of the threshold of the current meter, it would be expected that the current meter would at least register some flow in the shallow section. It is concluded from this simple analysis that while friction is important in channelling the flow through the main channel there must be other factors at work too in accounting for the disproportionate flow conveyed through the main channel.

The question of outflow dynamics and others sparked by the field observations in this section on outflow description and Part I will be explored by mathematical modelling and by analytical methods in Part III. As well, background information on empirical methods of supplying surface energy components and river water temperatures will be examined in support of thermodynamic modelling of ice-free and ice-covered lakes.

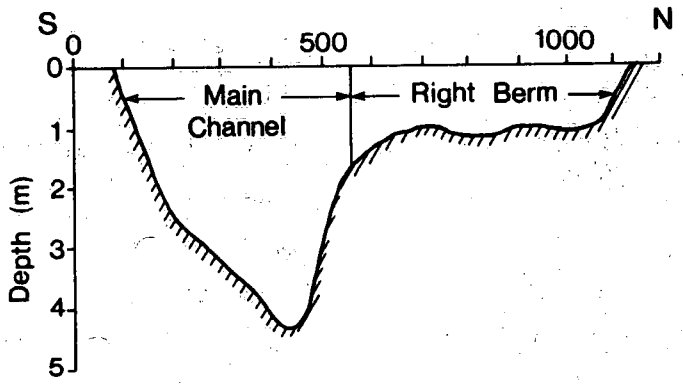

Figure 27. Outflow cross section of line N1 to N10, Tagish Lake.

PART III: THE PHYSICS AND NUMERICAL MODELS OF CIRCULATION AND THERMAL REGIMES IN LAKES AND RIVERS

Introduction

The physics of the ice-covered or winter through-flow in lakes is a well-defined problem in rotating stratified hydraulics that has received scant attention in the literature. Stigebrandt (1978) was the first to identify the essential nature of winter through-flow in lakes, that is, a flow field composed of an entrance jet, a steady near-surface flow from one end of the lake to the other, and a withdrawal area, as outlined schematically in Figure 28. Carmack et al. (1987) also provide a less-detailed picture of winter through-flow in Lake Laberge. The data discussed in Parts I and II and additional data presented in Carmack et al. (1987) are highly suggestive that three zones of flow, entrance, internal circulation, and outflow, are not independent, but interact with one another. This possibility was not recognized by Stigebrandt, who treated each regime separately. Unlike the ice-free period, where

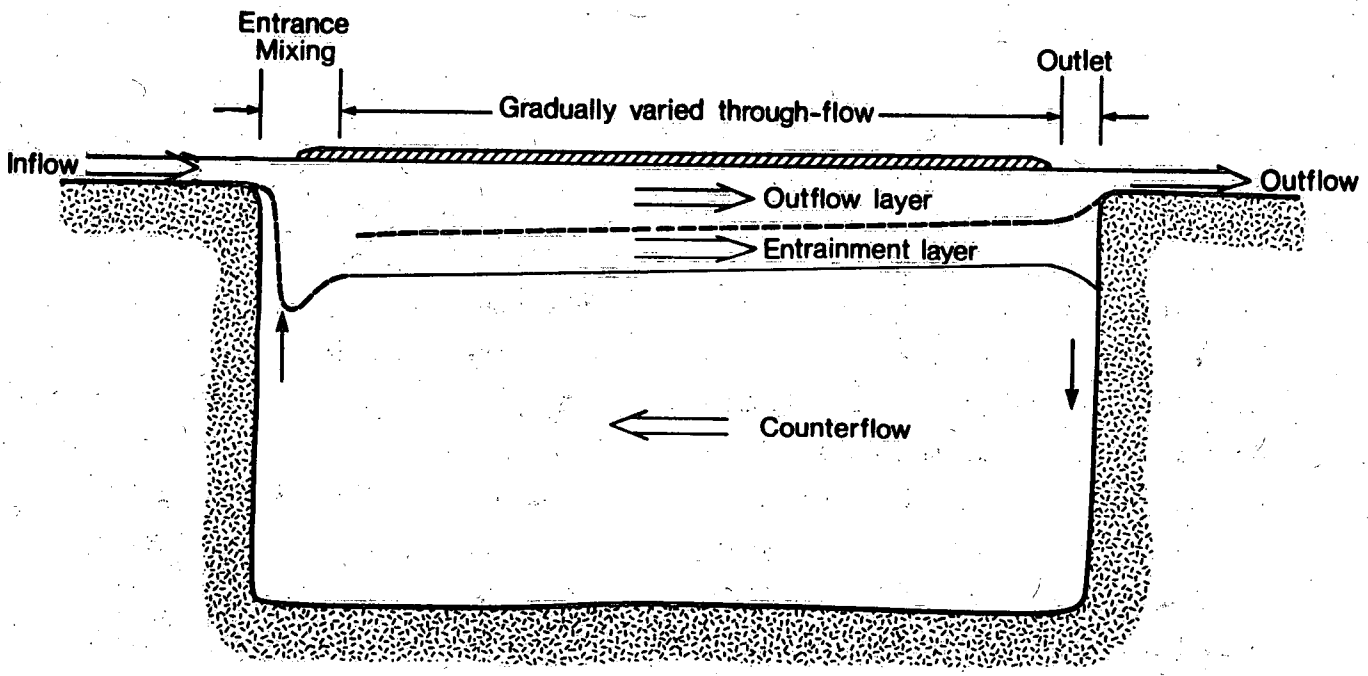

Figure 28. Schematic of winter through-flow.

turbulent mixing driven by atmospheric forcing largely determines the density structure of the lake, the outflow and inflow are connected by means of the through-flow. The closely related problem of selective withdrawal has been studied in containers in which the surface is drawn down. Thus, while it does not directly apply here, this theory does provide a useful preliminary guide.

Briefly, most of the mixing between the inflow and lake occurs close to the inflow in the zone shown as entrance mixing in Figure 28. The augmented flow, consisting of the original inflow plus the fluid entrained from the lake water, proceeds from the entrance mixing zone to the outflow region, where the outflow portion is drawn up to supply the outflow and the entrainment layer is turned around to become the counterflow. The interfacial boundaries of the through-flow are noticeably inclined along the axis of the lake in order to overcome frictional resistance in accordance with the theory of gradually varied internal flow, except at the outflow where downwelling is evident and at the entrance where the data and analyses to follow indicate the presence of an internal hydraulic jump. Although the three flow regimes (namely, inflow, through-flow, and outflow) are coupled, each will be discussed separately.

Outflow Dynamics

The simplest method of modelling the upwelling of the outflow would be to assume that at least the core flow is potential flow. The well-known potential solution for flow into the corner of a wedge has streamlines intermediate in slope between the confining walls. For example, in the case of the Tagish Lake outflow of Figures 18 to 20, the bottom slope is approximately 7×10^{-3} so that the 2°C isotherm, in the absence of mixing, ought to have a slope of 4.5×10^{-3} and the 1.5°C isotherm, a slope of 2×10^{-3} according to potential flow theory. Since the observed slopes are 1.5×10^{-3} and 8×10^{-4}, respectively, about one-third of the expected value, there must be some selective withdrawal of the outflow by the stratification of the fluid near the outflow. A

similar analysis for the Marsh Lake outflow between stations 15 and 16 shows that the observed slope of 1°C isotherm is about one half of that expected by potential theory. In this case, this observation is in agreement with the expectation that the influence of vertical density stratification would be weaker so close to the outflow.

In order to model the outflow polynya, it is necessary to mathematically describe the heat flux associated with the outflow and temperature distribution under the ice. As a first step, it is instructive to find out if the outflow is dominated by either viscous-diffusive effects or by inertial effects. From the two-dimensional outflow theory described by Fischer et al. (1979), we may compute an outflow Froude number, $Fr = q/NL^2$, and a Grashof number, $Gr = N^2L^4/k_v^2$, where L is the length of the lake; in the case of Marsh Lake, 28 km. Taking a value for N^2 of 6.8×10^{-5} s^{-2} for Marsh Lake, a vertical eddy diffusivity for heat, k_v, of 10^{-4} m^2/s and a discharge per unit width, q, of 168/500 = 0.168 m^2/s, it follows that $Fr = 5.2 \times 10^{-8}$ and $Gr = 4.1 \times 10^{21}$. Since the product $FrGr^{1/3}$ is 0.82, the outflow may be classified as intermediate between viscous-diffusive and inertial. (As the ice sheet is a plane of symmetry, the discharge is taken as twice the outflow of 84 m^3/s.) On the other hand, if the outflow is considered as three-dimensional, Lawrence (1980) has obtained the transition parameter $Q/(Lk_v)$, which is much larger than unity, suggesting inertial dominance of the selective withdrawal. In Tagish Lake, the outflow is similar because the much greater length of the lake compensates for the greater discharge of 140 m^3/s. In this case, the depth of the withdrawal layer, D (outflow layer thickness), may be given by $D = 5.5\ Gr^{-1/6}\ L$ or 38.5 m and from three-dimensional theory by $(Q/N)^{1/3}$ or 32 m.

A theory of stratified withdrawal dominated by viscosity and diffusivity in a steady two-dimensional outflow has been given by Koh (1966). In his solution, Koh did not consider the under-ice flow problem so that a number of important effects were excluded, namely, the nonlinear dependence of density on temperature, the zero flow condition at the ice water boundary, and the flux of heat being proportional to the

product of velocity and temperature at 1 m depth. Nonetheless, it is still possible to determine the general nature of the heat flux from Koh's similarity method. To a first approximation close to the ice, U is proportional to $y/x^{2/3}$ and T varies as $y^4/x^{5/3}$ so that the vertical heat flux depends on $y^5/x^{7/3}$ where y is the vertical coordinate with the origin at the ice/water boundary and x is the horizontal distance from the outflow. At a fixed depth, then, the heat flux is proportional to $x^{-7/3}$, which appears to be a much too rapid fall-off with horizontal distance. Physically, the vertical diffusion term diffuses away the sharpened vertical temperature gradient caused by vertical upwelling into the sink and thus temperature field is not changed until the immediate vicinity of the outflow is reached where vertical advection dominates the balance. Alternatively, a low Prandtl number model is advanced in which vertical diffusion of temperature is ignored in favour of pure advection. In the case of advection in a two-dimensional flow, it is well known that the isotherms must be parallel to the flow lines so that the temperature field is a function of stream function. The requirement of nonlinear density may be accounted for in the similarity equation. With these simplifying manipulations, it is also possible to seek similarity solutions for the horizontal vorticity equation. In this case, the similarity variable, Z, is $y/[\nu qx/g\beta(\Delta T)^2]^{1/4}$ where ν is the eddy viscosity assumed to be $10^{-5}m^2/s$, β is $6.8 \times 10^{-6}/C^2$, ΔT is the temperature difference across the outflow, and g the acceleration of gravity. As in the case of Koh's model, it is assumed that the first derivative of the similarity function, which is proportional to horizontal velocity, varies as the similarity variable. This is necessary since the velocity must go to zero at the ice/water surface. Thus the discussion is confined to the region below the ice where the outflow-induced current is decreasing upwards. This assumption is valid since, with the parameters specified, the range of interest of Z is from 0.2 to 1. In this region, the form of the temperature distribution ought to behave as

$$T = \frac{Z^2 T_D}{2}$$

where T_D is temperature at the depth, D, and

$$U = \frac{qZ}{\left[\frac{qvx}{B(\Delta T)^2 g}\right]^{1/4}}$$

In the above expressions, the numerical constant of unity has been determined approximately by reference to the field data of Marsh and Tagish lakes rather than by solving the similarity equations directly. Finally, we may infer that the heat flux from the water to the ice may be given according to equation (1) by

$$H = \frac{C_s}{2} \rho C_p g y^3 \beta (\Delta T)^3/(xv) \qquad (2)$$

where y is, of course, taken at depth of 1 m. It is noted that the discharge per unit width, q, does not explicitly appear in this expression, which is probably due to simple linear dependence assumed for the behaviour of the similarity function and the limitations of similarity. As an example of the application of this formula, consider the case of Tagish Lake where T_D is 2.5°C at depth, D, of 1 m at a distance of 3 km from the outflow, the heat flux is 10 W/m^2 at a distance of 300 m, 100 W/m^2 at 30 m, and 1000 W/m^2 at 3 m. This 30-m flux indicates that the polynya should be at least 30 m in length as this heat flux is much larger than the heat flux through a 10-cm layer of ice of 345 W/m^2 at an average air temperature of -15°C. This figure of 345 W/m^2 may be compared to the March mean heat loss of an arctic polynya of 329 W/m^2 (Den Hartog et al., 1983) or 380 W/m^2 for sensible and evaporative heat fluxes over the St. Lawrence Island polynya (Pease, 1985).

In the case of Marsh Lake, the value of the appropriate stratification parameter is somewhat ambiguous as the average value of N may not apply in a two-layer situation. An application of the

two-dimensional theory of Fischer et al. (1979, equation 6.87) suggests that withdrawal depth, D, may occur in the epilimnion to a depth of 11.6 m.

$$D = \left[\frac{2q}{\left(\frac{\Delta\rho g}{\rho} \right)^{1/2}} \right]^{2/3} \tag{3}$$

where $\Delta\rho$ is the density difference between the top and bottom of the epilimnion. Thus, if we take the temperature at the base of the epilimnion of 1.5°C as the ΔT in equation (2), it follows that the heat flux at 3 km from the outlet is 2.4 W/m^2, 24 W/m^2 at 300 m, and 240 W/m^2 at 30 m from the outflow. Since this last value is less than the heat flux required to melt an ice layer of 10 cm in thickness, it is likely that the polynya does not exist when air temperatures are as cold as -15°C on average.

It has been stated earlier that the viscous theory is indicated according to the value of the parameter R of Fischer et al. (1979), but that diffusive effects on the temperature field are not realistic. In the application of equation (2), it is recommended that the withdrawal depth at which temperature ΔT is determined be computed either from equation (2) in a two-layer situation or by

$$D = 2\sqrt{q/N} \tag{4}$$

in the case of uniform stratification after the inertial theory of Fischer et al. (1979). Equation (4) applied to Tagish Lake results in a value of D of 120 m, or in other words the bottom depth. It may be noted that by use of inertial withdrawal formulae, the discharge enters the heat flux expression (2) through the depth at which the temperature ΔT is determined.

This analysis of outflow dynamics is concluded by the recommendation that equation (2) along with the companion formulae (3) and (4) be tested by application to the formation of the polynya of Lake Laberge employing the simulated temperature profiles of the model DYRESM (Patterson and Hamblin, 1988). Typical observed polynya areas have been determined from satellite and aerial photographs by Carmack et al. (1987) for the headwater lakes. If this simple approach fails, then it is possible that the low Prandtl number similarity equation (Koh, 1966)

$$Z \frac{\left(f - \frac{4}{\Delta T}\right) f^{i}}{2} = f^{iv}$$

with the conditions $f(0) = f^{i}(0) = f^{ii}(\infty) = 0$ and $f(\infty) = 1$ be solved for the velocity and temperature field numerically. It may be noted that similarity does not allow for a realistic surface boundary condition for temperature, and as a result does not permit an exchange of heat to the ice. A more exact treatment would require a full two-dimensional solution, which is beyond the scope of a one-dimensional thermal simulation model. The obvious shortcoming of formula (2) is the difficulty in specifying ΔT. Equations (3) and (4) may provide only approximations. Also, it is noted that the depth is much greater than the discharge depth in the development of the theory.

In some cases in the development of the theory, it has been assumed that the outflow is two-dimensional in nature. This idealization could only hold in long, narrow lakes such as Marsh, Tagish, and Laberge. However, the outflow of Atlin Lake and others is at a mid-axis point, where clearly the outflow would be better idealized by axisymmetric withdrawal theory. Examination of the axisymmetric equations revealed that a similarity does not exist, but that a solution of the form $F(Y)/r$ exists for a limited range of r yielding a heat flux dependence on radial distance, r, proportional to $\Delta TQ^2/r^3$ where Q is the discharge (Koh, 1966). Therefore, the radial dependence of heat flux falls off much more rapidly with horizontal distance, r, from the outlet. This dependence on

the radius and its effect on polynya area ought to be testable from aerial and satellite observations of the polynya area of Atlin Lake when combined with lake survey and meteorological data. The withdrawal depth may be given by the formula of Lawrence (1980), $(Q/N)^{1/3}$.

Three-Dimensional Effects

The outflow dynamics so far discussed either assume horizontal homogeneity across the lake or axial symmetry, thus ruling out such three-dimensional effects as the earth's rotation. These effects will be explored here by means of a vertically integrated approach, but first we return to the simple two-dimensional case discussed in the previous section on outflow dynamics.

A three-dimensional coordinate system, Figure 29, has its origin at the surface, the x-axis directed along the channel in the direction of flow, the y-axis transverse to the flow and increasing leftwards of the flow, and the z-axis is taken positive upward from the ice/water surface.

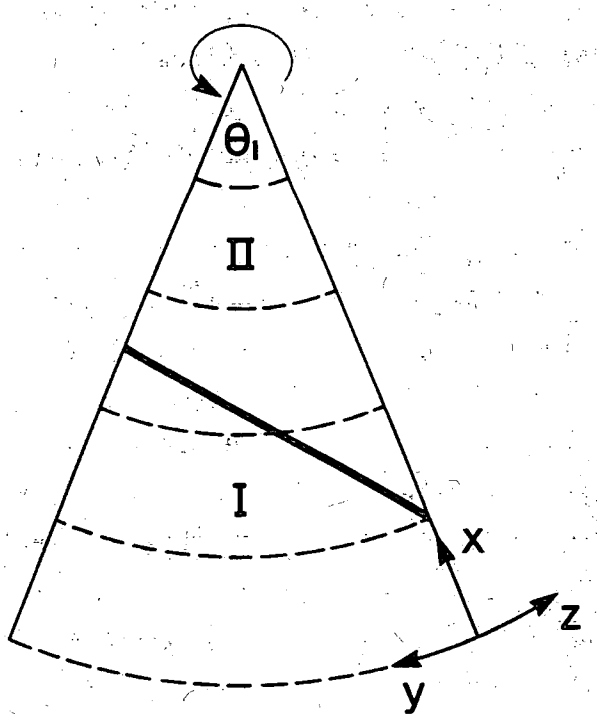

Figure 29. Idealized flow into a rotating sector.

At a large distance from the outflow, the stratification and hence density defect, ρ, is taken as $\rho = (\rho_s - \rho_D)(z + D)/\rho_D D$, where D is the previously defined withdrawal depth (outflow layer depth, Figure 28). The density defect is zero at $z = -D$ and decreases to a minimum at the surface (ρ_s). The steady equation of motion, assuming lateral uniformity and that h is the depth of zero velocity, is

$$\frac{\partial u^2}{\partial x} + \frac{\partial (uw)}{\partial z} = \frac{1}{-\rho_0} \frac{\partial P}{\partial x} - g \int_{-h}^{z} \frac{\partial \rho}{\partial x} dz + \frac{1}{\rho_D} \frac{\partial \tau xz}{\partial z} \qquad (5a)$$

Although not exact, it is assumed for simplicity that at the withdrawal depth and lower, the outflow velocity and horizontal gradient of total pressure vanish and ρ is zero so that the gradient of barotropic pressure, P, may be evaluated from $\rho = \varepsilon(z + h)/h$ as

$$\frac{1}{\rho_D} \frac{\partial P}{\partial x} = - g \int_{-h}^{0} \frac{\partial \rho}{\partial x} dz = g \frac{\varepsilon}{2} \frac{\partial h}{\partial x} \qquad (5b)$$

where $\varepsilon = (\rho_D - \rho_s)/\rho_D$ and h may now be less than the far field withdrawal depth, D.

From vertical integration of equation (5a) and parameterization of the under-ice stress by the transport, q, and eddy viscosity, ν, for a parabolic boundary layer and the assumption that u also varies linearly with depth outside a thin boundary layer [$u = 2q(h+z)/h^2$], we have

$$-4q^2 \int_{-h}^{0} \frac{\partial (h + z)^2}{\partial x\, h^4} dz = - g\varepsilon \frac{h}{2} \frac{\partial h}{\partial x} - g\varepsilon \int_{-h}^{0} \frac{\partial}{\partial x} \left(\frac{1}{h} \frac{z^2}{2} - zh \right) dz + \frac{2.0\nu q}{h^2}$$

It may be noted that in stratified withdrawal theory cosine variation of the velocity is usually assumed instead of the linear variation assumed here. Interchanging the order of differentiation and integration yields

$$-4q^2 \frac{\partial}{\partial x} \int_{-h}^{0} \frac{(h + z)}{h^4} dz = - g\varepsilon \frac{h}{2} \frac{\partial h}{\partial x} - g\varepsilon \frac{\partial}{\partial x} \int_{-h}^{0} \frac{1}{h} \left(\frac{z^2}{2} - zh\right) dz$$

$$\left[- \frac{\varepsilon g}{h} \left(zh - \frac{z^2}{2}\right)\right]_{z = -h} \frac{\partial h}{\partial x} + \frac{2.0\nu q}{h^2}$$

After integration and collection of terms

$$\left(\frac{h^3}{3} - \frac{4q^2}{3g\varepsilon}\right) \frac{\partial h}{\partial x} = \frac{2 \nu q}{g\varepsilon} \qquad (6)$$

or $$h^4 - h_0^4 - \frac{16q^2}{g\varepsilon} (h - h_0) = \frac{24\nu qx}{g\varepsilon}$$

where the depth at the outflow, h_0, is assumed to occur when the slope of the outflowing layer is infinite or $h_0 = (4q^2/g\varepsilon)^{1/3}$. Since the analytical solution for h is implicit, it must be computed by numerical methods, although the layer depth may be approximated reasonably by $(24\ \nu qx/g\varepsilon + h_0^4)^{1/4}$ under most conditions. The solution, h, appropriate to Lake Laberge, is evaluated in Figure 30 for $\nu = 10^{-5}$ m^2/s, $q = 0.046$ m^2/s, and $\varepsilon = 10^{-5}$, and apparently remains thin for large distances from the outflow. In the discussion of the two- and three-dimensional selective withdrawal theory above, the transition between frictionally and inertially dominated flows was computed. Similarly, by equating the frictional to inertial terms in equation (6), the transition distance is estimated to be $4/3\ 2^{1/3}\ q^{5/3}/[\nu\ (g\varepsilon)^{1/3}]$. In the case of the parameters for the Lake Laberge outflow, this expression gives a transition distance of 2.1 km from the outflow. Between this point and the inflow, the outflow layer is seen to thicken by about 4 m from Figure 8 and from Appendix E in Carmack et al. (1987) and to have an average depth of approximately 8 m. It is now possible to compute the eddy viscosity from the longitudinal slope of the isotherms according to

$$v = \frac{g\varepsilon}{2q} \frac{H^3}{3} \frac{dh}{dx}$$

which yields a value of 1.5×10^{-5} m^2/s. It may be noted that equation (6) is of identical form to the gradually varied flow equation (10) of Baddour (1987) in the case of a deep counterflow. The solution to equation (6) thus provides the linkage between the outlet region of the length of the transition point and the interior through-flow, which is an example of gradually varied internal flow. The counterflow cannot be taken into account in the simple analysis of the through-flow problem unless the exchange between the entrainment layer and return flow is known. This problem will be discussed in the section on two-dimensional through-flow modelling. Based on the assumed temperature profile in the outflow layer (see Fig. 8), $T = -0.9\ z/h + 0.3$, it is possible to compute the vertical and horizontal components of the advection of temperature at

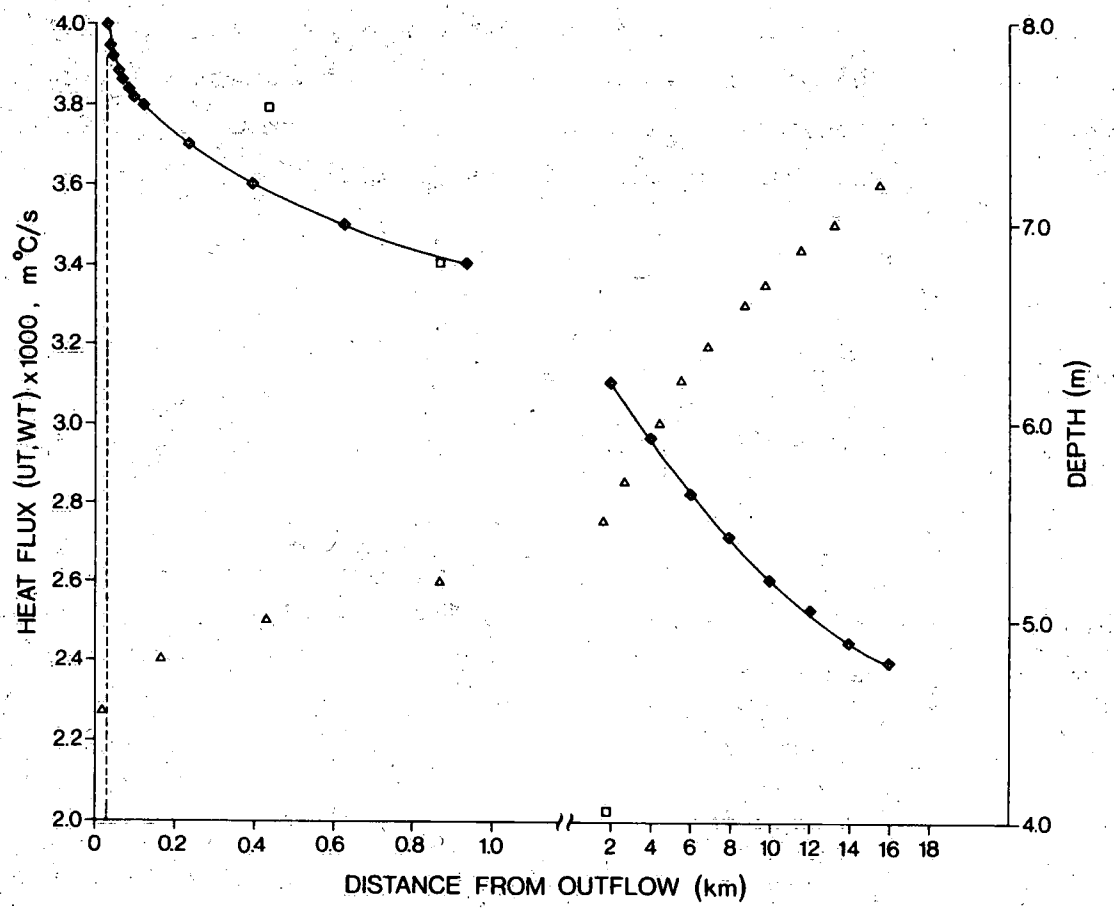

Figure 30. Depth of outflowing layer, Δ, with distance from outflow. Solid line is horizontal temperature flux at depth of 1 m. Dashed line is vertical flux. Open squares are numerically obtained uT'.

a depth of 1 m. These components are proportional to the vertical and horizontal heat flux. It is seen in Figure 30 that, except for a narrow region within 50 m of the outflow, nearly all the heat supplied to the ice is through horizontal flow as opposed to vertical flow.

It is evident, then, that the vertically integrated outflow and through-flow model has the same $x^{1/4}$ dependence for isopycnal depth as the continuous two-dimensional model at large distances from the outflow.

The product of velocity and temperature will then be proportional to h^{-2} or $x^{-1/2}$, which is a weaker dependence than the continuous model.

The extension of the vertically integrated model to three-dimensional outflow requires a further assumption on the under-ice friction. It is assumed that the friction acts only on the longitudinal component of flow and that it may be given by the surface velocity times a linear friction coefficient, γ, having dimensions of velocity. For simplicity, advection terms are ignored. The three-dimensional equations may be written with these simplifying assumptions as

$$-fv = \frac{1}{\rho_D}\frac{\partial P}{\partial x} - g\int_z^0 \frac{\partial \rho}{\partial x}\,dz + \frac{1}{\rho_0}\frac{\partial \tau xz}{\partial z} \tag{7}$$

$$fu = \frac{1}{\rho_D}\frac{\partial P}{\partial y} - g\int_z^0 \frac{\partial p}{\partial y}\,dz \tag{8}$$

and in integrated form employing the above analysis of the barotropic pressure gradient (cf. equation [5b]) and the component u at the surface from the previous equation

$$f\frac{\partial \psi}{\partial y} = -\frac{g\varepsilon h}{3}\frac{\partial h}{\partial y} \tag{9}$$

$$f\frac{\partial \psi}{\partial x} = -\frac{g\varepsilon h}{3}\frac{\partial h}{\partial x} - \frac{\gamma}{f}\frac{g\varepsilon}{2}\frac{\partial h}{\partial y} \tag{10}$$

where f is the Coriolis paramater.

The vertically integrated stream function has been introduced such that

$$U = \frac{\partial \psi}{\partial y}, \quad V = -\frac{\partial \psi}{\partial x}$$

where $U = \int_{-h}^{0} u\,dz$ and similarly for V or in terms of polar coordinates, equations (9) and (10) become

$$f \frac{\partial \psi}{\partial \theta} = -\frac{g\varepsilon}{6} \frac{\partial (h^2)}{\partial \theta} \tag{11}$$

$$f \frac{\partial \psi}{\partial r} = -\frac{g\varepsilon}{6} \frac{\partial (h^2)}{\partial r} - \frac{\gamma}{f} \frac{g\varepsilon}{2r} \frac{\partial h}{\partial \theta} \tag{12}$$

$$Ur = \frac{1}{r} \frac{\partial \psi}{\partial \theta} \; ; \quad U_\theta = -\frac{\partial \psi}{\partial r}$$

Integration of equation (11) across a pie-shaped channel, (Fig. 29) from $\theta = 0$ to θ yields in terms of the bulk outflow, Q,

$$fQ = -\frac{g\varepsilon}{6} (h_1^2 - h_0^2) \tag{13}$$

In the case when $h_0 < \sqrt{6fQ/(g\varepsilon)}$, as is probably the case here, equation (13) implies that the withdrawal layer does not extend across the channel. It is evident that the layer depth on the right-hand side of the channel in the direction of flow is greater than on the left side. Now along the sides of the channel, $\partial\psi/\partial r = 0$ so that equation (12) becomes

$$\frac{\partial (h^2)}{\partial r} = -\frac{3\gamma}{fr} \frac{\partial h}{\partial \theta} \tag{14}$$

From the requirement of continuity, equations (11) and (12) give $\partial^2 h/\partial \theta^2 = 0$, which implies $\partial h/\partial \theta$ is a function of r say $\alpha(r)$, which from equation (13)

$$\alpha = -\frac{h_0}{\theta_1}\left(1 - \sqrt{1-6fQ/h_0^2\, g\varepsilon}\right)$$

or to an approximation if $6fQ < (h_0^2\, g\varepsilon)$

$$\alpha \simeq -\frac{3fQ}{g\varepsilon\, h_0\theta_1}$$

In the approximate case we can now integrate equation (14) along the right-hand boundary

$$h_0^3 - D^3 = \frac{27\gamma\, Q \ln (r/r_D)}{g\varepsilon\, \theta_1}$$

where D is the specified depth of the outflow layer at some distance from the sink, r_D, and h_1 can be found from equation (13). In the case that the withdrawal layer fills the channel, but $h_0 \sim \sqrt{6fQ/(g\varepsilon)}$, equation (14) must be integrated numerically.

We notice the following features of this solution: the transverse velocity is zero throughout the section; the longitudinal transport is uniform across the channel; the depth varies linearly so that the flow speed must be larger on the left-hand side to compensate; and the larger the angle θ_1 of the sector, the smaller the radius r_D is. At least in the case of low outflow or weak stratification [$h_0 > \sqrt{6fQ/(g\varepsilon)}$], rotation does not affect the outflow thickness. As far as outflows from the headwater lakes are concerned, the theory suggests that since the discharge is so large, the outflow may not extend across the lake. This is probably the case in Marsh Lake, where the left-hand current along the southwestern shoreline is in the counterflowing flowing direction in Figures 11 and 12. The cross-channel tilt is seen to increase towards the outlet.

Although the laboratory experiments of Monismith and Maxworthy (1988) were designed to examine the spin-up of stratified rotating outflow and drew down the upper layer, it is of some interest to compare their results with the above theory. They found that the outflow current was concentrated on the left-hand shoreline and decreased linearly to the opposite wall. In case of small cross-channel tilts, the current also decreases linearly from left to right. This decrease of current horizontally implies, through the thermal wind relation, that the isopycnal surfaces in the withdrawal layer are not linear but curve upwards at the shoreline. The horizontal shear in the outflow thus could account for the concave shape of detailed temperature and conductivity transects in Appendix E of Carmack et al. (1987).

Because of the stronger flow on the left-hand side of the channel, as well as higher temperatures due to reduced withdrawal depth, the principal influence of the earth's rotation is to cause larger sensible heat transfers on the left-hand side of the outflow region, which is in agreement with the heat flux and ice thickness distributions (Figs. 22 and 26). Furthermore, since the depth of the withdrawal layer is greater on the right-hand side of the channel, it might intersect the bottom on this side farther from the sink than on the other side if the bottom shoals more rapidly than h. Figure 29 shows a hypothetical case of the interaction of the withdrawal depth and bottom in a pie-shaped region with a linear sloping bottom. The region where the depth is greater than the withdrawal depth is region I. The assumptions so far made will not be valid in region II, where the depth is less than the withdrawal depth. There will no longer be compensation of the barotropic pressure gradient by the baroclinic gradient. Bottom friction caused by the resulting bottom current will have to be taken into account. The interaction of bathymetry, rotation, and baroclinicity has been termed the JEBAR effect (joint effect of baroclinicity and bottom relief) (Csanady, 1985; Rattray, 1982). Since the solutions are not valid in region II, where inertial effects ought to predominate, the neglect of these terms in equations (7) and (8) is justified.

It is not clear that the simple diagnostic treatment of the JEBAR effect can be employed, as the density defect is unknown in region II. However, the bottom frictional effect on the right-hand side of the channel would tend to retard the flow further and tend to concentrate the discharge even more to the left-hand side. In the realistic case of a transverse bottom slope as well, the JEBAR effect will exert torques on the fluid at the shorelines, pushing it to the middle of the channel. This may explain why friction alone is not sufficient to account for the low flow in the shallow lateral portions of the lake as discussed above.

Through-Flow

Three-Dimensional Diagnostic Model of Through-Flow Under Ice With Friction

In the previous computations of the heat flux across a lake section, the thermal wind relation was combined with the drogue data at one depth in the water column to compute the flow field. These computations were compared with the known cross-sectional transport for consistency. It would be desirable to be able to infer the flow field without recourse to drogue or current meter observations from the temperature observations and the known constraint of volume transport through each cross-section. In this section, a diagnostic method is outlined for inferring the three-dimensional steady circulation from the density field and through-flow. This method is subsequently applied to Tagish Lake and the inferred currents compared to the field observations.

The equations of motion for this problem are identical to equations (7) and (8), but now the internal shear stress is represented by the more accurate Ekman dynamics. As the Ekman solutions for the case of surface ice cover do not appear to given in the literature, they are included for convenience in Appendix B.

Since the vertical eddy viscosity is likely to be order 10^{-4} m^2/s or less under the ice cover, the corresponding Ekman boundary

layer thickness, $\sqrt{2\nu/f} = 1/\alpha$, is much less than the water depth so that surface stresses, τ_{sx} and τ_{sy}, may be given the following approximate expressions (see Appendix B):

$$\tau_{sx} = \frac{\rho}{2\alpha}\left(\frac{\partial P}{\partial x} + \frac{\partial P}{\partial y}\right)_{z=0}$$

$$\tau_{sy} = \frac{\rho}{2\alpha}\left(\frac{\partial P}{\partial x} - \frac{\partial P}{\partial y}\right)_{z=0}$$

and similarly for the bottom stress as τ_{bx} and τ_{by} at depth $z = -H$

$$\tau_{bx} = -\frac{\rho}{2\alpha}\left(\frac{\partial P}{\partial x} + \frac{\partial P}{\partial y}\right)_{z=-H}$$

$$\tau_{by} = -\frac{\rho}{2\alpha}\left(\frac{\partial P}{\partial y} - \frac{\partial P}{\partial x}\right)_{z=-H}$$

where P is the total pressure, $P = g(\eta\rho_0 + \int_{-H}^{0} \rho dz)$ and η is the free surface elevation.

Equations (7) and (8) may be integrated vertically over the total depth, H, to yield

$$-fV = -gH\frac{\partial \eta}{\partial x} - H\int_{-H}^{0}\left(1 - \frac{z}{H}\right)\frac{\partial \rho}{\partial x}\,dz + \frac{g}{\alpha}\left(\frac{\partial \eta}{\partial x} + \frac{g\partial \eta}{\alpha \partial y}\right)$$

$$+ \frac{g}{\rho_0 2\alpha}\int_{-H}^{0}\left(\frac{\partial \rho}{\partial x} + \frac{\partial \rho}{\partial y}\right)dz$$

$$-fU = -gH\frac{\partial \eta}{\partial y} - H\int_{-H}^{0}\left(1 - \frac{z}{H}\right)\frac{\partial \rho}{\partial y}\,dz + \frac{g}{\alpha}\left(\frac{\partial \eta}{\partial y} - \frac{\partial \eta}{\partial x}\right)$$

$$+ \frac{g}{\rho_0 2\alpha}\int_{-H}^{0}\left(\frac{\partial \rho}{\partial y} - \frac{\partial \rho}{\partial x}\right)dz$$

where U and V are the vertically integrated components of the transport.

It may be noted that these equations are identical to the approximate form of the well-known homogeneous Ekman problem, which has been solved by Hamblin (1976) by means of the finite element method, plus two additional terms each involving the vertical integrals of the horizontal density gradients. These expressions may be substituted into the finite element form of the continuity equation as in Hamblin (1976),

$$\iint \left(\frac{\partial \phi}{\partial x} U + \frac{\partial \phi}{\partial y} V\right) dA = - \int \phi \, U_N \, ds$$

where ϕ is a weighting function and the term on the right-hand side is a line integral of the known boundary forcing by the transport, U_N, normal to the boundary. The unknown transports, U and V, may be eliminated by the above relations with the result that

$$\iint gH \left(E \frac{\partial \eta}{\partial x} - F \frac{\partial \eta}{\partial y}\right) \frac{\partial \phi}{\partial x} \, dxdy + \iint gH \left(F \frac{\partial \eta}{\partial x} + E \frac{\partial \eta}{\partial y}\right) \frac{\partial \phi}{\partial y} \, dxdy$$

$$= -\iint \frac{g}{\rho_0} \left\{ \frac{\partial \phi}{\partial x} \left[-H \int_{-H}^{0} \left(1 - \frac{z}{H}\right) \frac{\partial \rho}{\partial y} \, dz + \frac{g}{2\alpha} \int_{-H}^{0} \left(\frac{\partial \rho}{\partial y} - \frac{\partial \rho}{\partial x}\right) dz \right] \right.$$

$$\left. + \frac{\partial \phi}{\partial y} \left[H \int_{-H}^{0} \left(1 - \frac{z}{H}\right) \frac{\partial \rho}{\partial x} \, dz - \frac{g}{2\alpha} \int_{-H}^{0} \left(\frac{\partial \rho}{\partial x} + \frac{\partial \rho}{\partial y}\right) dz \right] \right\} dxdy$$

$$- f \int \phi \, U_N \, ds$$

where $E = - \frac{1}{\alpha H}$; $F = \left(1 - \frac{1}{\alpha H}\right)$

The unknown surface pressure field, η, may be determined in terms of the known forcing terms on the right-hand side of the above equation from field data for the density field and the inflows and outflows on the boundary. Once the surface pressure field has been found the pressure gradient at each finite element mesh point may be determined by solving the equations

$$\iint \phi_m \phi_n dA = \iint \phi_m \frac{\partial \eta_n}{\partial x} dA \tag{15}$$

$$\iint \phi_m \phi_1 dA = \iint \phi_m \frac{\partial \eta_1}{\partial y} dA \tag{16}$$

for ϕ_1. In equations (15) and (16), ϕ_m is taken to be a quadratic function, whereas ϕ_n is cubic in the application to follow.

Once the barotropic or free surface pressure gradients are known, equations (7) and (8) may be solved for the velocity distribution at a mesh point as a function of depth. The approximate solutions for the case of low vertical eddy viscosity ($H >> 1/\alpha$) are

$$u = \frac{g}{f}\frac{\partial n}{\partial y} - \frac{g}{f}\int_{-z}^{0} \frac{\partial \rho}{\partial y} dz + g\frac{e^{\alpha z}}{f} \cos(\alpha z) \frac{\partial \eta}{\partial y} - g\frac{e^{\alpha z}}{f} \sin(\alpha z)\frac{\partial \eta}{\partial x}$$

$$+ \frac{ge^{-\alpha(z+H)}}{f}\left\{\left(\frac{\partial \eta}{\partial y} + \int_{-H}^{0} \frac{\partial \rho}{\rho_o \partial y} dz\right) \cos[\alpha(z+H)]\right.$$

$$\left. - \left(\frac{\partial \eta}{\partial x} + \int_{-H}^{0} \frac{\partial \rho}{\rho_o \partial y} dz\right) \sin[\alpha(z+H)]\right\} \tag{17}$$

$$v = \frac{g}{f}\frac{\partial \eta}{\partial x} + \frac{g}{f}\int_{-z}^{0} \frac{\partial \rho}{\partial x} dz - g\frac{e^{\alpha z}}{f} \cos(\alpha z) \frac{\partial \eta}{\partial x} + g\frac{e^{\alpha z}}{f} \sin(\alpha z) \frac{\partial \eta}{\partial y}$$

$$- \frac{ge^{-\alpha(z+H)}}{f}\left\{\left(\frac{\partial \eta}{\partial x} + \int_{-H}^{0} \frac{\partial \rho}{\rho_o \partial x} dz\right) \cos[\alpha(z+H)]\right.$$

$$\left. + \left(\frac{\partial \eta}{\partial y} + \int_{-H}^{0} \frac{\partial \rho}{\rho_o \partial y} dz\right) \sin[\alpha(z+H)\right\} \tag{18}$$

It may be noted that, outside the boundary layer regions at the surface and bottom, the exponential terms in the above expressions are small and may be neglected if the depth is much greater than the boundary layer thickness.

Application of Three-Dimensional Model to Tagish Lake

A mesh of 24 triangles was drawn through the 20 field stations in Tagish Lake (Fig. 14) with the field stations forming the vertices of the triangles. This mesh was expanded to include the boundaries of the lake and two inflow and outflow points upstream and downstream from the field stations. In total, the expanded mesh comprised 52 triangles and 119 nodal points.

In order to determine the forcing due to the baroclinic component of the pressure field, it is necessary to first compute the horizontal density gradients. Equations similar to equations (15) and (16) may be solved to yield the horizontal density gradients at each of the interior nodes where density is defined, except that linear interpolation of the density field was used. Density gradients were computed at 2-m increments of depth starting at the surface. Vertical integrals of horizontal density were then evaluated according to the trapezoidal rule applied at discrete 2-m intervals. Density gradients were extrapolated from the interior to the boundary points by the simple assumption that they are equal to the nearest interior values.

Finally, inflow was imposed between two open lake points located on the boundary to the south of line 12-14 and the corresponding outflow of 140 m^3/s at two interior points to the north of line 11-13. The parameter values assumed throughout the study were 1 cm^2/s for the vertical eddy viscosity and 1.27×10^{-4} s^{-1} for f, which then yield an Ekman depth, α^{-1}, of 1.25 m. The model results are discussed next.

First, the barotropic pressure field in terms of the free surface displacement for the case of no density gradients is compared

with the free surface computed from inflow and the measured and extrapolated density fields. It may be evident in Figure 31a that with only inflow and friction, the east component of pressure gradient tends to be concentrated along the western shoreline, whereas with stratification, the gradient is not as sharply defined in Figure 31b.

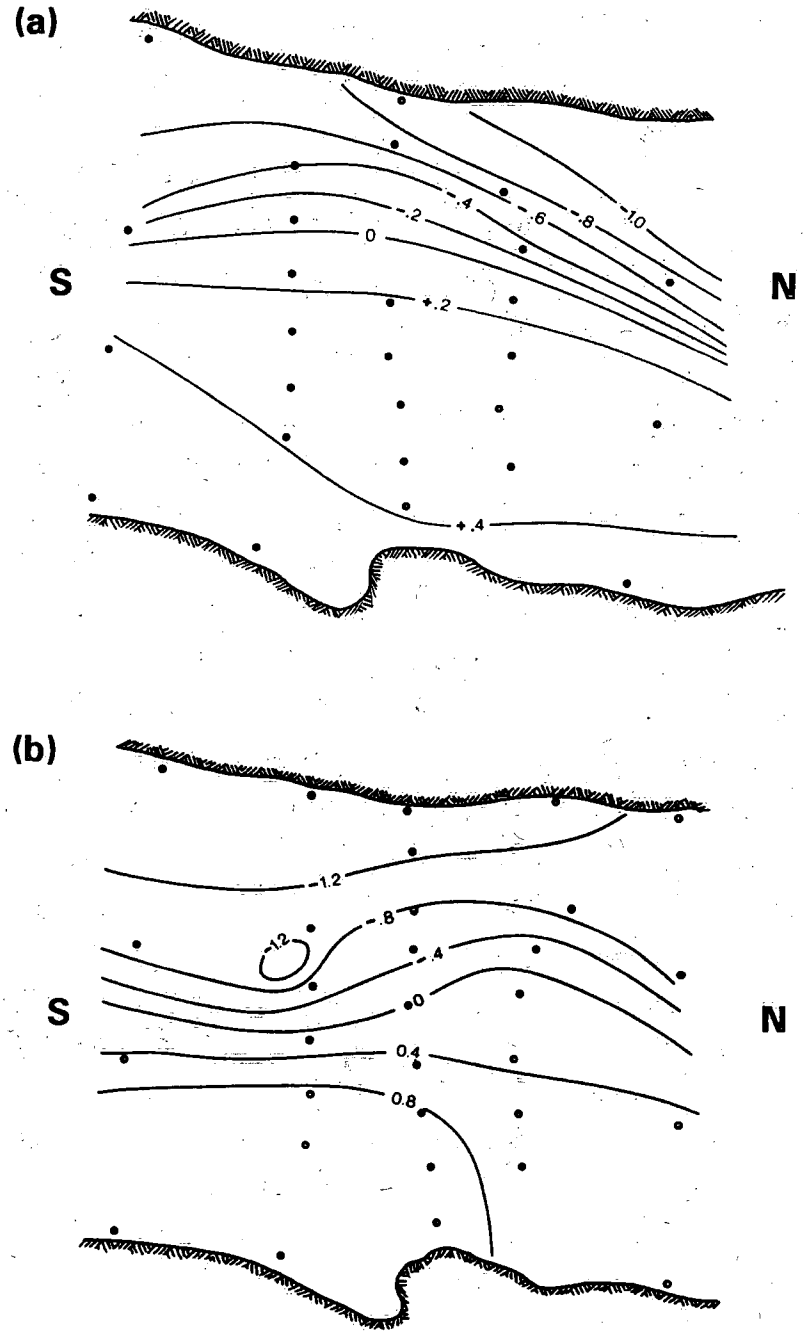

Figure 31. Surface water level displacement (barotropic pressure field) (cm x 10^2) based on diagnostic model, Tagish Lake. (a) No stratification. (b) With observed stratification, $\nu = 1$ cm^2/s.

In addition, the cross-lake component of pressure is nearly twice as large as in the horizontally uniform case. This finding is in agreement with the observations in Figures 18 to 20, which show that the northward transport is confined to the upper portion of the water column instead of being uniform throughout depth as is the case in a horizontally uniform density field. Thus the pressure gradients must be larger to allow for the compensatory effect of the horizontal density gradients.

The northward component of flow computed from equation (18) is shown in Figure 32 for the central and northern cross sections. When account is taken that the flow is computed at the station location instead of between the stations, as in the thermal wind method of Figures 18 to 20, the inverse method described here compares favourably with the direct method, especially at the central line. The northward jet of current centred between 2 to 3 m at station 5 is even more pronounced in the inverse method as is the weak return flow at depth. At the northern line (Fig. 32b), the northward jet is stronger and is compensated by a southward return on the eastern shoreline, unlike the direct distribution. The cross-sectionally averaged transports are 145 m^3/s at the central line, 122 m^3/s at the northern line, and 320 m^3/s at the southern line. The transport at the inflowing line is greatly in error due to the steep horizontal gradient of surface pressure at stations 10 and 16 seen on Figure 31b, which results in a northward flow of approximately 5 cm/s at these points. The lack of agreement of the transport at the inflow and outflow lines demonstrates the difficulty with the extrapolation of pressure gradients beyond the measurement area as these transports were found to be sensitive to the density gradients assumed. Twenty stations are probably too few to reasonably employ this diagnostic method unless the boundary transports are better known than in Tagish Lake. The alternative would be to specify the transports along lines 13–11 and 14–12, but this would probably introduce as much error as extrapolating the density gradients.

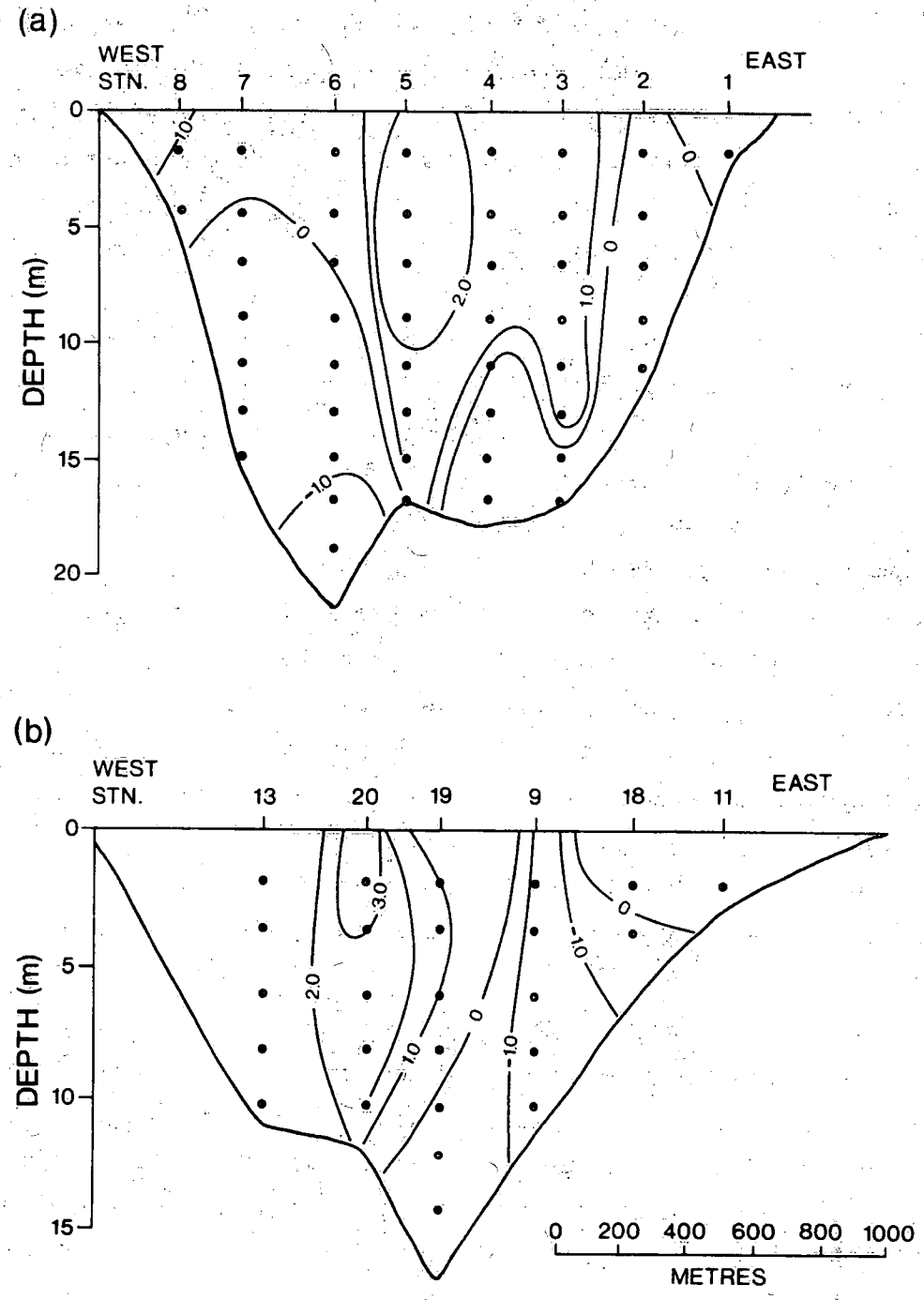

Figure 32. Northward component of flow (cm/s). Tagish Lake, (a) stations 1-8, (b) stations 13-11.

River Inflow Mixing

A key question in the design of northern impoundment is the length of the ice-free river downstream from the discharge point or,

alternatively, the heat flux out of the reservoir. The temperature data of Figure 8 and the similar sections of Appendix F of Carmack et al. (1987) show that the temperature of the outflow is determined by mixing at the inflow and that if heat is diffused to the through-flowing layer from the warmer bottom layer, it must be closely balanced by loss to the ice except in the vicinity of the outflow.

From an analysis of the heat budget in an ice-covered Norwegian lake, Sperillen, Stigebrandt (1978) deduced that the inflow is increased by 60% by river inflow mixing processes. In the present study, the return flow in Marsh Lake, as estimated from Figure 13, is 50% of the through-flow. Similarly, the return flow in Tagish Lake is calculated from Figures 18b and 19b to be approximately 30% of the through-flow. Unfortunately, there are no cross-sectional flow observations in Lake Laberge. Instead, Figure 8 and the longitudinal sections of Appendix F of Carmack et al. (1987) indicate that the isotherm dividing the through-flow from the main body of the lake is 0.8°C. Inflow at the freezing point mixing with lake water at an assumed temperature of 2.5°C (see Fig. 8) would have to be diluted by about 20% to form an average water temperature of 0.4°C. It is hoped that this crude calculation will be refined by the more precise thermodynamic model of Lake Laberge in the future.

In summary, the inflow-induced mixing appears to be somewhat weaker in the Yukon River headwater lakes than in the Norwegian lake. As Stigebrandt (1978) pointed out, weak inflow mixing is surprising in view of the relatively high densimetric Froude numbers of these lakes in winter. He also mentioned that no reliable estimates of inflow mixing are available in the literature. A search of the literature by the present author yielded the same conclusion. More recent studies dealing with this question are reviewed below.

Turning first to the buoyant jet literature, the numerical studies of Adams et al. (1975) show some features in common with the observations. Their solutions show a rapidly varied deepening of the

inflow to a maximum depth. For the inflow data (U_0 = 0.6 m/s, g^i = 5.4 x 10^{-4} m s^{-2}, and h_0 = 2 m [Carmack et al., 1987]) the jet theory yields a maximum depth of 80 m and a dilution rate of 13, both of which are unrealistically too large. The empirically based inflow dilution formula of Jirka and Watanabe (1980), which is similar to that of Adams et al. (1975), results in an inflow dilution of about 8 based on the Lake Laberge inflow data.

The buoyant jet theory neglects the effects matching the farfield density distribution of the jet to the downstream conditions. In an important study, Wilkinson and Wood (1971) showed, through both analysis and laboratory measurements, how the inflow dilution rate is linked to the downstream condition through the mechanism of drowning of a rapid flow transition known as a density jump or more loosely as an internal hydraulic jump by the downstream flow conditions. As the thickness of the outflow layer is increased and the jump is pushed closer to the inflow, the length of the supercritical flow region between the outflow and jump is reduced and accordingly the dilution rate of the inflow. The two-dimensional analysis of Wilkinson and Wood (1971) predicts a hydraulic jump from 2 m to about 45 m, a result closer to the observed maximum depth of about 10 m, but still too high.

The question of the mixing of the inflow with the open lake is explored in more detail by reference first to the recent two-dimensional theory of Baddour (1987). Baddour shows that under certain circumstances it is possible to predict the dilution of through-flow. Baddour describes a mixing zone between the inflow and interior flow, which has four types of behaviour depending on the characteristics of an internal hydraulic jump. If the inflow to Lake Laberge has a depth of 2 m, a uniform width of 200 m, and a discharge of 140 m^3/s (Carmack et al., 1987), and if the open lake conditions are taken as a depth of 100 m and discharge densimetric Froude numbers ranging from 11 to 14, depending on the density structure, are assumed, then the inflow would hydraulically jump from supercritical inflow to depths from 34 to 46 m where the flow would be subcritical based on Baddour's mixing zone equation (9). The theory allows for a dilution across the mixing zone; in this case a

dilution of 1.4 was assumed. In this parametric range, the stable subcritical depths or conjugate depths are not sensitive to dilution. At a Froude number of 11, conjugate depths ranged from 34 to 36 m over a dilution range of 10% to 90%. Since the depth of subcritical flows predicted by the two-dimensional theory are deeper than the observed and predicted depth of through-flow layer at the upstream end of the lake of about 10 m, then the mixing zone may be classified as a type C or upstream controlled instability. According to the laboratory experiments of Baddour (1987), this regime has a steep gradient of the interface in the mixing zone or point of virtual control (infinite at a critical depth of 16.4 m) as the interface proceeds from supercritical to the subcritical depth; there is also evidence of recirculation of the inflow. Both these features are apparent in the field data of Figure 8 and Appendix F of Carmack et al. (1987), where the isopleths of conductivity and temperature appear to bend down to the conjugate depth of about 25 m from the interior. The closed contours of conductivity are suggestive of recirculation. Since the interface of the through-flow does not intersect across the mixing zone, it is not possible, in this case, to predict the dilution factor; in this analysis it was assumed from field measurements. Based on the inflow Froude number, Baddour gives an upper limit for optimal mixing which, in this case, is a factor of three. Although the two-dimensional theory gives some indication of the inflow mixing, the results are limited by assumption of uniform width.

As an attempt to allow for spreading of the inflow, the radial internal hydraulic jump equation of Lee and Jirka (1981) was applied to the Lake Laberge inflow. In this case, the radius at which the jump begins was taken to be 60% of the total depth, as suggested by the experiments of Lee and Jirka. The depth was assumed to be 100 m.

According to their equation (34), the conjugate depth to 2 m is 16.4 m, which is still more than the observed through-flow layer thickness of 8 m in Lake Laberge. Thus, according to the three-dimensional theory, the inflow mixing regime is also unstable. However, since the conjugate depth is much closer to the through-flow depth, three-dimensional theory suggests that it would not require such a

large decrease in the inflow to achieve optimal mixing as in the two-dimensional case. In summary, the theory of Baddour (1987) and Lee and Jirka (1981) provides an alternate explanation for the relatively low inflow dilution observed. The inflow may not be treated simply as a buoyant jet discharging into an infinite reservoir, but instead it is necessary to consider the interaction of the inflow with the outflow at the downstream end of the lake. The theory suggests that inflow dilution rates may decrease for the increased inflow due to an inverted hydrograph. Additional laboratory evidence for decreasing dilution with an increased inflow Froude number is reported in the inflow experiments of Leong (1988).

The theory and laboratory results discussed above apply strictly to the case of two-layer stratification, whereas the field data clearly indicate a uniform rate density stratification in the inflow layers. In the absence of laboratory or theoretical guidance, it may be assumed that maximum depth is a point of virtual control where the internal wave velocity equals the inflow velocity. If a constant rate of deepening of the inflow plume applies, then the length of the supercritical portion of the plume should vary according to the rates of the maximum depths or to the one-third power of the discharges. This provides an upper bound on the dilution rate as the inflow depths also increase with increasing discharge according to the 0.6 power of the discharge. Experiments are required to confirm that the increase of dilution with increasing discharge are bounded by the one-third power of discharge in a uniformly stratified fluid.

Thermal Modelling

River Thermal Regime Modelling

Daily inflow temperatures are required as input to a model designed to simulate the thermal structure in lakes. For this purpose, a river water temperature gauge was established in the Yukon River near the entrance to Lake Laberge (Fig. 1). Due to instrument failure and periods of extremely low water, there were intervals of missing data. A river

temperature simulation model was developed to fill these gaps in the daily records.

Conservation of heat in a water body may be expressed in terms of the cross-sectionally averaged temperature, T, as

$$\rho\, C_p\, Y \frac{dT}{dt} = Q_A + Q_B$$

where C_p is the specific heat of water, Y the mean depth, t the time, and the source terms, Q_A the atmospheric heat flux and Q_B the heat flux from the bottom and sides of the river channel. Since the interest is on the entire river reach, advection and diffusion terms are neglected. Since an initial sensitivity test employing standard values of the thermal conductivity of bottom sediment and the assumption of 8°C bed temperature at a depth of 1 m below the bottom showed that the term Q_B is negligible, it will not be included in the model.

The atmospheric energy input, Q_A, is composed of solar radiation, Q_{SW}, which was directly measured at the meteorological station; Q_{LW} or incoming longwave radiation; Q_B, outgoing longwave radiation; Q_S, the sensible heat flux between the air and water surface; and Q_L, the evaporative heat flux. With the convention that incoming energy flux is positive, we have that

$$Q_A = Q_{SW} + Q_{LW} - Q_B + Q_S + Q_L.$$

Since the shortwave radiation was measured at a height from 4 to 6 m above the ground, it is necessary to account for the shading of low angle solar radiation on the surface of the river by the river banks and surrounding trees. According to TVA (1972), the daily solar radiation is reduced by the amount

$$\frac{hss \sin\phi \sin\delta + \cos\phi \cos\delta \sin hss}{hs\delta \sin\phi \sin\delta + \cos\phi \cos\delta \sin hs\delta}$$

where the solar declination angle, δ, is given in terms of the Julian Day, JD, by the formula

$$\delta = \frac{23.45\ \pi \cos\ [2\pi(172-JD)/365]}{180}$$

ϕ is the latitude, and cos hss = - sin ϕ sin δ/(cos ϕ cos δ). If the solar altitude at sunset or sunrise is α, here assumed to be 20°, then cos hss = (sin α - sin ϕ sin δ)/(cos ϕ cos δ) providing the quantity on the right-hand side is less or equal to unity. If it is larger than unity, then no solar radiation is received on that day at sunrise. The solar radiation transmitted to the water is reduced by a further 3% to account for the albedo of the water surface. Shading effects in river thermal models have also been discussed by Mason (1983).

The longwave radiation, Q_{LW}, was not measured but reconstructed from the measured air temperature, T_A, and estimated cloud cover according to the Swinbank formula (TVA, 1972):

$$Q_{LW} = 5.18 \times 10^{-13}\ (1 + 0.17\ C^2)\ (273 + T_A)\ W/m^2$$

The fraction of cloud cover, C, was determined from the measured solar radiation and the clear sky radiation, Q_{SC}, for the latitude of 60°N according to the Smithsonian Meteorological Tables, using $C^2 = (1 - Q_{SW}/Q_{SC})/0.65$. Daily estimates of Q_{SC} were interpolated from eight values evenly distributed over the year. Again, the above empirical formula is taken from the TVA (1972) report. The validity of this expression for Q_{LW} will be examined for high latitudes in the next section.

The outgoing longwave radiation, Q_B, is given by

$$Q_B = 5.23 \times 10^{-8}\ (273 + T)^4\ W/m^2$$

where T is the simulated water temperature.

The sensible and evaporative heat fluxes are specified according to the standard expressions except that the bulk transfer coefficient, C_s, was taken as 2×10^{-3} instead of the value recommended by Fischer et al. (1979) of 1.5×10^{-3}.

The daily river discharge, Q, is known, but not the river depth, Y. Based on the assumption of a rectangular channel, the river depth may be estimated from Mannings formula,

$$Q = K \; S^{1/2}$$

where the conveyance, K, is given by

$$K = Y^{5/3} \; w/n$$

Since the bedslope, S, channel width, w, and Mannings n are unknown, the factor F relating discharge to water depth, $Q = F \; Y^{5/3}$, was determined by optimization based on the most complete ice-free season of 1983. A best fit value of F of 5.65 $m^{4/3}/s$ resulted in an overall RMS error of 1.00°C between observations and model results. The model was initiated on April 12, 1983, with the observed river temperature of 0°C and run for 208 days until November 6, when the observed temperature reached the freezing point.

From the optimum value of F, the average value of the bedslope of 2×10^{-4}, and the river width of 250 m, the best fit value of Mannings n is 0.675 $s/m^{1/3}$. A comparison of this value to those more commonly quoted reveals that this estimate is 20 times larger than other rivers. This is probably because upstream water temperatures are unknown and there are a number of lakes in the watershed that alter the thermal regime. Additional evidence supporting the conclusion is that river depths varied between 6 and 15.5 m, which are probably too deep.

Although the model result is not physically realistic, it is nonetheless possible to use it to supply the missing river inflow temperatures.

The comparison of simulated and observed river temperatures for the Yukon River just upstream from Lake Laberge is shown in Figure 33. Since the starting temperature on June 10 was not known, it had to be estimated. By a series of iterations, the initial temperature that resulted in exact agreement on July 10, when river water temperatures became available, was determined. It may be noted that river temperature tends to be overestimated in the first part of the ice-free season and underestimated in the latter half of the season. This is probably due to the effect of the headwater lakes on the thermal regime of the river.

Evaluation of Empirical Relations for Incoming Longwave Radiation

For the purposes of modelling the thermal regime of Lake Laberge, it is necessary to establish the incoming longwave radiation field on a daily basis. In addition, since the usual empirical formulae require fraction of cloud cover, it is necessary to estimate the cloudiness from the measured shortwave radiation. It was considered that in a mountainous region the longwave radiation at Whitehorse, approximately 27 km from the meteorological station at Lake Laberge, would not be fully representative. As an example of spatial variability in daily meteorology in this area, the air temperatures from June 1 to December 31, 1982, are compared in Figure 34 for all stations available in the area of interest. It is evident that the Braeburn station located near the north end of Lake Laberge and Takhini Ranch near the south end register more severe cold temperatures than at Whitehorse. Variations in temperature within the immediate Whitehorse area are much smaller. Similarly, precipitation, which is required for the accumulated snow cover of Lake Laberge, is seen to vary between the two areas in Figure 35. However, major events such as the rainy period from October 16 to 23, 1982, and the December 2 snowfall are found at all four stations.

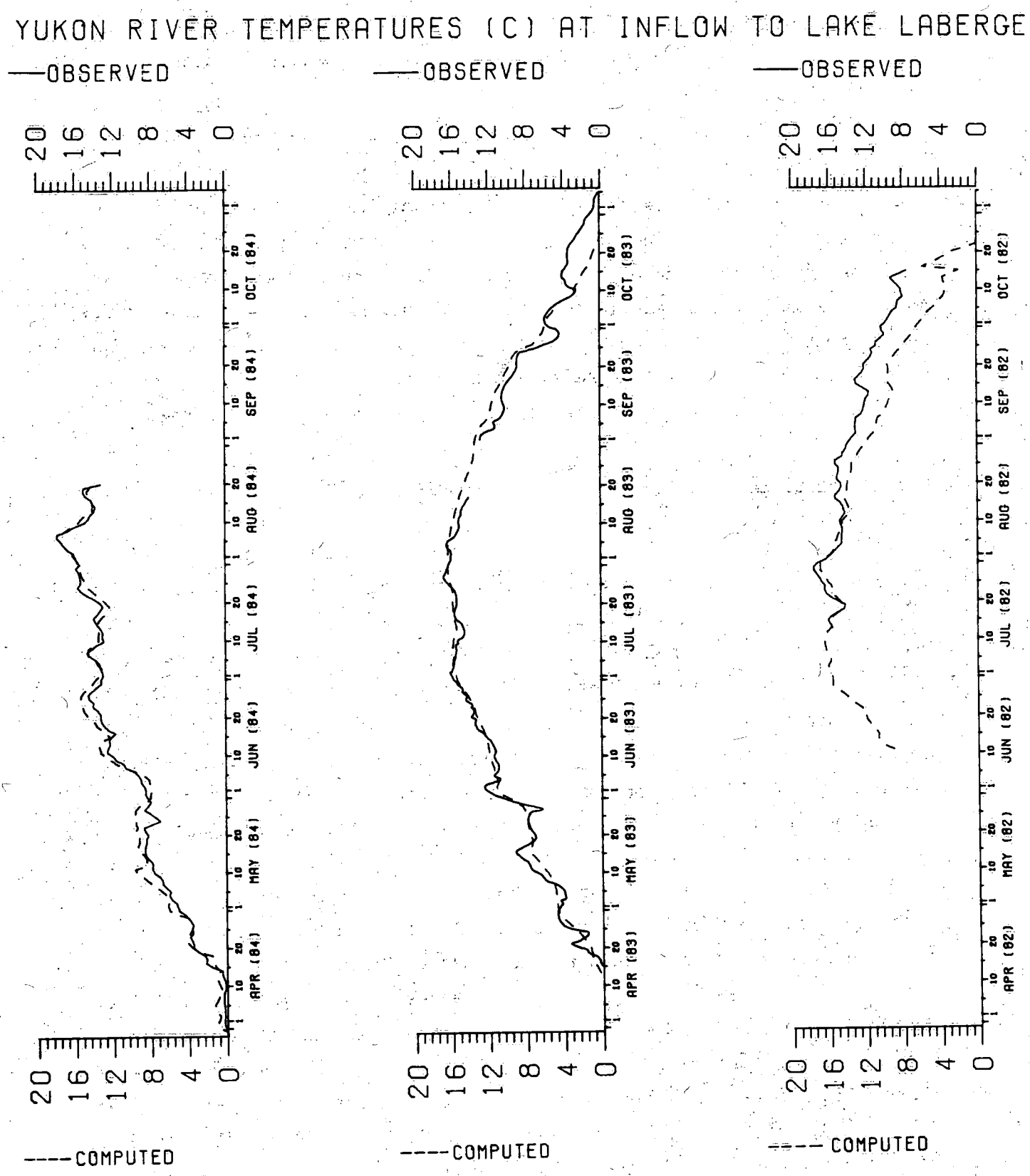

Figure 33. Observed and computed temperature of the Yukon River during the ice-free season, June 1982 to August 1984.

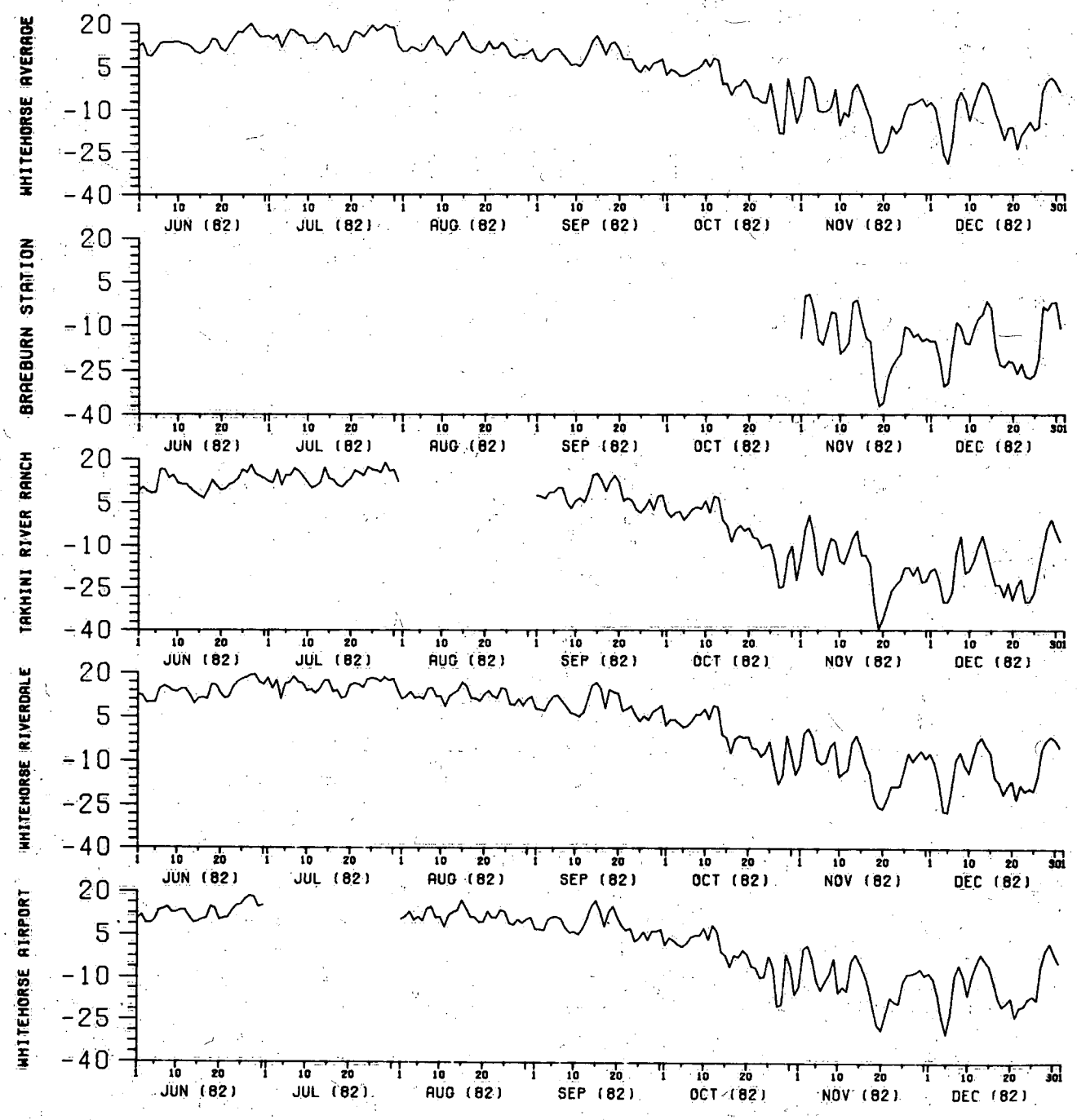

Figure 34. Daily averaged air temperatures, Whitehorse-Lake Laberge area.

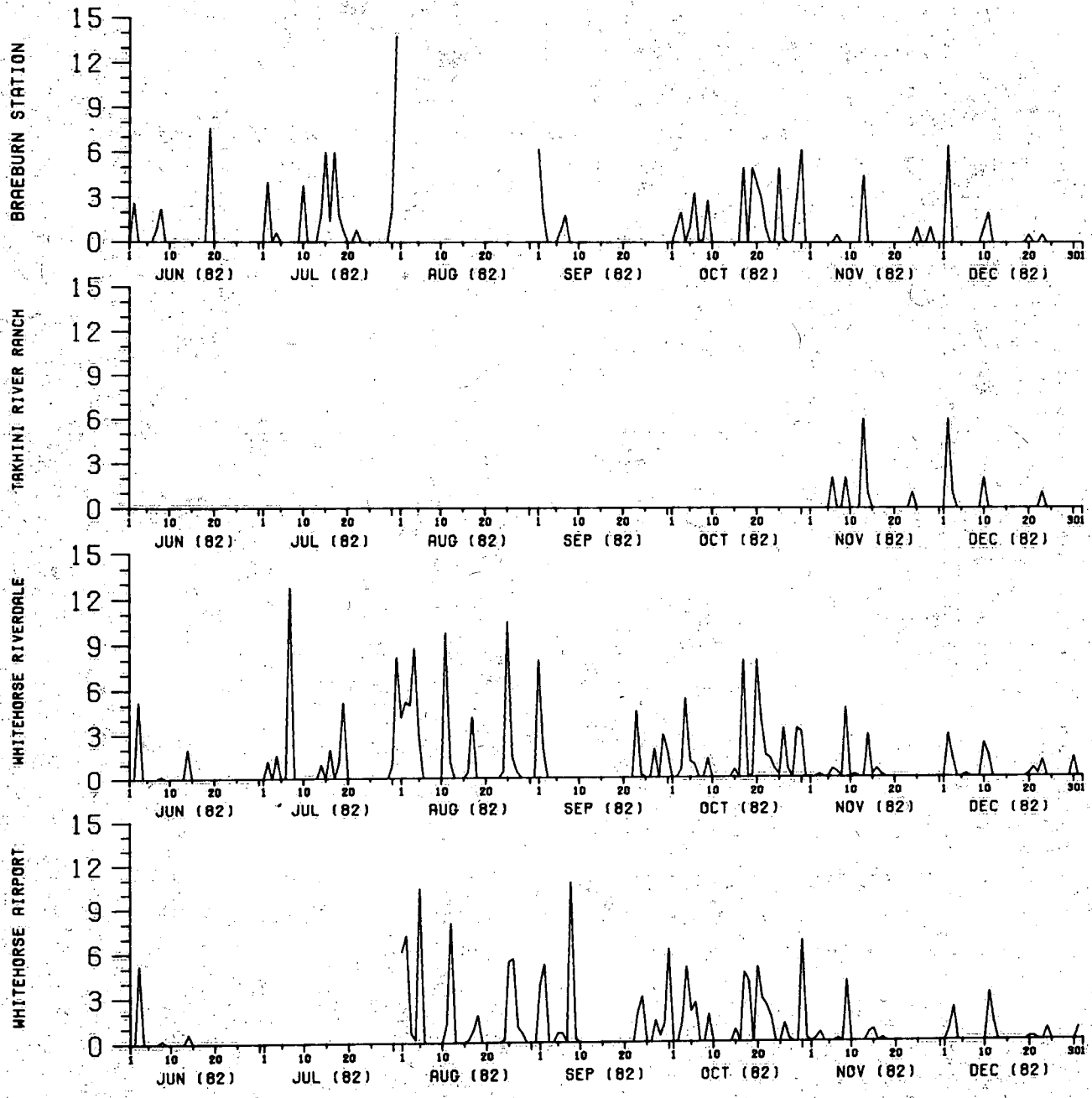

Figure 35. Precipitation (mm) June to December 1982, Whitehorse-Lake Laberge area. Note that rainfall data at Takhini River Ranch are missing from June to October.

Observed daily fractions of cloud cover squared, C^2, are compared to those computed from the standard empirical formula in TVA (1972),

$$C^2 = (1 - Q_{sw}/Q_{cs})/0.65$$

where Q_{cs} is the clear sky shortwave radiation given as a function of latitude, atmospheric attenuation, and date by the Smithsonian Meteorological Tables. Computed cloudiness squared for a range of atmospheric attenuations was compared to the Whitehorse observations. Best agreement was found for atmospheric attenuation of 0.83 at Whitehorse and is seen to be reasonably close in Figure 36a even during the winter period. On the other hand, a comparison of cloudiness measured at Whitehorse and computed at Lake Laberge shown in Figure 36b demonstrates similar agreement during the summer period, but poor agreement in the winter period. It is noted that the best agreement (R^2 = 0.7) was found for an attenuation coefficient of 0.85 and that the clear sky radiation value on December 22 was increased to 840 from 441 kJ/(m^2d) to better match the observed shortwave radiation.

The incoming longwave radiation at the Whitehorse airport meteorological station was not directly measured, but had to be estimated on an hourly basis from the measured net radiation, the shortwave radiation balance, and the outgoing longwave radiation, and then the hourly contributions summed to daily totals. The outgoing longwave radiation was based on measured air temperatures. The computed daily sequence of incoming longwave radiation is provided in Figure 37. Once the incoming longwave radiation has been determined, it is possible to evaluate methods for estimating this quantity. Two empirical formulae recommended in the TVA (1972) report, the Swinbank and Anderson relations, both require air temperature and cloudiness, while the Anderson is also based on vapour pressure. Figure 38 shows that the Swinbank formula tends to overestimate the incoming longwave radiation in the late spring and early summer, but not as much as the Anderson expression. Conversely, from October through to December, the Anderson

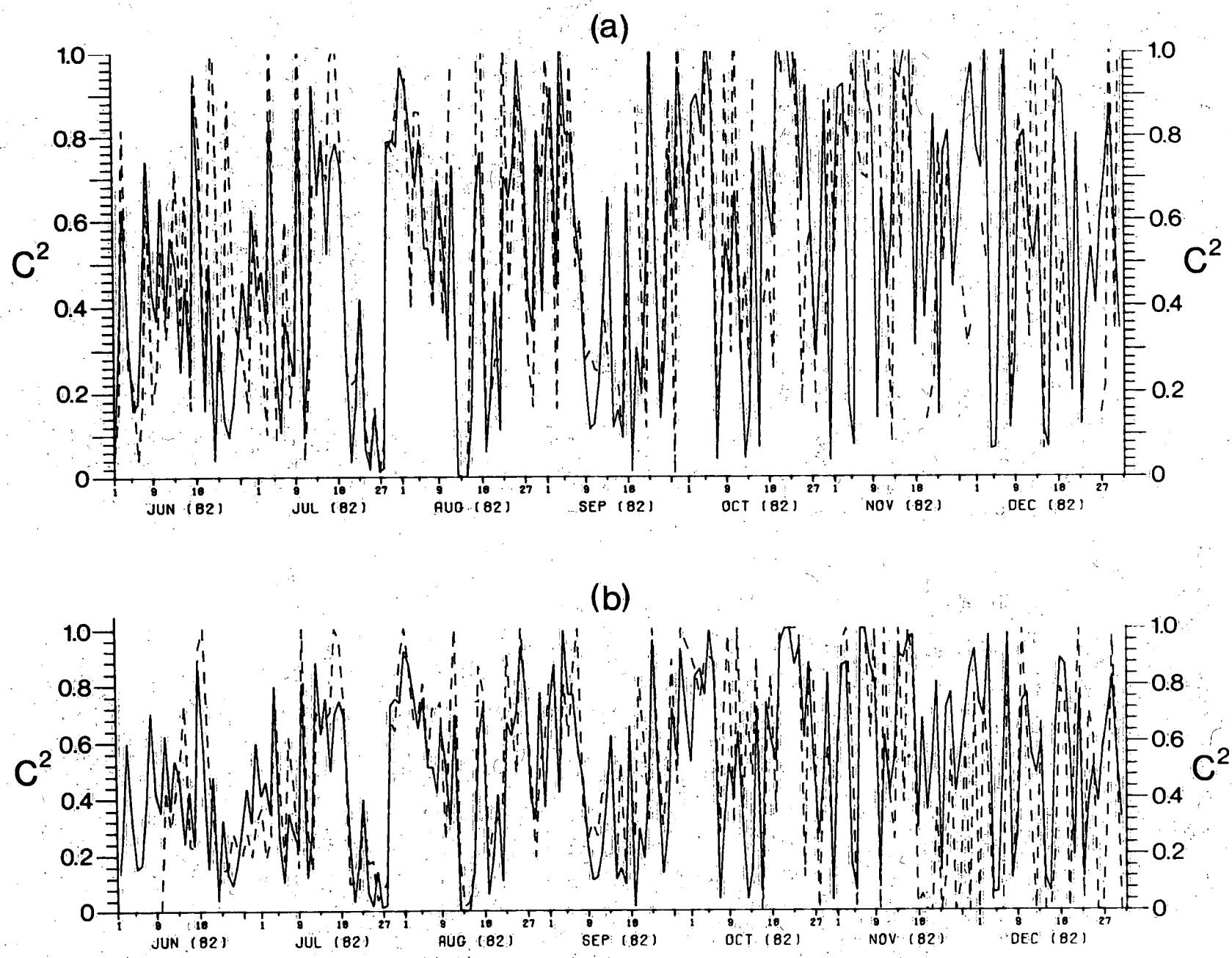

Figure 36. Comparison of the observed (solid line) and computed (dashed line) daily cloudiness fraction squared, June to December 1982. (a) Attenuation coefficient of 0.83, both at Whitehorse. (b) Attenuation coefficient of 0.85, observed at Whitehorse and computed at Lake Laberge.

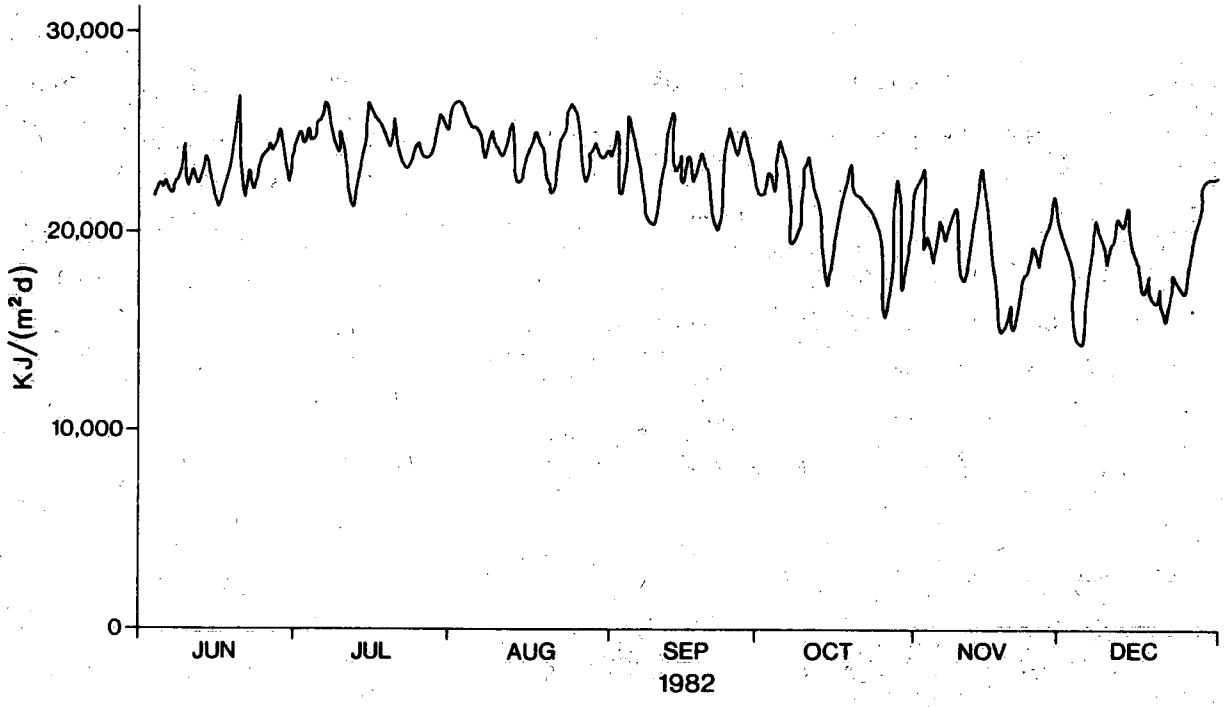

Figure 37. Computed daily incoming longwave radiation (kJ/(m^{2}d) from measured radiation at Whitehorse, June to December 1982.

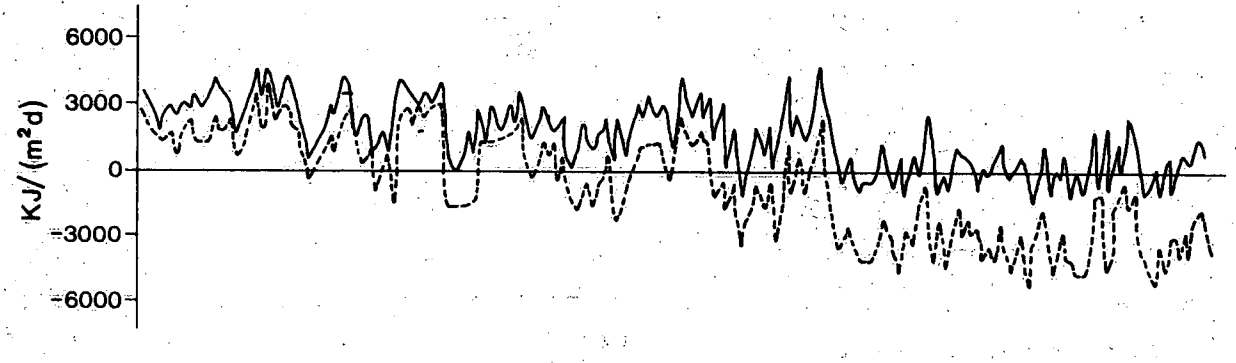

Figure 38. Estimated minus observed daily incoming longwave radiation at Whitehorse for the Anderson formula (solid line) and the Swinbank formula (dashed line). Note that cloudiness is directly measured.

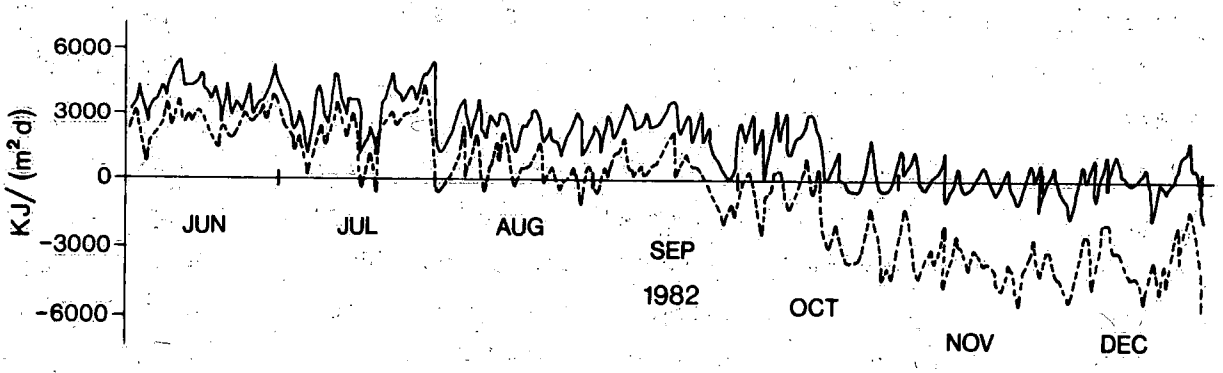

Figure 39. Same as Figure 38, but cloudiness is empirically estimated from observed and clear sky solar radiation.

relation is superior to the Swinbank. It is recommended, therefore, that the Swinbank formula be used when the daily averaged air temperature is above the freezing point and that the Anderson law be used for subfreezing temperatures. The identical conclusion is reached in Figure 39, where the two formulae are based on empirically computed cloudiness instead of directly observed cloudiness. It is possible that the better agreement during cold periods in the Anderson formulation is due to the inclusion of vapour pressure, which would account for the longwave contribution due to fog.

Two-Dimensional Lake Model

In order to better understand the outflow dynamics in an ice-covered stratified lake, a two-dimensional numerical model was constructed and solved for the steady circulation starting from a rest state and for a parameter range appropriate to Lake Laberge. The temperature of the cavity, boundary conditions, and the nonhydrostatic equations of motion in nondimensional form are presented in Figure 40. For details of the numerical method, see Marmoush (1985). The variable, θ, represents nondimensional temperature according to $\theta = (T - 4.0)/(T_b - T_s)$ where T_b is the bottom temperature and T_s is the surface temperature, ψ is a nondimensional stream function, $\psi = h/q\ \psi^1$, where q is the flow per unit cross-sectional width, Ω is the nondimensional vorticity, $\Omega = h^2/q\ \Omega'$, ρ is nondimensional time, $\tau = q/hl\ t'$, U and V are the nondimensional horizontal velocity components, respectively, $U = h/q\ U'$, $V = l/q\ V'$, x the horizontal coordinate has been nondimensionalized by the length of the cavity, l, and y the vertical coordinate has been scaled by h, the height of the cavity. In the preceding, primed quantities represent dimensional quantities. Four nondimensional parameters appearing in the equations of motion are the outflow Froude number (Fischer et al., 1979), $F_r = q\sqrt{\Delta\rho/\rho gh^3}$, the Grashof number, $g\Delta\rho h^3/(\rho K^2)$, where $\Delta\rho/\rho = 6.8 \times 10^{-6} (T_b - T_s)(8 - T_b - T_s)$, the Prandtl number, ν/κ, where ν is the viscosity and κ the conductivity, and the cavity aspect ratio, $A = h/l$. The function $f(\theta)$ in Figure 40 is simply θ^2, which approximates the density

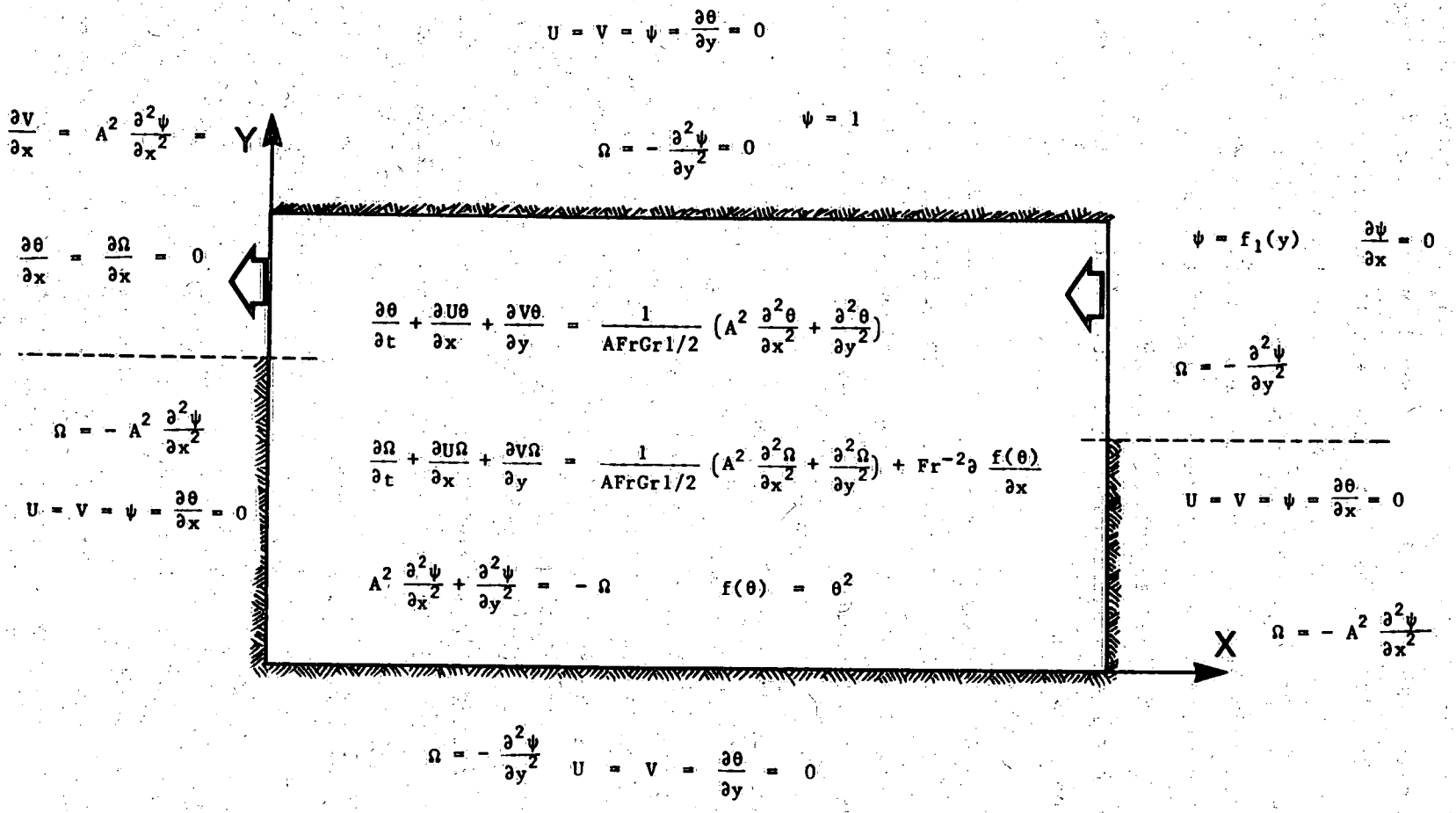

Figure 40. Schematic diagram of the rectangular cavity flow model. Equations of motion and boundary conditions are given and notation is in the text.

dependence on temperature at cold temperatures by a quadratic relation. The boundary conditions on the solid side walls and ice-covered surface are the standard insulated and nonslip boundary conditions. The inflow and outflow boundary conditions are specified according to the recommendations of Roache (1972). In the inflow boundary conditions, it was found necessary to specify the stream function distribution across the inflow for stability reasons. The function $f_1(y) = -16(y - 0.5)^3 + 12(y - 0.5)^2$ yields an assumed parabolic inflow profile. The inflowing temperature distribution is assumed to remain at the initial observed value. The domain is described by a mesh of 21 points in the vertical and 201 in the horizontal.

A series of cases were run to test the sensitivity of the flow and temperature fields to various combinations of nondimensional parameters. It was found that the inflow Froude number appeared to be the most sensitive parameter and that for large F_r of order unity, the inflow fills the cavity uniformly, whereas for small F_r of order 10^{-2} to 10^{-3}, the inflow crosses the cavity near the surface. The final test examined the case of nondimensional parameters based on the physical setting of Lake Laberge and assumed values of the eddy diffusivity and eddy viscosity of 1×10^{-5} m^2/s. For comparison with the model results of Figure 41, a longitudinal temperature section is presented in Figure 8 based on the field data collected in March 1983.

Near steady solutions after 1600 time steps or 105 days from the initial period for the stream function and temperature fields are shown in Figure 41 for Fr $= 7.3 \times 10^{-4}$, Pr $= 1$, A $= 3.2 \times 10^{-3}$, and Gr $= 3.0 \times 10^{3}$. Initially, the surface temperature is assumed to be 0.3°C, the bottom temperature, 2.3°C, and the intermediate temperature to vary uniformly between these limits. There is a similarity between the velocity and temperature distributions, particularly near the outflow in the low outflow Froude number regime. This supports the hypothesis adopted in the analysis of the Marsh Lake temperature data that the vertical velocity may be inferred from the slope of the isotherms and the horizontal velocity. Noteworthy is the indication of a weak return flow

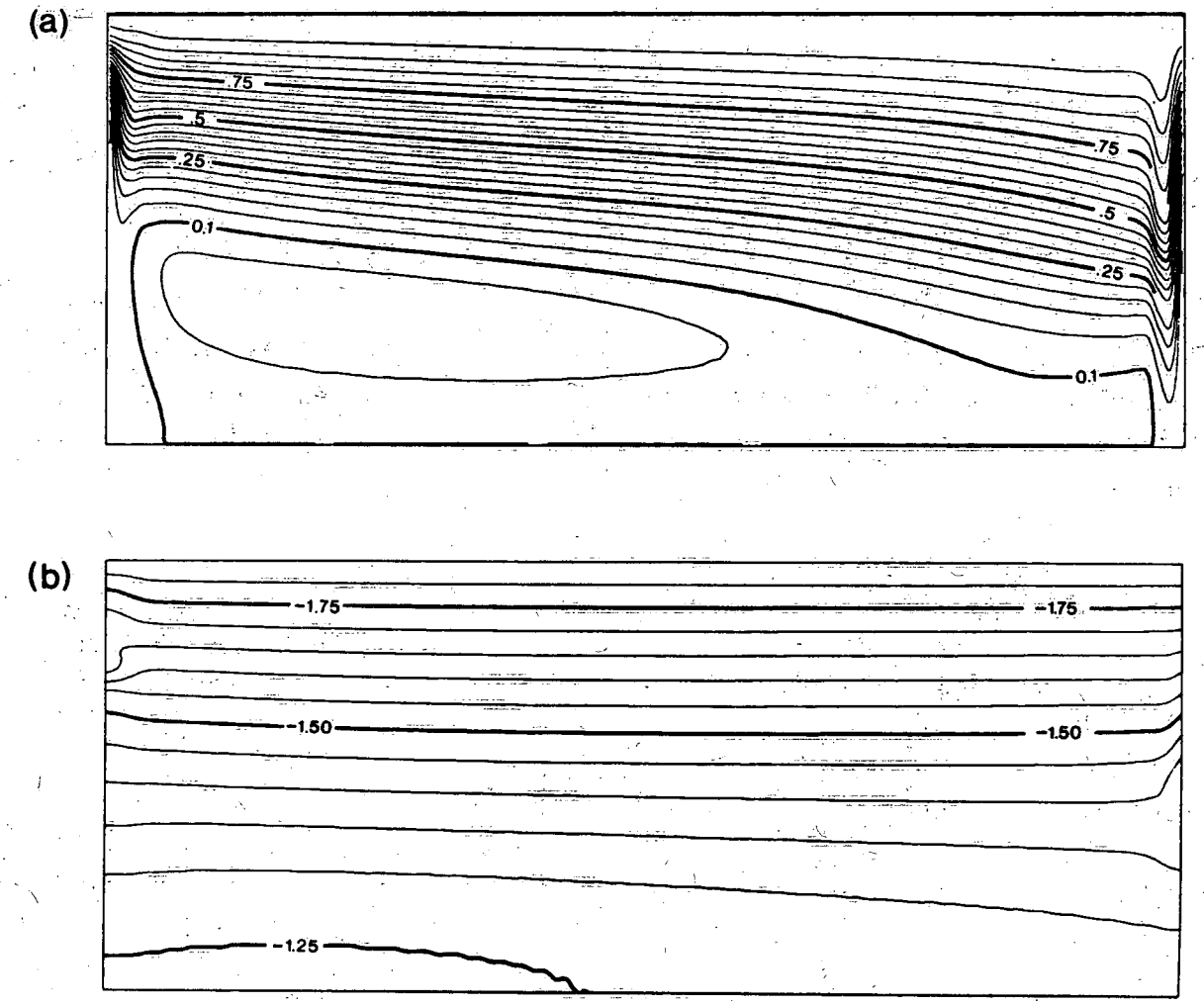

Figure 41. Solutions for A = 3.2 x 10^{-3}, Gr = 3 x 10^{13}, Fr = 7.3 x 10^{-4}, and t = 0.06. (a) Stream function. (b) Nondimensional temperature.

in the lower depths of the model lake, which supports the assumption made in the analytical model that the outflow circulation does not extend to the bottom except near the outflow. Another interesting feature of the solution is the rapid deepening of the inflow as it enters the cavity. This deepening is similar to the observed temperature distribution in Lake Laberge in Figure 8. This sudden transition could be an internal hydraulic jump as the inflow goes from critical to subcritical. Similarly, the isotherms below the outflow suggest the divergence seen in the field observations of Figure 8.

The nondimensional horizontal velocities at the grid point below the ice and the associated temperatures are listed in Table 2. The product of the numerically derived heat flux and the two distance laws obtained from the similarity and the analytical models demonstrates that the x^{-1} behaviour holds close to the outflow, while the $x^{-1/2}$ dependence is more appropriate further from the origin. It would appear that neither of the simple models is in good agreement with the numerical results and that more work must be done to parameterize the vertical heat flux under ice. The more rapid falloff of horizontal heat flux (UT_1) in the numerical model is also demonstrated in Figure 30 for the first three grid points.

Table 2. Comparison of Heat Flux near the Outflow of the Numerical Model with that Suggested by Analytical and Similarity Models

Grid point x	Nondimensional current U	T' °C	Proportional to heat flux UT'	$(UT - UT_\infty)x$	$(UT - UT_\infty)x^{1/2}$
1	-8.6	0.46	-3.78	-2.58	-2.58
2	-7.94	0.44	-3.41	-4.42	-3.12
3	-5.85	0.43	-2.49	-3.87	-2.23
4	-4.79	0.42	-2.01	-3.24	-1.62
5	-4.37	0.42	-1.83	-3.15	-1.40
6	-4.34	0.42	-1.82	-3.78	-1.54
7	-4.35	0.42	-1.82	-4.34	-1.64
8	-4.35	0.42	-1.82	-4.96	-1.75
9	-4.29	0.42	-1.80	-5.4	-1.86
20	3.0	0.40	-1.2	-	-

The similarity between the modelled and observed temperature distributions encouraged the repetition of the calculations for a more realistic variation of the depth of the cavity with uniform deepening from the end walls to the centre of the cavity. This computational domain was represented by 53 points in the horizontal and 41 points in the vertical at its deepest part. The boundary conditions for the sloping bottom were specified after Roache (1972).

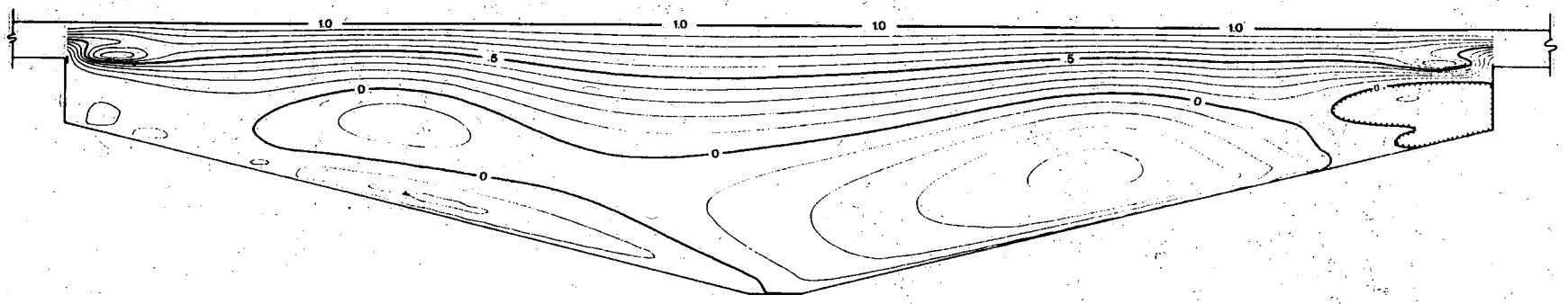

Figure 42. Stream function in variable depth model for the same parameter settings as in Figure 40, but t = 0.001 (Ra = 10^6).

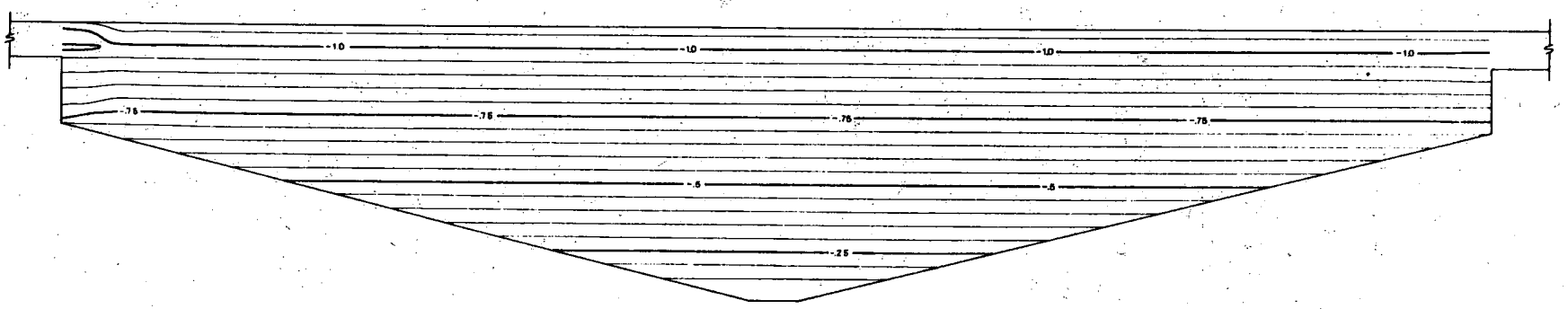

Figure 43. Nondimensional temperature associated with solution shown in Figure 42.

More limited sensitivity tests confirmed similar behaviour in the sloping cavity that higher Froude number inflows tend to fill the box. In one case of Fr 0.031, a weak return flow developed near the bottom mainly on the inflow half of the cavity after a sufficiently long period of time (about one day real time). The flow field after a period of 1.6 d or 500 time steps is seen in Figure 42 to be confined to the upper portion of the water column and to exhibit sharp transitional features close to the inflow and outflow. The main effect of sloping bathymetry appears to be splitting of the return flow at depth into several weak eddies. Unfortunately, in the fairly short period for the development of the solution, the associated temperature field has not departed significantly from its initial value. Only at the inflow and outflows does Figure 43 demonstrate a correspondence of the isotherms to the streamlines. As a further step towards a more realistic model of the water flow-through of Lake Laberge, the nonhydrostatic model was extended to include vertical and horizontal variations in cross-sectional width. At the time of writing, there have not been any successful solutions of this problem.

REFERENCES

Adams, E.E., K.D. Stolzenbach, and D.F. Harleman. 1975. Near and far field analysis of buoyant surface discharges into large bodies of water. Report 205, Department of Civil Engineering, Massachusetts Institute of Technology, Boston.

Baddour, R.E. 1987. Hydraulics of shallow and stratified mixing channel. J. Hydraul. Div., Am. Soc. Civ. Eng., 113: 630-645.

Ball, A.J. 1983. Temperature-turbidity relationships of southern Lake Laberge. National Water Research Institute, West Vancouver, B.C. Unpub. rep.

Baird, S. 1981. A solution to the problem of current vector measurements in areas of low horizontal magnetic field intensity. Fisheries and Oceans Canada, Burlington, Ontario. Unpub. rep.

Bogorodskiy, V.V., and K.K. Sukhorukov. 1983. Physical conditions of bottom melting of Arctic sea ice pack. Izvestiyza, Atmospheric and Ocean Physics, 19: 667-669.

Carmack, E.C., R.C. Wiegand, E. Marles, M.E. Alford, and V.A. Chamberlain. 1987. Physical limnology of an ice-covered lake with through-flow: Lake Laberge, Yukon Territory. NHRI Pap. No. 35/IWD Sci. Ser. No. 157, Inland Waters Directorate, National Hydrology Research Institute, National Hydrology Research Centre, Environment Canada, Saskatoon, Sask.

Csanady, G.O. 1985. Pycnobathic currents over the upper continental slope. J. Phys. Oceanogr., 5: 306-315.

Den Hartog, G., S.D. Smith, R.J. Anderson, D.R. Topham, and R.G. Perkin. 1983. An investigation of a polynya in the Canadian archipelago, 3, Surface heat flux. J. Geophys. Res., 88: 2911-2916.

Dillon, T.M. 1982. Vertical overturns: A comparison of Thorpe and Ozmidov length scales. J. Geophys. Res., 87: 9601-9613.

Fischer, H.B., E.J. List, R.C.Y. Koh, J. Imberger, and N.H. Brooks. 1979. Mixing in inland and coastal waters. New York: Academic Press.

Gilpin, R.R., T. Hirata, and K.C. Cheng. 1980. Wave formation and heat transfer at an ice-water interface in the presence of a turbulent flow. J. Fluid Mech., 99: 619-640.

Hamblin, P.F. 1976. Seiches, circulation and storm surges of an ice-free Lake Winnipeg. J. Fish. Res. Board. Can., 33: 2377-2391.

Hamblin, P.F., and E.C. Carmack. 1990. On the rate of heat transfer between a lake and an ice sheet. Cold Reg. Sci. Tech., 18: 173-182.

Henderson, F.M. 1966. Open channel flow. New York: Macmillan Co.

Jirka, G.H., and M. Watanabe. 1980. Thermal structure of cooling ponds. J. Hydraul. Div., Am. Soc. Civ. Eng., 106: 701-715.

Josberger, E.G., and D. Meldrum. 1985. Bottom ablation measurements and heat transfer coefficients from MIZEX-WEST, February 1983. MIZEX Bulletin VI MIZEX West, P. Wadhams, ed. U.S. Army CRREL Special Report #85-6, 68-72.

Kirkland, R.A., and C.B.J. Gray. 1986. Reconnaissance of the chemical and biological limnology in four large lakes of the Yukon River basin. NHRI Pap. No. 33/IWD Sci. Ser. No. 153, Inland Waters Directorate, National Hydrology Research Institute, National Hydrology Research Centre, Environment Canada, Saskatoon, Sask.

Koh, R.C.Y. 1966. Viscous stratified flow towards a sink. J. Fluid Mech., 24: 555-575.

Langleben, M.P. 1982. Water drag coefficient of first-year sea ice. J. Geophys. Res., 87(C1): 573-578.

Lawrence, G.A. 1980. Selective withdrawal through a point sink. In Proc. 2nd Int. Symp. on Stratified Flows, pp. 411-425. Trondheim: Tapir Press.

LeBlond, P.H., and L.A. Mysak. 1978. Waves in the ocean. Amsterdam: Elsevier.

Lee, J.H.W., and G.H. Jirka. 1981. Vertical round buoyant jet in shallow water. J. Hydraul. Div., Am. Soc. Civ. Eng., 107: 1651-1675.

Leong, D.C.K. 1988. Mixing of dense river inflows into lakes. M.Eng. thesis, Department of Civil Engineering, University of Canterbury, Christchurch, New Zealand.

Liljequist, G. 1941. Winter temperatures and ice conditions of Lake Vetter with special regard to the winter of 1939/40. Swedish Meteorological and Hydrographical Institute Communication Series No. 35, 29 pp.

Marmoush, Y.M.R. 1985. Behaviour of thermal density currents in cold receiving natural water bodies. Ph.D. thesis, McMaster University, Hamilton, Ontario, 221 pp.

Mason, J.E. 1983. The effect of topographic shading on the energy budget of small lakes. M.Eng. thesis, Department of Civil Engineering, University of Canterbury, Christchurch, New Zealand.

Mellin, R. 1947. Investigations at the Meteorological and Hydrological Institute of Sweden concerning the ice conditions on lakes and rivers. Swedish Meteorological and Hydrological Institute Communications Series D, No. 1, 50 pp.

Mellin, R. 1948. Currents caused by water flowing through lakes. Extract of Proceedings of IUGG General Assembly. Oslo, Norway.

Monismith, S.G., and T. Maxworthy. 1988. Selective withdrawal and spin-up of a rotating stratified fluid. Unpubl. ms.

Papadakis, J.E. 1981. A simple method for monotonic approximation of functions. Pacific Marine Science Report 81-7, Institute of Ocean Sciences.

Patterson, J.C., and P.F. Hamblin. 1988. Thermal simulation of lakes with winter ice cover. Limnol. Oceanogr. 33(3): 328-338.

Pease, C.H. 1985. Theory of wind-driven coastal polynyas. Mizex-Bulletin VI, CCREL Special Report 82-6. U.S. Army Corps Eng. Cold Reg. Res. Eng. Lab., Hanover, N.H., pp. 112-119.

Rattray, M. 1982. A simple exact treatment of the baroclinicity-bathymetry in a frictional iterative diagnostic ocean model. J. Phys. Oceanogr., 12: 997-1003.

Roache, P.J. 1972. Computational fluid dynamics. Albuquerque: Hermosa Publishers.

Stigebrandt, A. 1978. Dynamics of an ice-covered lake with through-flow. Nord. Hydrol., 9: 219-244.

Topham, D.R., R.G. Perkin, S.D. Smith, R.J. Anderson, and G. Den Hartog. 1983. An investigation of a polynya in the Canadian archipelago, 1, Introduction and oceanography. J. Geophys. Res., 88: 2888-2899.

TVA. 1972. Heat and mass transfer between a water surface and the atmosphere. TVA Rep. No. 6803.

Wilkinson, D.L., and I.R. Wood. 1971. A rapidly varied flow phenomenon in two-layer flow. J. Fluid Mech., 47: 241-256.

Appendix A

Under-ice Drogue

APPENDIX A

UNDER-ICE DROGUE

by P. Hamblin and F. Roy

DESCRIPTION AND FIELD DEPLOYMENT

Figure A-1 presents a schematic diagram of the under-ice drogue. The positions of the drogue are determined by successive tracking of a radio beacon transmitting through the upper 10 cm of the water column and the ice and snow layers. Each transmitter has its own frequency so that more than one drogue may be deployed and tracked at a time. Figure A-2 demonstrates the near field tracking method by the location of the signal amplitude peak along straight lines. The far field antenna is used in a directional mode to locate the approximate position of the drogue. Details on the field operation of the underwater drogue are given by Roy and Savile (1985).

LABORATORY DROGUE EVALUATION

A series of tests were undertaken following the field experiment to examine the behaviour of roller blind drogues in a horizontal shear flow. Horizontal shears were observed in the field as large as 10^{-4} s^{-1}, which would result in a velocity differential across the drogue of 0.3 mm/s. While this differential is much less than the average speed in the field of about 1 cm/s, it is the same order as the slip velocity estimated to be 1 mm/s.

The effect of a linear shear is to displace the line of action of the net force on the drogue from the centreline to the direction of higher flow. Thus, the retarding force of the under-ice float and the displaced slippage force exert a torque on the drogue, which tends to rotate the drogue out of the shear. If the lateral slip is larger than the slip velocity, appreciable deviation of the drogue path may be experienced in the direction from high flow to low flow.

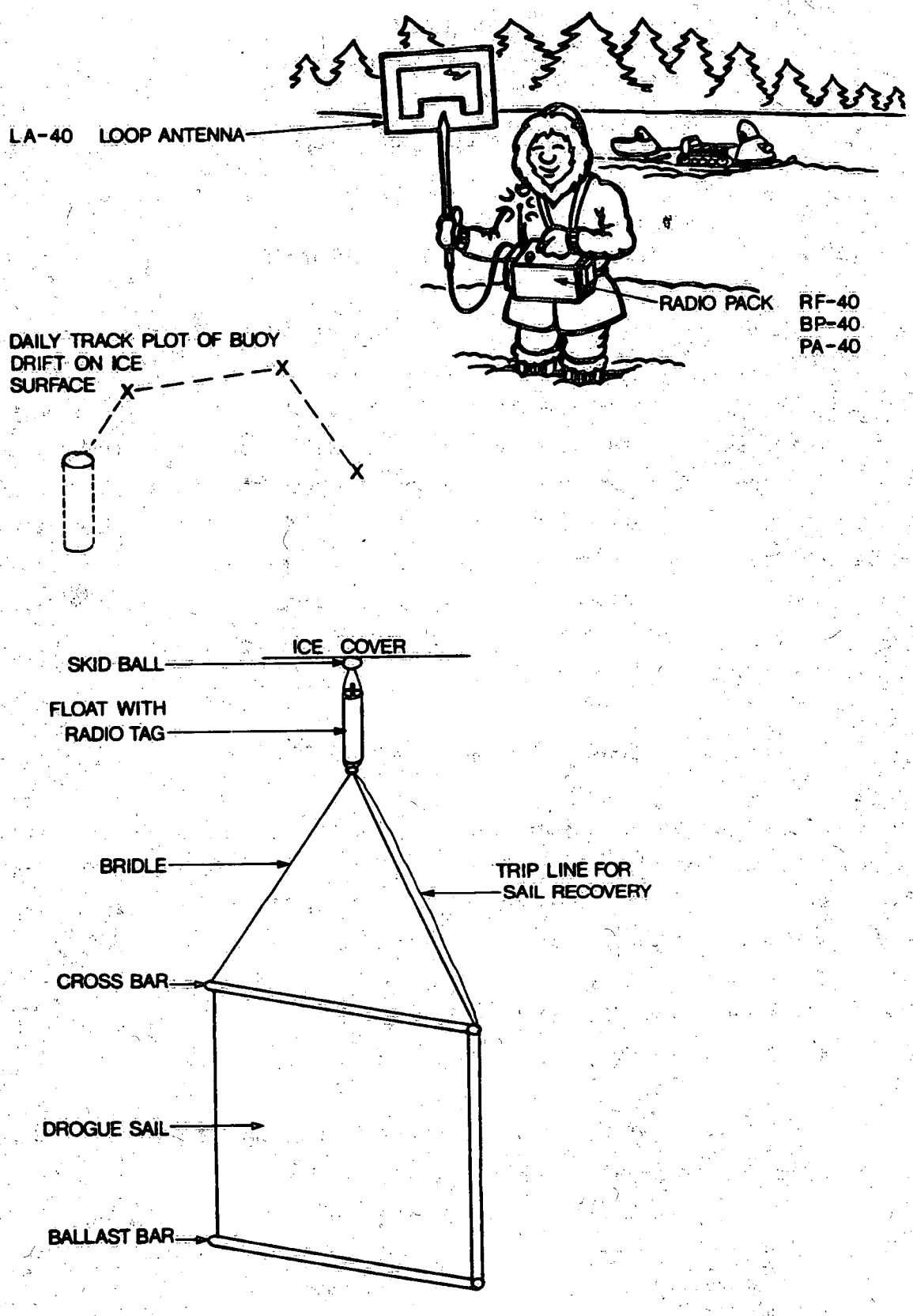

Figure A-1. Schematic of under-ice drogue and deployment concept.

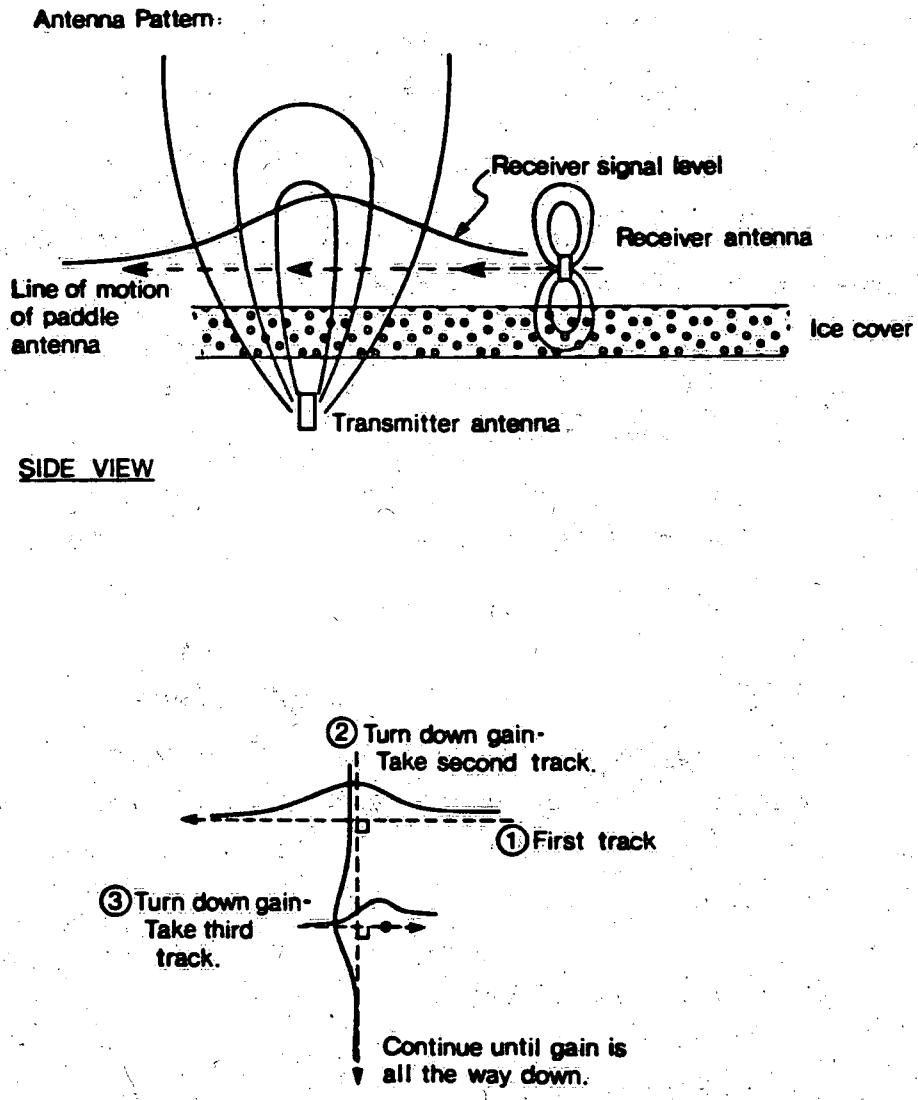

Figure A-2. Radio location technique.

Quantitatively, the offset from the centreline may be computed from integration of the aerodynamic drag law across the drogue

$$\tau = \frac{1.7}{2} \rho A U^2_s \qquad \text{(A-1)}$$

where 1.7 is the drag coefficient for a roller blind drogue (Vachon, 1973), A is the area, and U_s is the slip velocity.

$$\text{Z offset} = \frac{\int_{-L}^{L} (U_s + z\,U^1)^2 z\,dz}{\int_{-L}^{L} (U_s + z\,U^1)^2 dz}$$

where U^1 is the current shear and L is the half-width of the drogue, here 1.5 m. After some algebra, it may be seen that

$$\text{Z offset} = \frac{2L^2\ U^1\ U_s}{3\ U_s^2 + (U^1\ L)^2}$$

or

$$\text{Z offset} = 15 \text{ cm for } U^1 = 10^{-4}\ s^{-1} \text{ and}$$

$$U_s = 1 \times 10^{-3} \text{ m/s}$$

Therefore, in a shear flow of $10^{-4}\ s^{-1}$, the centre of action of the net slippage force is displaced by 10% of the drogue half-width from the centre of suspension. In order to test this result, a series of experiments were conducted in the CCIW laboratory towing facility with a 1-m^2 roller blind drogue.

Experiment 1 (No shear, uniform flow simulation)

During the first experiment, the test drogue was towed with the centre of attachment aligned as closely as possible to the centreline of the sail area in order to test the drogue behaviour in a uniform flow field. Reynolds number similarly occurred between the 1-m^2 test drogue and the 10-m^2 prototype at slippage or towing speeds between 0.5 and 1.5 cm/s. In addition, to simulate the under-ice friction on the surface float, the float was towed by a long string held nearly parallel to the water surface in the direction of travel of the towing carriage. At the three towing speeds of 0.5, 1.0, and 2.0 cm/s, the drogue was observed to rotate about its vertical axis at the same time as progressing laterally in the direction of the leading edge of the sail until apparently the restoring force of the string was sufficient to cause displacement and rotation in the opposite direction. These oscillations across the tank

were centred about the point of attachment to the carriage and were more vigorous at higher speeds with amplitudes estimated to be around 1 m at 2 cm/s. A further test at a speed of 0.5 cm/s was repeated with the towline free to move back and forth across the tank in order to maintain it parallel to the direction of flow thereby eliminating the restoring force. The drogue continued to oscillate as before, indicating that restoring forces are generated by the sail angle to the flow and not by the towline direction. Finally, the force on the drogue towing line was measured to be 5 g at 0.5 cm/s. This force is consistent with the drag law, equation (A-1).

Experiment 2 (Horizontal shear flow simulation)

In the second experiment, the point of attachment was offset from the centreline by 9.8 cm or by 20% of the half-length of the drogue. This arrangement attempted to simulate the effect of the shear, which, of course, could not be set up in the tow tank. Time limitations permitted only one speed, 0.5 cm/s, and one offset to be observed. In this case, the drogue was observed to "skate" in the direction of suspension offset and slowly twist so that the edge of the sail in the direction of offset became the leading edge. The drogue came into an unsteady equilibrium at a mean angle of 30° in the offset direction. Oscillations in the towline angle of $\pm 6°$ within a period of about five minutes were observed. Unlike the former case, when the towline was adjusted to move laterally in order to maintain zero lateral restoring force, the drogue continued to move to the side until eventually it collided with the side of the tank. The speed of travel of the sideways motion was estimated crudely to be about 1 cm/s or twice the slip velocity. As an approximate check on this performance ratio or ratio of lateral speed to forward slip velocity, we have at the 30° equilibrium angle that the restoring force would be 2.5 g. If the initial angle of rotation of the drogue is 10°, then at that position the 2.5-g force must be balanced by $\rho U^2 A/2 \sin 10°$, which gives a value of U of 0.85 cm/s or about twice the slip velocity. Further tests would be valuable, especially to establish the dependence of the performance ratio on percentage displacement of the suspension

point. Failing these data, we will simply assume in further analysis that either this relation is linear, that is, a performance ratio of zero at no offset and 2 at 20% offset, or at the other extreme that the performance ratio is independent of displacement except at zero displacement.

APPLICATION

With reference to Figure 18, the average velocities at the drogue depth, shear, and angular deviations expected are listed in Table A-1 for the Tagish Lake drogue experiment. On the basis of the assumptions made concerning the performance ratio dependencies on offset and the observations made during the towing test, it would appear that the tendency for drogues to sail across a shear zone towards a lower flow is probably tolerably small, say in the order of 10°, under field conditions and that the wandering behaviour of the drogues observed in Tagish Lake is due to the unsteady nature of the flow.

Table A-1. Average Speed and Shear at 6-m Depth, Line 1-8, Tagish Lake

Station	Average speed (cm/s)	Deviation constant performance ratio	Shear x 10^5 s^{-1}	Percent displacement	Angular deviation
6	1.0	-11°	-8.0	8	-5°
4	1.2	9°	3.0	3	1°
3	0.6	18°	1.4	1	1°
2	0.25	39°	1.6	2	2°

REFERENCES

Roy, F.E., and H.A. Savile. 1985. Handbook notes for under-ice drifter buoy. NWRI ES-1134. Unpub. rep.

Vachon, W.A. 1973. Scale model testing of drogues for free drifting buoys. Technical Report R-709. The Charles Start Draper Laboratory, Inc., Cambridge, Mass. 143 pp.

Appendix B

Under-ice Flow Equations

APPENDIX B

UNDER-ICE FLOW EQUATIONS

The steady Ekman equations may be written for $w = u + iv$ and $s = x + iy$; $(i = \sqrt{-1})$

$$ifw = \frac{-1\partial P}{\rho \partial s} + \frac{v\partial^2 w}{\partial z^2}$$

where $$\frac{\partial P}{\partial s} = \rho g \left(\frac{\partial \eta}{\partial x} + \frac{i\partial \eta}{\partial y}\right)$$

Under ice the boundary conditions are $w = 0$ at $z = 0$ and $z = -H$.

If $\alpha^2 = f/(2v)$ then the solution is

$$w = \frac{\partial P}{\rho if \partial s}\left(\frac{\{\cosh [(1 + i)\ \alpha H] -1\}}{\sinh ((1 + i)\ \alpha H)} \sinh [(1 + i)\ \alpha z] + \cosh [(1 + i)\ \alpha z] -1\right)$$

This solution may be integrated vertically for the transport, W.

$$W = \frac{\partial P}{if \partial s}\left(\frac{\{\cosh [(1 + i)\ \alpha H] -1\}}{\sinh [(1 + i)\ \alpha H]} \{1 - \cosh [(1 + i)\ \alpha H]\} + \frac{\sinh [(1 + i)\ \alpha H]}{(1 + i)\ \alpha} - H\right)$$

$$= \frac{2H\partial P}{if \partial s}\left\{\frac{\cosh [(1 + i)\ \alpha H] -1}{(1 + i)\ \alpha H \sinh [(1 + i)\ \alpha H]} - \frac{1}{2}\right\}$$

Finally, it is useful to obtain surface stress, $\tau_s = v\partial w/\partial z$ at $z = 0$ and at the bottom, $z = -H$, in the limiting case when $\alpha H \to \infty$. From the above expression for W, it can be shown that

$$\tau_s = \frac{1 + i}{i\ 2\alpha} \frac{\partial P}{\partial s} \frac{1}{\rho}$$

in complex notation so that

$$\tau_{sx} = \frac{\rho g}{2\alpha}\left(\frac{\partial \eta}{\partial x} + \frac{\partial \eta}{\partial y}\right)$$

and

$$\tau_{sy} = \frac{\rho g}{2\alpha}\left(-\frac{\partial \eta}{\partial x} + \frac{\partial \eta}{\partial y}\right)$$

Similarly,

$$\tau_b = -\frac{(1+i)}{i2\alpha}\frac{\partial P}{\partial s}\frac{1}{\rho}$$

so that

$$\tau_{bx} = -\frac{g\rho}{2\alpha}\left(\frac{\partial \eta}{\partial x} + \frac{\partial \eta}{\partial y}\right)$$

$$\tau_{by} = \frac{g\rho}{2\alpha}\left(\frac{\partial \eta}{\partial x} - \frac{\partial \eta}{\partial y}\right)$$

It may be noted that in the case of stratification the pressure gradient at the bottom may have an additional term,

$$\frac{g}{\rho_o}\int_{-H}^{0}\frac{\partial \rho}{\partial x}\,dz$$

Note: Lake Laberge meteorological and inflow water temperatures are available in edited format on tapes WA 1089 and DM 527 (nine-track, 1600 bpi records of 80 characters) at 10-, 20-, 30-, and 60-minute intervals (F = S, LB = KU).